Solar neutrinos at DUNE

Aran N. Borkum

University of Sussex

Department of Physics and Astronomy

Submitted for the degree of Doctor of Philosophy

University of Sussex

September 2022

UNIVERSITY OF SUSSEX

Aran N. Borkum

Solar Neutrinos at DUNE

Abstract

The Deep Underground Neutrino Experiment, DUNE, is a future long-baseline neutrino experiment, starting from the Fermi National Accelerator Laboratory, FNAL, to the Sanford Underground Research Facility, SURF. The far detector complex at SURF will consist of four 17-ktonne liquid-argon time projection chambers, LArT-PCs. DUNE's long-baseline physics program aims to evaluate neutrino oscillation parameters, the CP-violating phase, δ_{CP}, and determine the neutrino mass hierarchy. DUNE's low-energy physics program aims to observe solar neutrinos and those emanating from core-collapse supernovae. The low-energy program relies on carefully controlled systematic uncertainties and well-understood radiological backgrounds, pertinent at the $\mathcal{O}(1-100)$ MeV domain.

This thesis presents two analyses. The first is a detailed examination of the radiological neutrons at DUNE. Neutron capture on argon can be confused with low-energy neutrino interactions. We know neutrons emanate from the cavern walls, aggregate construction materials and various types of steel, including those used within the DUNE cryostats. With improvements to the simulation geometry and energy spectra informed by elemental spectroscopy on material samples, the total neutron capture rate is estimated to be 3.05 ± 0.13 captures / 10 ktonne-second.

Secondly, the improvements required of a far detector module to observe CNO neutrinos are discussed. Inconsistencies in available solar neutrino data imply two possible neutrino fluxes relating to higher and lower solar metallicity models. Under DUNE's baseline configuration, CNO neutrino observation is unlikely. However, a low-background far detector module with improved systematic uncertainties would allow for an almost 5σ measurement of CNO neutrinos under a high metallicity model. Additionally, DUNE could separate the high from low metallicity model at a $> 3\sigma$ confidence level. This measurement would resolve the solar metallicity discrepancy.

Declaration

I hereby declare that this thesis has not been and will not be submitted in whole or in part to another university for the award of any other degree.

Signature:

Aran Borkum

Acknowledgments

First and foremost, I would like to extend my sincerest gratitude to my friend, supervisor, and fellow scotch whisky enthusiast, Prof. Simon Peeters. Working with you has been a pleasure for the last four years. You always made time for discussion, helped me navigate the gauntlet that is professional particle physics, and supported me through every endeavour that has come our way. I couldn't have asked to work with a better supervisor.

To my other fellow academics with whom I've had the pleasure of working at the University of Sussex alongside. Pierre, the man who took a premium economy seat on a flight back from Chicago and without whom many of my projects would have been insurmountable; Thiago, my partner in crime in all things DAQ. Sammy, thank you for getting me over the finish line; I'm sorry you have to inherit all my unfinished and *creatively* named projects. Tyler, who spring-boarded me into my favourite project of my entire degree, and with whom I've shared some of the most memorable (and difficult to remember) times. Charlie, Yibing and Brett, my 2018 cohort, we made it! Alex, the other guy who got a premium economy plane seat (I'm not bitter at all), thank you for always being there for me and letting me steal your desk.

I've met many fantastic people who have helped define the last four years of my life. The immeasurably positive Dom Brailsford without whom collaboration meetings would have been far less hilarious. My 2018 DISCnet cohort. I'll never forget our time in Edinburgh and Liphook.

This list would be incomplete without mentioning all my Brighton friends: Jack, Agostina, Esteban, Nacho, Javi, Beth, Murray and Rich. You guys have supported, teased, empowered, employed, and tolerated me for most of a decade, and I couldn't be more grateful. It's comforting to know someone will always be at Ed's. I couldn't have done it without all of your support.

To Eric, my best friend and the fairer half of Blondie and Curly. Starting as pool fanatics in the first year of our undergrads, then became lab partners for two years and finally grad students together. Thank you for asking me to be the best man at your wedding; I'm looking forward to many more misadventures, Afrikaans swearing battles, far-fetched business ideas and testing the theoretical limits of a Weber barbecue.

Finally, and most importantly, my amazing family. My wonderful girlfriend, Caili, thank you for the back hugs, the endless stream of support, coffee and food. I'm excited to see what adventures we go on together next. My brother, Mark, the original Dr Borkum. My sister, Laurian, thank you for tolerating me for three and a half years in a small house. I'm not sure we'll ever recover from descending into the fake language, lockdown-induced insanity, but a Caprese salad might help. Last but very much not least, my parents, Hilda and Steven. The words thank you don't come close to the gratitude that you deserve. You've supported and counselled me, built me up when I'm down; you're always there for me. I love you very much. I hope I continue to make you proud.

Preface

Below outlines the general content of each chapter forming this thesis. The analysis aims were a combination of suggestions by my supervisor, Prof Simon Peeters, co-coordinator of the Backgrounds Taskforce, and the organic evolution of those ideas. Some references included are documentation accessible only with DUNE registration. These references ensure credit gets given to the collaborators to whom it belongs. In each case, every effort gets made to ensure clarity within this thesis.

Chapter 1 discusses the motivation of this thesis.

Chapter 2 discusses the theory of neutrino physics. General information, such as oscillations and neutrino masses, are briefly discussed. Physics relevant to this dissertation, such as solar neutrinos, are discussed in detail. The neutrino theory and future experimental designs come from numerous sources, citing the relevant parties where appropriate.

Chapter 3 gives an overview of DUNE: the detector, components and physics goals. This chapter is based heavily on the work of the entire DUNE collaboration.

Chapter 4 begins with an overview of the radiological background signals at DUNE, emphasising those present in low-energy physics studies. Much of the discussion is the work of the extended DUNE collaboration. Following this is a discussion of the development of a far detector geometry and associated inputs. Lastly, there is a summary of the neutron simulation results in the far detector geometry. The development, implementation and analysis performed with the far detector geometry is solely the author's work. The associated inputs to the geometry are collaborative

achievements. The University of Sheffield is responsible for calculating neutron production spectra; the South Dakota School of Mines and Technology is responsible for numerous material and radiological assays.

Chapter 5 presents an analysis of solar neutrinos in the context of DUNE. The simulations executed and analyses performed are solely the work of the author. Simulation inputs, where relevant, are credited to the appropriate sources.

Chapter 6 presents a summary of this thesis. The conclusions and results from previous chapters get recapitulated, and the furthering of the analysis gets outlined.

Contents

List of Figures

List of Tables

Chapter 1

Introduction

"In theory there is no difference between theory and practice - in practice there is"

— Lawrence Peter"Yogi" Berra

Neutrinos are one of the most mercurial and intriguing particles in the Standard Model of particle physics. Initially conceptualised as a solution to a violation of angular momentum, their prevalence in particle physics has snowballed. Initially, neutrinos were considered massless. However, this was disproven by the observation of neutrino oscillations. Now they may reveal why we live in a matter-dominated universe.

The parameters and characteristics governing the behaviour of neutrinos are relatively well known. Questions, such as *"What is the heaviest neutrino?"* and *"Are neutrinos also their antiparticle?"* are still unknown. Answers to these questions will likely emerge with the next generation of neutrino experiments.

Neutrinos provide answers to pressing questions in astronomy. Detection of neutrinos emanating from core-collapse supernovae provides a direct probe into the collapse mechanism, gives information about the progenitor, and reveals the outcome of the collapse. A measurement of neutrinos from the Sun, which once catalysed the discovery of neutrino oscillation, could reveal the Sun's intrinsic metallicity.

The first analysis presented in this thesis concerns the radiological backgrounds relevant to low-energy physics studies at DUNE. To detect supernova or solar neutrinos, one must understand any background as clearly as possible. An overhaul of the radiological background simulation and re-analysis of background levels provide the best estimation of the neutron capture background DUNE can expect to see. The results of the background analyses directly inform the second study: solar neutrinos at DUNE. An evaluation of DUNE's ability to measure CNO and ^{8}B neutrinos under

carefully considered modifications gets presented. As an extension, assuming CNO measurement capabilities, we evaluate DUNE's ability to measure the Sun's intrinsic metallicity.

Chapter 2

Neutrino Physics

"There, now, for the first time, we may be able to see the infinitesimal fabric of matter itself, laying bare the most fundamental laws of the universe."

— H. J. Farnsworth

2.1 History of the neutrino

2.1.1 Pauli's prediction

The neutrino was first proposed in 1930 by Wolfgang Pauli [24] in an effort to explain how beta decay could conserve energy, momentun and angular momentum. Beta decay, which was thought to be a two body problem of the form

$$X \rightarrow Y + e^{-}, \tag{2.1}$$

predicted that the emitted electron must have a fixed energy based on the two other particles in the process. That energy, in natural units ($c \equiv \hbar \equiv 1$), would be given by

$$E_{e^-} = \frac{m_X^2 - \left(m_Y^2 + m_{e^-}^2\right)}{2m_X^2}. \tag{2.2}$$

Observation, however, showed that the emitted electron's energy followed a distribution with the energy calculated in Equation 2.2 representing the maximum possible energy. This spectrum is shown in Figure 2.8. To resolve this issue, Pauli suggested the existence of a new particle which he named the *neutron*, employing the same *-on* ending motif used in the naming of the proton and electron. Pauli put forth that this new neutral particle was emitted from the nucleus together with the electron during beta decay [25].

In 1932, James Chadwick discovered a new massive elementary particle with no charge that he also named the neutron [26]. Initially, Pauli considered his neutral particle that resolved the beta decay issue and Chadwick's particle to be the same. This nomenclature did not last very long as Edoardo Amaldi coined the term

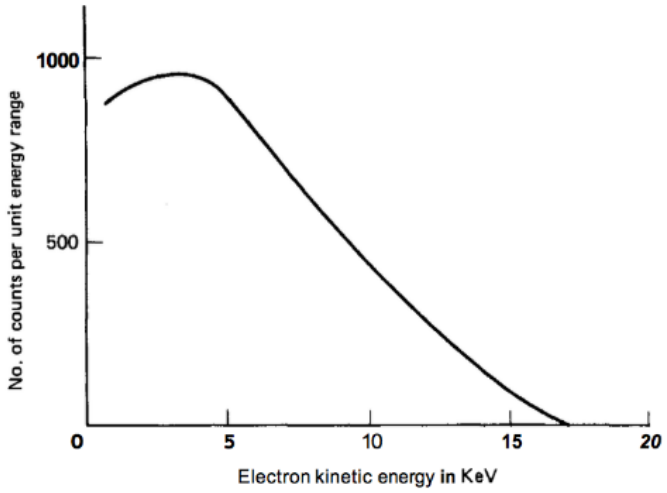

Figure 2.1: Electron energy spectrum produced by beta decay [1]

neutrino, which in Italian means "little neutral one", which officially entered the scientific lexicon in July of 1932 when Enrico Fermi used the term in a Paris conference. From then on then on neutrino and neutron referred to Pauli's light and Chadwick's heavy neutral particles respectively [27].

2.1.2 Direct neutrino detection

In 1942, an experiment involving beta capture was put forward as a way of directly detecting neutrinos [28]. A series of experiments by Clyde Cowan and Frederick Reines, from 1953-1956, tested the neutrino hypothesis and later confirmed its existence. In 1995 they recieved the Nobel Prize for their work, almost four decades after publishing their discovery.

The Cowan-Reines neutrino experiment made use of liquid scintilator detectors [29], a new technology for the time. Their experiment [30] was designed to study the anti-neutrinos that were produced from the Hanford nuclear reactor in Washington, U.S.A., through inverse beta decay;

$$\bar{\nu_e} + p \rightarrow e^+ + n. \tag{2.3}$$

The observable signals being searched for were the two gamma rays produced by electron-positron annihilation, and then the gamma emission associated with neutron capture. The initial results of the 1953 experiments [31] showed a small excess over the background predictions, however the backgrounds measured were much larger than expected. This was attributed to underestimating the effects of cosmic rays. In 1956 another experiment was conducted, this time 12 m underground to mitigate the effects of cosmic rays, by the Savannah River reactor in South Carolina. This time a neutrino detection rate of 2.9 ± 0.2 per hour was recorded which was over 20 times larger than the accidental background rate [32]. This experiment confirmed the existance of neutrinos.

In 1959, Raymond Davis conducted an experiment to test the notion of neutrino-antineutrino identity. Using a 3000 gallon carbon tetrachloride detector he searched for the interaction

$$\bar{\nu} + {}^{37}\mathrm{Cl} \rightarrow {}^{37}\mathrm{Ar} + e^-. \tag{2.4}$$

It was known from the Cowan-Reines expeiment that inverse beta decay occurs, so this experiment would probe the difference between neutrinos and antineutrinos, should one exist. Davis found that the interaction rate for the process shown in Equation 2.4 was 20 times less than expected when assuming neutrino-antineutrino

identity, implying a fundamental difference between the two particles. Furthermore, this experiment gave rise to the concept of lepton number and lepton number conservation in physical interactions.

The next addition into the growing family of neutrinos came in 1962 from the discovery of the muon neutrino [33]. Muon decay of the form

$$\mu^- \rightarrow e^- + \gamma \tag{2.5}$$

was thought to be allowed, however it was never observed. This inspired the idea of two distinct neutrino flavours. To test this, Lederman, Steinberger and Schwartz used a muon beam with the intent of studying two interactions:

$$\bar{\nu_\mu} + p \rightarrow \mu^+ + n, \tag{2.6}$$

$$\bar{\nu_\mu} + p \rightarrow e^+ + n. \tag{2.7}$$

The idea here is that with only one neutrino type the two interactions would occur at the same rate. To produce the neutrinos protons were accelerated to 15 GeV which struck a beryllium target. This produced a spill of mesons that would, in turn, decay producing neutrinos of energies up to $\sim$1 GeV. In the end, 34 muon events were recorded (five of which were attributed to cosmic backgrounds) and no electron events were observed. This experiment not only proved the existence of a second neutrino flavour, but also paved the way for experiments using an artificial neutrino beam; a standard in modern neutrino experiments.

The third generation of lepton, the τ lepton, was discovered by Martin Perl and his colleagues at the Stanford Linear Accelerator Center (SLAC) in 1975 [34]. Events of the form

$$e^+ + e^- \rightarrow e^\pm + \mu^\pm + \geq 2 \text{ undetected particles.} \tag{2.8}$$

Using the angular and energy distributions they saw that at least two additional particles must be present in these interactions. No conventional explanation could rationalise these events, and so they proposed the existence of a new heavy charged lepton. This would act as an intermediates stage in the reaction,

$$e^+ + e^- \rightarrow \tau^+ + \tau^- \rightarrow e^\pm + \mu^\pm + 4\nu. \tag{2.9}$$

It was difficult to verify this as the energy required to produce a $\tau^-\tau^+$ pair is similar to the threshold for the D-meson. Eventually, the mass and spin of the τ-lepton was established with the SPEAR direct electron counter at SLAC and the Double Arm Spectrometer (DASP) at DESY [35, 36]. Given the pattern of lepton and associated neutrino it was a natural extension from the discovery of the τ-lepton to assume the existence of the τ-neutrino.

In 1989 the Large Electron-Positron Collider (LEP) at CERN brought further evidence for the existence of a third neutrino flavour. Four experiments were being undertaken, all of which were studying the Z^0 boson which had been discovered a few years earlier in 1983 [37–40]. Theoretically, the Z^0 boson resonance width, Γ_Z, is dependent on the contributing partial widths of final state leptons, hadrons and neutrinos. One can characterise this as

$$\Gamma_Z = \Gamma_{ee} + \Gamma_{\mu\mu} + \Gamma_{\tau\tau} + N_\nu \Gamma_\nu + \Gamma_{\text{hadrons}}, \tag{2.10}$$

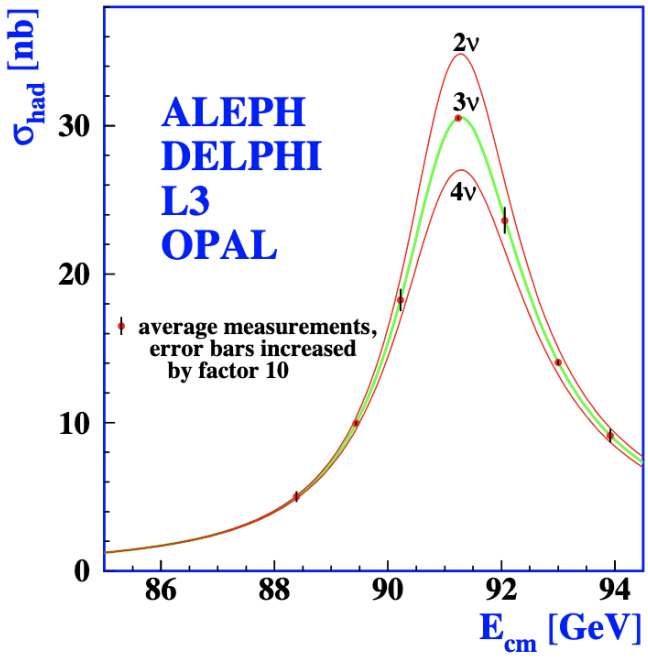

Figure 2.2: Measurements of the hadron production cross-section around the Z resonance.The curves indicate the predicted cross-section for two, three and four neutrino species with SM couplings and negligible mass [2].

where N_ν is the number of neutrino neutrino flavours. One can produce predictions for the shape of the Z^0 resonance for different numbers of neutrino flavours, as shown in Figure 2.2. By fitting to experimental data it was determined that the closest fit corresponds to a value of $N_\nu = 2.984 \pm 0.008$ [2].

Despite the overwhelming nature of the evidence it wasn't until the year 2000 that the Direct Observation of NuTau (DONUT) experiment at Fermilab reported direct detection of the τ-neutrino [41]. As the name implies, DONUT was designed for the sole purpose of discovering the τ-neutrino. A ν_τ beam was created by firing 800 GeV protons from the Tevatron at a tungsten beam dump. The mean energy of the neutrino beam was 111 GeV, produced as a result of D_S meson decay to a τ lepton

and a $\bar{\nu_\tau}$, which is then followed by the decay of the τ-lepton which produces a ν_τ. This experiment yielded four events, significantly over the 0.34 ± 0.05 background, consistent with the predictions of the τ-neutrino from the Standard Model.

2.1.3 The Solar Neutrino Problem

In the 1930s, when Hans Bethe was developing the theory of stellar nucleosynthesis [42], it was known that electron neutrinos would be produced in abundance by the process that powers the Sun. Later, in 1968, John Bahcall established the Standard Solar Model (SSM) [43] which describes the process of nuclear fusion that ultimately powers stars. In relatively small stars, like our Sun, this process is dominated by the proton-proton chain where four hydrogen atoms and two electrons interact producing a helium nucleus, two electron neutrinos and around 27 MeV of energy. Larger stars follow the CNO cycle, which produces elements including carbon, nitrogen and oxygen, hence the abbriviation *CNO*. A majority of the energy produced in these processes is lost via photons, however a small amount is carried away by the resultant neutrinos. The spectra for the p-p chain, CNO cycle and other known processes is shown in Figure 2.3.

The first experiment undertaken to directly observe solar neutrinos began in 1968, conducted by Ray Davis in collaboration with Bahcall. A 380 m^3 tank of tetrachloroethene was commissioned to detect neutrinos via inverse beta decay. In order to combat the backgrounds, mainly from cosmic rays, the experiment was built 4850 ft underground at the Homestake mine in Lead, South Dakota. Interestingly, the Homestake mine was, until its closure in 2002, the largest and deepest gold mine in North America, responsible for the unearthing of over 1.2 million kilograms of

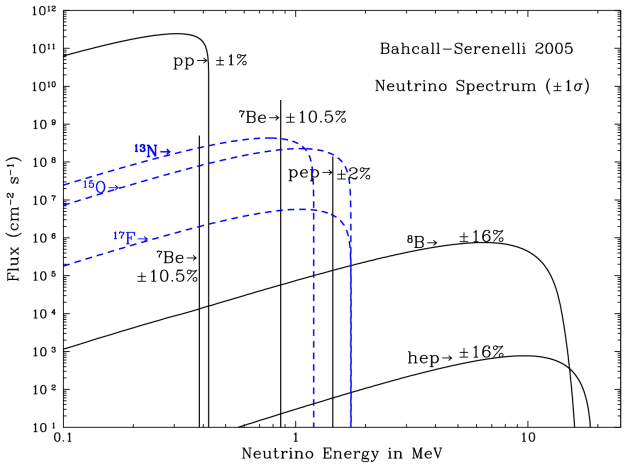

Figure 2.3: Solar neutrino energy spectrum for the solar model BS05(OP) [3].

gold over its lifetime. The experiment ran for 25 years, however the results gave rise to what is now known as the Solar Neutrino Problem. The solar neutrino flux measured disagreed significantly with the predictions of the SSM [44]. The experiment measured around a third of the electron flux predicted by the SSM [45]. This missing flux was measured again by the SAGE and GALLEX experiments, reporting neutrino capture rates of $66.6^{+6.8+3.8}_{-7.1-4.0}$ SNU and $77.5 \pm 6.2^{4.3}_{-4.7}$ SNU respectively, where 1 SNU is defined as the equivalent neutrino flux producing 10^{-36} captures per target atom per second.

There are two conclusions to be made from the three experiments described. One conclusion is that the SSM was incomplete, which leads to the erroneous over-prediction of the solar electron neutrino flux. The second, and more positive, is that there is new physics to discover as motivated by the experimental data. This "new physics" ultimately solved the solar neutrino problem and has since become the leading study in neutrino physics (detailed discussion in Section 2.2).

2.1.4 Atmospheric Neutrino Deficit

Cosmic rays interacting with the upper atmosphere produce many particles. These particles generally must decay, producing an outpour of new particles, ultimately resulting in the production of neutrinos. The term "atmospheric neutrino" describes neutrinos produced in these interactions. The typical chain of interactions producing atmospheric neutrinos is as follows [46]:

$$\pi^+ \to \mu^+ + \nu_\mu, \qquad \mu^+ \to e^+ + \bar{\nu}_e + \nu_\mu, \tag{2.11}$$

$$\pi^- \to \mu^- + \bar{\nu}_\mu, \qquad \mu^- \to e^- + \nu_e + \bar{\nu}_\mu. \tag{2.12}$$

Detectors in deep mines in South Africa and India first observed atmospheric neutrinos in the 1960s [47,48]. Both detectors detected muons travelling horizontally which could not be rationalised as cosmic muons, as they could not reach such depths. The explanation for these unusual muons was neutrinos from all directions interacting and producing the muons. The kinematics and decay lengths of particles within the detectors are well understood, meaning one can predict the ratio of electron to muon neutrinos to high accuracy. Ultimately, one can compare the measured ratio to that predicted by the physical model used and determine the model's efficacy.

Understanding the atmospheric neutrino flux is integral for nucleon decay experiments as it represents a significant background. Two of the most significant of these experiments are the Irvine-Michigan-Brookhaven (IMB) experiment and Kamioka nucleon decay experiment (KamiokaNDE), both attempting to study proton decay in the 1980s. IMB and KamiokaNDE are both water Cherenkov detectors. The ring

of light produced within one of these detectors is easily classifiable as muon-like or electron-like. Muon rings are sharply defined, whereas electron rings are fuzzy as the lighter electron scatter more, resulting in electromagnetic showers. Determining lepton flavour also determines the specific neutrino that interacted in the detector and, therefore, the electron to muon neutrino ratio from atmospheric neutrinos. These experiments both saw a deficit in the number of muon neutrinos compared to predictions, which came to be known as the atmospheric neutrino deficit.

Numerous experiments measuring the atmospheric neutrino flux produced similar measurements to that of IMB and KamiokaNDE. Some implied an excess in electron neutrinos and some a deficit in muon neutrinos. Some even reported a combination of the two. This inconsistency, in combination with the solar neutrino problem, as discussed in 2.1.3, strongly suggested that our theoretical understanding of neutrinos is incomplete. The theoretical resolution to these issues is neutrino oscillation, which requires a significant modification to the Standard-Model and implies neutrinos have mass.

2.2 Neutrino Oscillation

Neutrino oscillations describe the changing of a neutrino's flavour as it propagates through space and time. Mathematically, there is a non-zero probability of a neutrino generated with a particular flavour to be detected having a different flavour state. First conceptualised in 1957 by Bruno Pontecorvo as an analogous phenomena to $K^0 \rightarrow \bar{K}^0$ oscillation in the quark sector [49, 50]. Neutrino oscillations are a practical

solution to the solar neutrino problem and atmospheric neutrino anomaly. One can postulate that the missing neutrinos have oscillated to a different, undetectable flavour.

2.2.1 Majorana particles and the seesaw mechanism

The theory of Majorana fermions dates back to 1937 [51] where the eponymous Ettore Majorana posited that electrically neutral spin-$\frac{1}{2}$ particles can be described by a real-valued wave equation. As a consequence, these particles would be identical to their antiparticles.

Mathematically, one expresses the difference between Dirac and Majorana fermions as follows. The creation operator, $\gamma_i^\dagger$, creates a fermion in quantum state i. Similarly, the annihilation operator γ_i annihilates this particle. Equivalently, the annihilation operator "creates" an antiparticle in quantum state i. For Dirac fermions, $\gamma_i^\dagger$ and γ_i are different, whereas, for Majorana fermions, they are identical. By extension, the general fermionic creation and annihilation operators in terms of two Majorana operators are given by:

$$f = \frac{1}{\sqrt{2}}(\gamma_1 + i\gamma_2), \tag{2.13}$$

$$f^\dagger = \frac{1}{\sqrt{2}}(\gamma_1 - 1\gamma_2). \tag{2.14}$$

Among the fundamental particles, the only candidate Majorana particles are theoretical sterile neutrinos. Regular left-handed neutrinos and right-handed antineutrinos have a non-zero weak isospin quantum number, $T_3 = \pm\frac{1}{2}$. A fundamental Majorana

particle requires zero-valued quantum numbers for all conserved charge-like quantities. Were sterile neutrinos to exist, the antiparticles would be left-handed, and the particles would be right-handed.

Majorana fermions could explain the anomalously small neutrino mass if they also had Majorana masses. In theory, via the seesaw mechanism, the neutrino fields would behave as six Majorana fields, with three having the low masses, $(O)(< 1\text{eV})$, as observed in modern experiments, and three with very high masses, comparable to the GUT scale.

The neutrino mass Lagrangian goes as

$$\mathcal{L}_{\text{mass}} \sim \begin{pmatrix} \overline{\nu_L^C} & \overline{N_R} \end{pmatrix} \begin{pmatrix} m_L & m_D \\ m_D & m_R \end{pmatrix} \begin{pmatrix} \nu_L \\ N_R^C \end{pmatrix} + h.c. \tag{2.15}$$

where $\begin{pmatrix} \overline{\nu_L^C} & \overline{N_R} \end{pmatrix}$ contains the right-handed fields, $\begin{pmatrix} \nu_L \\ N_R^C \end{pmatrix}$ the left-handed fields and

$$M = \begin{pmatrix} m_L & m_D \\ m_D & m_R \end{pmatrix} \tag{2.16}$$

represents the mass matrix with $L,\ D,$ and R denoting the left-handed, Dirac and right-handed mass terms. Suppose the following conditions are satisfied:

$$m_D \ll m_R,\ m_L = 0. \tag{2.17}$$

The mass matrix takes the form

$$M = \begin{pmatrix} 0 & m_D \\ m_D & m_R \end{pmatrix} \tag{2.18}$$

with eigenvalues

$$\lambda_{\pm} = \frac{m_R \pm \sqrt{m_R^2 - 4m_D^2}}{2}. \tag{2.19}$$

Since the geometric mean of the eigenvalues is $|m_D|$, the eigenvalues get simplified to

$$\lambda_+ \simeq m_R,\ \lambda_- \simeq -\frac{m_D^2}{m_R}. \tag{2.20}$$

Therefore, λ_+ is as heavy as the sterile right-handed, which has a mass comparable to the GUT scale. By extension, λ_- compensates this by having a mass on the electroweak scale. This process of heavy and light compensatory masses is the famous "*see-saw*" mechanism [52], which provides a plausible explanation of the anonymously small observed neutrino masses.

2.2.2 Theory of Neutrino Oscillations

Vacuum Oscillations

Neutrino oscillation is due to the mixing between flavour and mass eigenstates of neutrinos. Additionally, neutrinos interact in their flavour eigenstates but propagate as their mass eigenstates. Therefore, a neutrino interaction is a superposition of three (or more if there are more neutrino eigenstates) neutrino mass states.

The theoretical development of neutrino oscillations began with Pontecorvo and continued with Ziro Maki, Masami Nakagawa, and Shoichi Sakata [53]. Essentially, if the mass states are the true stationary states of the Hamiltonian, the flavour states are linear superpositions of the mass states:

$$\begin{pmatrix} \nu_e \\ \nu_\mu \\ \nu_\tau \end{pmatrix} = U^*_{\text{PMNS}} \begin{pmatrix} \nu_1 \\ \nu_2 \\ \nu_3 \end{pmatrix}. \tag{2.21}$$

Here, U^*_{PNMS} represents the PMNS mixing matrix which defines the flavour composition of a given mass state. The PNMS mixing matrix is not diagonal; otherwise, neutrino oscillation would not occur as each mass state would correspond to a single flavour state.

A given flavour state is definable as a superposition of mass states,

$$|\nu_\alpha\rangle = \sum_i U^*_{\alpha i} |\nu_i\rangle, \tag{2.22}$$

and a given mass state is similarly definable as a superposition of flavour states,

$$|\nu_i\rangle = \sum_\alpha U_{\alpha i} |\nu_\alpha\rangle. \tag{2.23}$$

When assuming three neutrino flavours, the PNMS matrix gets represented as a decomposition into a combination of three unitary rotation matrices.

$$U_{\alpha i} \equiv \underbrace{\begin{pmatrix} 1 & 0 & 0 \\ 0 & c_{23} & s_{23} \\ 0 & -s_{23} & c_{23} \end{pmatrix}}_{\text{Atmospheric}} \underbrace{\begin{pmatrix} c_{13} & 0 & e^{-i\delta}s_{13} \\ 0 & 1 & \\ -e^{-i\delta}s_{13} & 0 & c_{13} \end{pmatrix}}_{\text{Reactor or Accelerator}} \underbrace{\begin{pmatrix} c_{12} & s_{12} & 0 \\ -s_{12} & c_{12} & 0 \\ 0 & 0 & 1 \end{pmatrix}}_{\text{Solar}}, \tag{2.24}$$

where $c_{ij} \equiv \cos(\theta_{ij})$, $s_{ij} \equiv \sin(\theta_{ij})$ and δ is a CP-violating phase required to account for the different oscillation probabilities observed between neutrinos and antineutrinos. Here, θ_{ij} is the neutrino mixing angle between two mass eigenstates. Their names refer to the neutrino fields of study where they are most applicable.

A neutrino of flavour α is a superposition of mass states and propagates as a plane wave through space and time, such that

$$|\nu_i(x,t)\rangle = |\nu_i(0)\rangle e^{-i\mathbf{x}\cdot\mathbf{p}}, \tag{2.25}$$

where $\mathbf{x}$ and $\mathbf{p}$ are the 4-position and momentum of the neutrino respectively. Given Equations 2.22 and 2.25, we can write the evolution of the neutrino flavour over space and time as

$$|\nu_\alpha(x,t)\rangle = \sum_i U^*_{\alpha i}|\nu_i(0)\rangle e^{-i\mathbf{x}\cdot\mathbf{p}}. \tag{2.26}$$

In the ultra-relativistic limit, implying the mass of the neutrino is negligible compared to its momentum ($|\vec{p}_i| \gg m_i$)

$$E_i = \sqrt{|\vec{p}|^2 + m_i^2} = \vec{p}\sqrt{1 + \frac{m_i^2}{|\vec{p}|^2}} \approx \vec{p} + \frac{m_i^2}{2\vec{p}} \tag{2.27}$$

and

$$\mathbf{x}\cdot\mathbf{p} = E_i t = \vec{x}\cdot\vec{p} = \vec{p}\cdot t + \frac{m_i^2 t}{2\vec{p}} - \vec{x}\cdot\vec{p} \approx \frac{m_i^2}{2\vec{p}}\vec{x} = \frac{m_i^2}{2p}x. \tag{2.28}$$

Combining Equations 2.23, 2.26 and 2.28 we get

$$\begin{aligned} |\nu_\alpha(x,t)\rangle &= \sum_i U^*_{\alpha i}|\nu_i(0)\rangle e^{-i\frac{m_i^2}{2p}x} \\ &= \sum_i \sum_\beta U^*_{\alpha i} e^{-i\frac{m_i^2}{2p}x} U^*_{\beta i}|\nu_\beta\rangle. \end{aligned} \tag{2.29}$$

Determining the probability of observing a neutrino created with flavour α as flavour β is an extension of Equation 2.29:

$$\begin{aligned} P(\alpha\to\beta) &= |\langle\nu_\alpha|\nu_\beta(x,t)\rangle|^2 \\ &= \left[\sum_i U_{\alpha i} e^{i\frac{m_i^2}{2p}x} U^*_{\beta i}\right]\left[\sum_j U^*_{\alpha j} e^{-i\frac{m_j^2}{2p}x} U^*_{\beta j}\right] \\ &= \sum_{i,j} U_{\alpha i} U^*_{\alpha j} U_{\beta i} U^*_{\beta j} e^{i\frac{m_i^2 - m_j^2}{2p}x}. \end{aligned} \tag{2.30}$$

The probability is dependent on four parameters: the neutrino momentum, the difference of the squared masses of the flavour states, the propagation distance and the mixing parameters in the U matrix.

DUNE is an accelerator-based neutrino experiment, generally producing a muon-neutrino beam. Often, one would look for electron appearance and muon disappearance in such an experiment. The probability of each, still assuming the relativistic limit, is approximated as

$$P(\nu_\mu \to \nu_e) \approx \sin^2 2\theta_{13} \sin^2 \theta_{23} \sin^2 \left(1.27 \frac{\Delta m^2_{13} L}{E}\right), \tag{2.31}$$

$$P(\nu_\mu \to \nu_\mu) \approx 1 - \cos^4 \theta_{13} \sin^2 2\theta_{23} \sin^2 \left(1.27 \frac{\Delta m^2_{23} L}{E}\right), \tag{2.32}$$

respectively. Here, $\Delta m^2_{ij} = m^2_i - m^2_j$ is the mass squared splitting in eV^2, L is the propagation distance in km and E is the neutrino energy in GeV.

These equations contain two important, controllable parameters for designing an oscillation experiment: the distance travelled and the energy of the neutrinos. For a given distance, approximately 1,300 km in the case of DUNE, one can configure the beam energy to maximise the predicted oscillations. In turn, this allows for more precise measurements over the duration of the experiment.

Matter Effects on Neutrino Oscillations

Oscillation theory, thus far, pertains only to neutrinos travelling in a vacuum. Vacuum oscillation theory does not, in general, account for observations made by solar neutrino experiments[1]. The Sudbury Neutrino Observatory (SNO) collaboration observed more oscillations than expected via the vacuum oscillation model[2] [55, 56]. In response to these observations, the concept of matter effects on neutrino oscillation arose. Simply put, the matter effect on neutrino oscillation is analogous to the electromagnetic phenomena leading to refractive indices of light in a dense medium.

[1] Low energy solar neutrino signals, such as *pp* neutrinos, are largly uneffected by matter effects.

[2] This ignores the *just-so* solution where the neutrino oscillation parameters are tuned precicely to replicate the observation [54].

Charge current coherent forward scattering of electron neutrinos results in changes to the energy levels of the mass eigenstates of neutrinos propagating through a medium. As a result, the effective mass of a neutrino propagating through a dense medium is different to when it propagates through a vacuum. Equation 2.30 shows oscillation probability depends on the difference of the square of the neutrino masses. Therefore, if the masses change depending on the propagation medium, the oscillation probability changes accordingly. Within the Sun, the density is such that neutrinos experience a resonance, causing their oscillation probability to increase dramatically compared to vacuum oscillations.

The variation in neutrino oscillation due to propagation through matter is called the Makheev-Smirnov-Wolfstein (MSW) effect [57, 58]. The MSW effect is critical when studying solar neutrinos, not only for the Sun's matter effect but also the effect the Earth has on propagating neutrinos. Observing neutrinos at different times of day leads to variation in data collected by experiments hoping to study solar neutrinos. Additionally, since the universe is predominantly composed of matter and not antimatter, the MSW effect is different for neutrinos and anti-neutrinos.

2.2.3 CP Violation

The PMNS matrix includes the term δ, denoting the CP-violating phase factor. We know the neutrino mixing angles are non-zero implies there is scope for CP-violation in the lepton sector.

Probing CP violation is a central goal of neutrino physics. We live in a universe made almost entirely of matter and not anti-matter. Evaluating CP violation asks the question *why is there so much matter and practically no anti-matter?* An explanation for this is that a CP-violating process must have occurred in the early universe, resulting in the observed imbalance [59].

The first evidence for CP-violation came from studying kaon decay [60]. Cronin and Fitch showed that neutral kaon decays, which are weak interactions, violate CP-symmetry. In theory, CP-violation in QCD interactions is possible, but no observation has been made [61]. Observation of leptonic CP violation, assuming the amount of CP violation is sufficiently large, could explain the baryonic asymmetry in our universe [62, 63]. Furthermore, if neutrinos are Majorana fermions, two additional CP-violating phases could be added to the PNMS matrix, introducing an additional CP-violation contribution.

Matter-antimatter asymmetry occurs, via leptogenesis, as a result of CP-violation in the lepton sector. Were future experiments to confirm CP-violation in the lepton sector, leptogenesis would become the preferred explanation for matter-antimatter asymmetry in the Standard Model. However, if leptonic CP-violation is too small, it would imply new beyond the Standard Model physics.

2.2.4 Observation of Neutrino Oscillations

Atmospheric Neutrino Oscillations

The Kamiokande experiment stated results in 1994 indicating an angular dependence for the R-ratio deficit [64]. Here, the R-ratio is defined as $(\mu/e)_{\mathrm{DATA}}/(\mu/e)_{\mathrm{MC}}$ where μ and e are the number of μ-like and e-like events observed. An angular dependence implies measuring the R-ratio also depends on the neutrino travel distance. Kamiokande's observation is explainable if one considers neutrino oscillations, as the oscillation probability is dependent on the propagation distance. Super-Kamiokande, the next generation experiment following Kamiokande, was constructed to precisely measure this phenomenon.

Located 1000 meters below ground, Super-K is a 22.5 kilo-tonne volume of pure water, surrounded by a photomultiplier array and a 40% coverage of photocathodes. At the time, Super-K had ten times the amount of pixels compared to other competing experiments In 1998, Super-K confirmed that the R-ratio does indeed have an angular dependence. Super-K also considered their data as a function of neutrino energy and propagation distance. The results acquired were consistent with the two-flavour neutrino oscillation model between muon and tau flavour, $\nu_\mu \rightarrow \nu_\tau$. Famously, this result is the first published claim for the experimental discovery of neutrino oscillations [4].

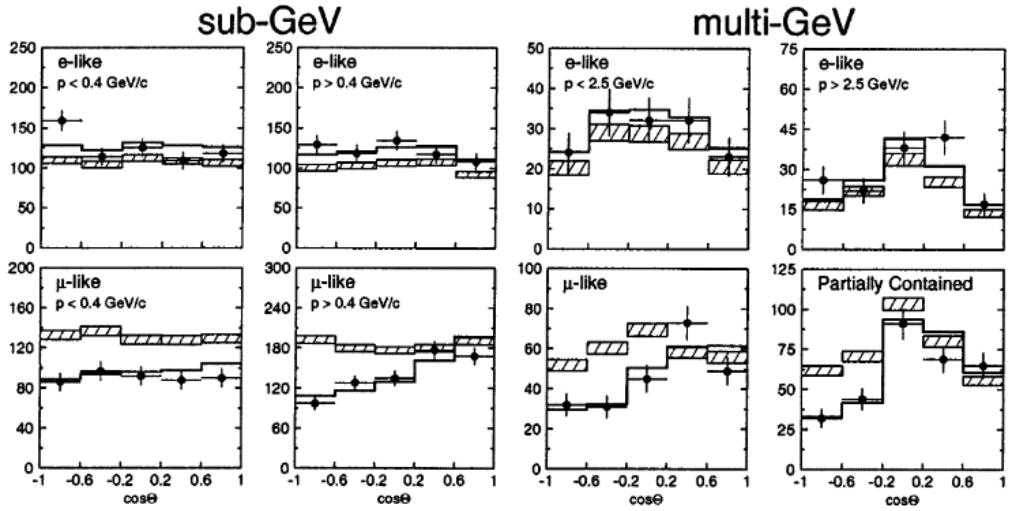

Figure 2.4: Zenith angle distribution of μ-like and e-like events for sub-GeV and multi-GeV data sets. Upward-going particles have $\cos\Theta < 0$ and downward-going particles have $\cos\Theta > 0$. Sub-GeV data are shown separately for $p < 400$ MeV/c and $p > 400$ MeV/c. Multi-GeV e-like distributions are shown for p ¡ 2.5 and p ¿ 2.5 GeV/c and the multi-GeV μ-like are shown separately for FC and PC events. The hatched region shows the Monte Carlo expectation for no oscillations normalised to the data live time withs statistical errors. The bold line is the expectation for $\nu_\mu \leftrightarrow \nu_\tau$ oscillations with the overall flux normalisation fitted as a free parameter. Taken from [4].

Solar Neutrino Oscillations

Given the results from Super-Kamiokande, it was clear that neutrino oscillations could explain the electron neutrino deficit observed in solar neutrino experiments. The final nail in the coffin comes from SNO with a conclusive measurement of the ^{8}B solar neutrino flux.

Similarly to Super-K, SNO is a water Cherenkov detector with one key difference. Instead of using pure water, SNO uses heavy water (D_2O), replacing hydrogen with deuterium. The heavy water is contained within a 12-meter spherical acrylic shell, surrounded by a photomultiplier array.

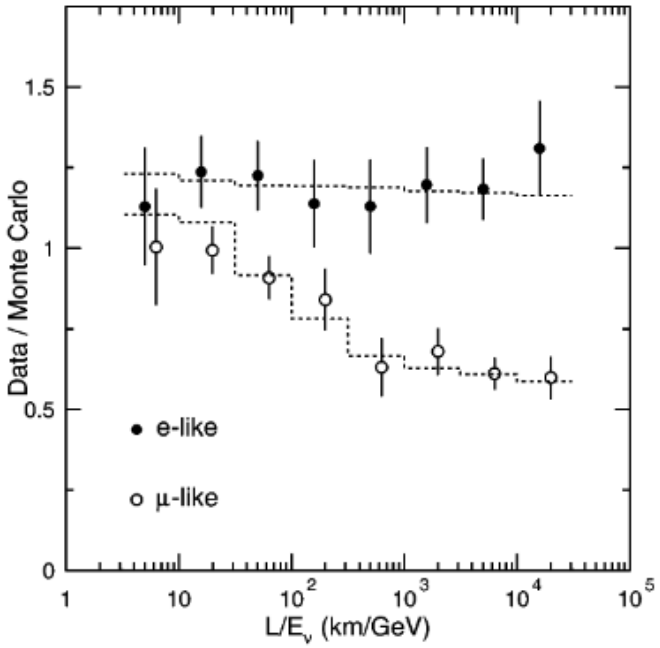

Figure 2.5: The ratio of the number of FC data events to FC Monte Carlo events versus reconstructed L/E_ν. The points show the ratio of the observed data to MC expectation in the absence of oscillations. The dashed lines show the expected shape for $\nu_\mu \leftrightarrow \nu_\tau$ at $\Delta m^2 = 2.2 \times 10^{-3}$ eV^2 and $\sin^2 2\theta = 1$. The slight L/E_ν dependence for e-like events is due to contamination (2-7%) of ν_μ CC interactions. Taken from [4].

The use of deuterated water facilitates SNO the sensitivity to neutrino interaction channels, unavailable to Super-K. These include the charge current (CC), neutral current (NC) and elastic scattering (ES) interactions:

$$\nu_e + d \rightarrow 2p + e^- \tag{2.33}$$

$$\nu_x + d \rightarrow p + n + \nu_x \tag{2.34}$$

$$\nu_x + e^- \rightarrow \nu_x + e^- \tag{2.35}$$

As denoted by the subscript on the neutrino in equations 2.33-2.35, the charge current interaction is specifically sensitive to electron neutrino interactions. Neutral current and elastic scattering interactions are flavour agnostic. As a result, SNO was uniquely able to measure the electron neutrino interaction rate and the total neutrino interaction rate simultaneously.

SNO measured the neutrino flux components [65] to be:

$$\begin{aligned} \phi_{\mathrm{CC}}^{\mathrm{SNO}} &= 1.59^{+0.08}_{-0.07}(\mathrm{stat.})^{+0.06}_{-0.08}(\mathrm{sys.}), \\ \phi_{\mathrm{ES}}^{\mathrm{SNO}} &= 2.21^{+0.31}_{-0.26}(\mathrm{stat.}) \pm 0.10(\mathrm{sys.}), \\ \phi_{\mathrm{NC}}^{\mathrm{SNO}} &= 5.21 \pm 0.27(\mathrm{stat.}) \pm 0.38(\mathrm{sys.}). \end{aligned} \tag{2.36}$$

The electron neutrino flux measured was roughly a third of the total neutrino flux, consistent with previous measurements. These results are conclusive: the SSM is correct, and the neutrinos from the sun are experiencing oscillation effects. The neutrinos are not disappearing.

One must make a syntactical distinction regarding the SNO measurements. Neutrino oscillations were not measured, as no consideration of the L/E dependence was taken. Instead, SNO measured the electron component of m_2 neutrino mass eigenstate.

2.3 Solar neutrinos

Solar neutrinos refer to any neutrino coming from the Sun, generated as a byproduct of nuclear fusion in the Sun's core. The detection of solar neutrinos is uniquely challenging as, for the most part, they have very low energies in the region of 0.1-18 MeV.

There have been great strides in solar neutrino study in recent years, but there is still much more to discover. This section will discuss four of the most important solar neutrino modes of interest to DUNE, ^{8}B, HEP, *pep* and CNO neutrinos.

2.3.1 Solar neutrino interactions in liquid argon

Three nuclei-scattering processes govern the neutrino interactions on liquid argon. There are two charged-current interactions:

$$\begin{aligned} \nu_e + {}^{40}\mathrm{Ar} &\rightarrow e^- + {}^{40}\mathrm{K}^*, \\ \bar{\nu}_e + {}^{40}\mathrm{Ar} &\rightarrow e^+ + {}^{40}\mathrm{Cl}^*. \end{aligned} \tag{2.37}$$

In these interactions, neutrinos (or antineutrinos) scatter on argon nuclei producing their associated lepton and a potassium (or chlorine) isotope in an excited state. The name "charged current" indicates the interaction is mediated by a charged vector boson, the $W^{\pm}$. In addition, neutral current interactions mediated by the Z^0 boson are possible,

$$\overset{(-)}{\nu} + {}^{40}\mathrm{Ar} \rightarrow \overset{(-)}{\nu} + {}^{40}\mathrm{Ar}^*. \tag{2.38}$$

Neutrinos also undergo elastic scattering on atomic electrons,

$$\overset{(-)}{\nu} + {}^{40}\mathrm{Ar} \rightarrow \overset{(-)}{\nu} + {}^{40}\mathrm{Ar}. \tag{2.39}$$

The direction of the electron recoil and incoming neutrino are highly correlated, allowing for the reconstruction of the neutrino source direction, which is particularly interesting for supernova studies [66].

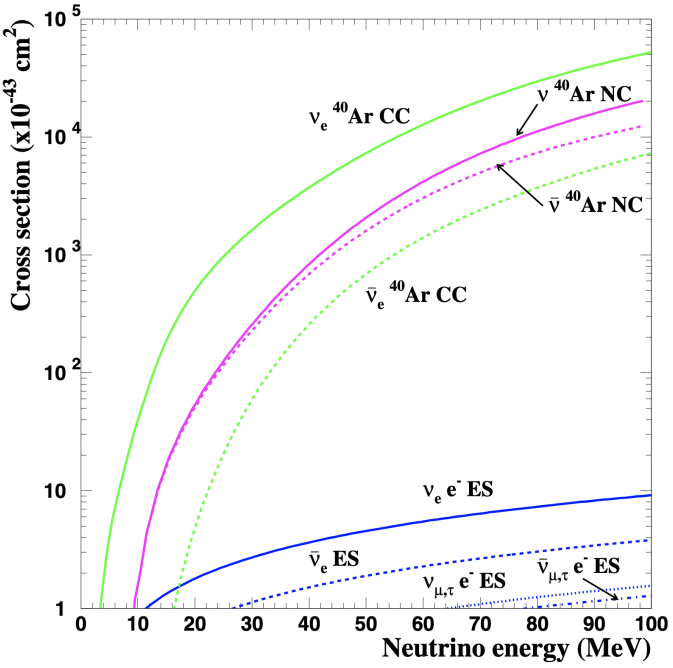

Figure 2.6: Neutrino cross sections relevant to low-energy studies in a liquid argon TPC. Taken from [5].

Figure 2.6 illustrates the cross section for the elastic processes relevant to low-energy neutrino interactions on argon. The dominant process, ν_eCC, has a Q-value of 1.50 MeV. However, this Q-value implies a transition to the ground state of ^{40}K. The spin-parity values for argon and potassium in this transition are 0^+ and 4^-, respectively. Ultimately, this transition is third forbidden and, therefore, strongly suppressed. When modelling neutrino interactions on argon, the forbidden transitions get ignored, resulting in an effective ν_eCC threshold $\sim$ 5 MeV. Under 5 MeV, the dominant interaction channel is elastic scattering on atomic electrons.

2.3.2 ^{8}B neutrinos

The lowest level process generating power in the Sun is the *pp*-reaction. Energy is released as two hydrogen atoms combine to form a deuterium atom:

$$^1\mathrm{H} + {}^1\mathrm{H} \rightarrow {}^2\mathrm{H} + e^+ + \nu_e. \tag{2.40}$$

The deuterium atom then combines with a third hydrogen atom, producing a helium isotope and one gamma,

$$^2\mathrm{H} + {}^1\mathrm{H} \rightarrow {}^3\mathrm{He} + \gamma. \tag{2.41}$$

At this point, the *pp*-chain branches. Most often, the chain chooses *pp*-I where two helium isotopes combine to form ^{4}He,

$$^3\mathrm{He} + {}^3\mathrm{He} \rightarrow {}^4\mathrm{He} + 2{}^1\mathrm{H}. \tag{2.42}$$

pp-I has a probability of occurring of 83.3% [67].

Alternatively, a ^{3}He and a ^{4}He can combine, producing a beryllium isotope and a photon,

$$^3\mathrm{He} + {}^4\mathrm{He} \rightarrow {}^7\mathrm{Be} + \gamma. \tag{2.43}$$

From this point, two more interactions may occur. *pp*-II, sometimes referred to as lithium burning, is the dominant process. A beryllium isotope absorbs an electron producing a lithium isotope and an electron neutrino,

$$^7\mathrm{Be} + e^- \rightarrow {}^7\mathrm{Li} + \nu_e. \tag{2.44}$$

The lithium isotope combines with a hydrogen atom (hence"lithium burning") and produces two helium atoms,

$$^{7}\mathrm{Li} + {}^{1}\mathrm{H} \rightarrow 2\,{}^{4}\mathrm{He}. \tag{2.45}$$

Much more rarely, *pp*-III occurs, whereby a beryllium isotope combines with a hydrogen atom, producing ^{8}B and a photon,

$$^{7}\mathrm{Be} + {}^{1}\mathrm{H} \rightarrow {}^{8}\mathrm{B} + \gamma. \tag{2.46}$$

The boron isotope then β^{+}-decays,

$$^{8}\mathrm{B} \rightarrow {}^{8}\mathrm{Be}^{*} + e^{+} + \nu_{e}, \tag{2.47}$$

and the excited beryllium isotope decays into two helium atoms. Under the β^{+}-decay, the electron neutrino is produced with a range of possible energies. As shown in Figure 2.3, the upper limit of the neutrino energy is 15 MeV. This energy range is relatively high compared to some other solar neutrino modes.

2.3.3 HEP neutrinos

Theoretically, there is a fourth possible branch to the *pp*-chain. In this case, a ^{3}He isotope combines directly with a hydrogen atom producing a helium atom, a positron and an electron neutrino,

$$^{3}\mathrm{He} + {}^{1}\mathrm{H} \rightarrow {}^{4}\mathrm{He} + e^{+} + \nu_{e}. \tag{2.48}$$

Neutrinos produced in this interaction have energies ranging up to 18.8 MeV. No experiment has successfully observed HEP neutrinos to date. Their low probability of occurring and the associated low flux make direct measurement challenging. Experiments like DUNE, with sufficiently low radiological backgrounds and well-constrained systematics, could produce the first measurement of HEP neutrinos.

2.3.4 *pep* neutrinos

In addition to the *pp*-chain, deuterium production occurs via the *pep* interaction. In this process, two protons combine with an electron, producing the hydrogen isotope deuterium. The process is as follows:

$$2\mathrm{p}^{+} + e^{-} \rightarrow {}^{2}\mathrm{H} + \nu_e \tag{2.49}$$

This interaction produces mono-energetic electron neutrinos, with an energy of approximately 1.44 MeV [68].

2.3.5 CNO neutrinos

The CNO cycle is a catalytic process of producing helium in stars. In the Sun, the CNO cycle is subdominant to the *pp*-chain; however, in stars of mass greater than 1.3 $\mathrm{M}_{\odot}$ theory predicts the CNO-cycle to be the dominant process for generating helium [69].

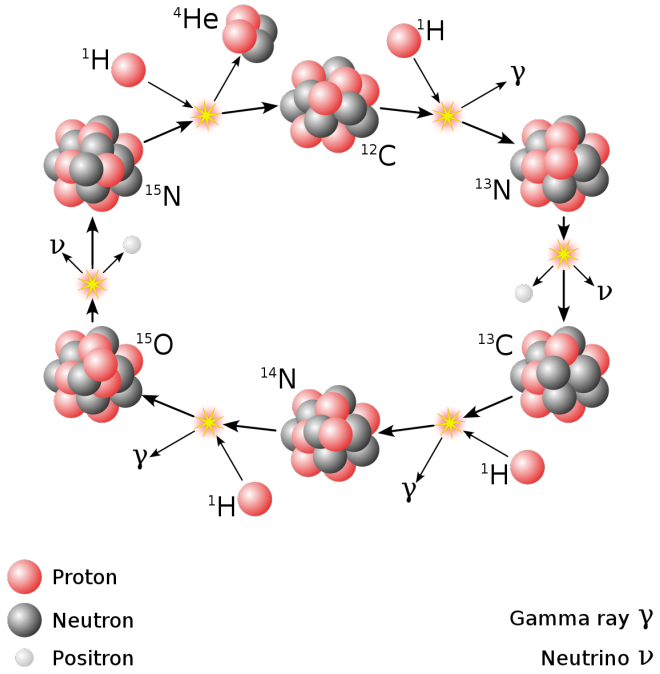

Figure 2.7: A cartoon representation of the CNO cycle.

The CNO cycle uses carbon, nitrogen and oxygen isotopes to fuse four hydrogen atoms into one helium atom. At each step of the cycle, one of the isotopes is consumed and then recovered at a later point, making the process catalytic. The overarching process of the CNO cycle is

$$4\,^1\mathrm{H} + 2e^- \rightarrow {}^4\mathrm{He} + 2e^+ + 2e^- + 2\nu_e + 3\gamma. \tag{2.50}$$

Ultimately, the electrons and positrons will annihilate, so the equation can be simplified to

$$4\,^1\mathrm{H} + 2e^- \rightarrow {}^4\mathrm{He} + 2\nu_e + 3\gamma. \tag{2.51}$$

One can extend the over-arching CNO cycle into four cold and three hot cycles. Here, cold refers to CNO cycles in active stars, and hot refers to CNO cycles in high-temperature events, such as x-ray bursts and novae.

Cold CNO-I

The first theory of a catalytic cycle that converted hydrogen to helium came over 1937-39 through the independent work of Carl Friedrich von Weizsäcker [70, 71] and Hans Bethe [42]. Initially, the CN-cycle was so-called because a stable isotope of oxygen was not in the process. In detail, the cycle is the following:

$$\begin{aligned}
^{12}\mathrm{C} + {}^{1}\mathrm{H} &\rightarrow {}^{13}\mathrm{N} + \gamma \\
^{13}\mathrm{N} &\rightarrow {}^{13}\mathrm{C} + e^{+} + \nu_e \\
^{13}\mathrm{C} + {}^{1}\mathrm{H} &\rightarrow {}^{14}\mathrm{N} + \gamma \\
^{14}\mathrm{C} + {}^{1}\mathrm{H} &\rightarrow {}^{15}\mathrm{O} + \gamma \\
^{15}\mathrm{O} &\rightarrow {}^{15}\mathrm{N} + e^{+} + \nu_e \\
^{15}\mathrm{N} + {}^{1}\mathrm{H} &\rightarrow {}^{12}\mathrm{C} + {}^{4}\mathrm{He}.
\end{aligned} \tag{2.52}$$

The two positrons emitted through proton capture annihilate, resulting in a total energy emission of 26.73 MeV [72].

CNO-I contributes to the ^{13}N and ^{15}O neutrino spectra, the two dominant neutrino fluxes detectable by neutrino experiments. The ^{13}N neutrino spectrum has an endpoint of 1.2 MeV, and ^{15}O has an endpoint of 1.73 MeV [73].

Cold CNO-II

One possibility in the CNO cycle is, in the final stage of Equation 2.52, ^{15}N captures a proton and forms ^{16}O instead of ^{12}C and a helium nucleus. In this case, the following cycle emerges:

$$\begin{aligned}
^{15}\mathrm{N} + {}^{1}\mathrm{H} &\rightarrow {}^{16}\mathrm{O} + \gamma \\
^{16}\mathrm{O} + {}^{1}\mathrm{H} &\rightarrow {}^{17}\mathrm{F} + \gamma \\
^{17}\mathrm{F} &\rightarrow {}^{17}\mathrm{O} + e^{+} + \nu_e \\
^{17}\mathrm{O} + {}^{1}\mathrm{H} &\rightarrow {}^{14}\mathrm{N} + 2{}^{4}\mathrm{He} \\
^{14}\mathrm{N} + {}^{1}\mathrm{H} &\rightarrow {}^{15}\mathrm{O} + \gamma \\
^{15}\mathrm{O} &\rightarrow {}^{15}\mathrm{N} + e^{+} + \nu_e .
\end{aligned} \tag{2.53}$$

From this subcycle, the ^{17}F neutrino spectrum appears with an endpoint similar to that of ^{15}O.

Cold CNO-III

A third possibility for the CNO cycle comes as an extension to CNO-II. Here, instead of the ^{17}O capturing a proton and producing a ^{14}N and two helium nuclei (step 4 of Equation 2.53), it forms a ^{18}F, as follows:

$$\begin{aligned}
^{17}\mathrm{O} + {}^{1}\mathrm{H} &\rightarrow {}^{18}\mathrm{F} + \gamma \\
{}^{18}\mathrm{F} &\rightarrow {}^{18}\mathrm{O} + e^{+} + \nu_e \\
{}^{18}\mathrm{O} + {}^{1}\mathrm{H} &\rightarrow {}^{15}\mathrm{N} + 2^{4}\mathrm{He} \\
{}^{15}\mathrm{N} + {}^{1}\mathrm{H} &\rightarrow {}^{16}\mathrm{O} + \gamma \\
{}^{16}\mathrm{N} + {}^{1}\mathrm{H} &\rightarrow {}^{17}\mathrm{F} + \gamma \\
{}^{17}\mathrm{F} &\rightarrow {}^{17}\mathrm{O} + e^{+} + \nu_e .
\end{aligned} \tag{2.54}$$

CNO-III is only significant for massive stars; therefore ^{18}F neutrinos are unlikely emanate from the Sun.

Cold CNO-IV

The fourth extension to the CNO cycle emerges when an ^{18}O in step three of Equation 2.54 captures a proton to form a ^{19}F instead of a ^{15}N and two alpha particles. When this happens, a further subcycle emerges, as follows:

$$\begin{aligned}
^{17}\mathrm{O} + {}^{1}\mathrm{H} &\rightarrow {}^{18}\mathrm{F} + \gamma \\
^{18}\mathrm{F} + {}^{1}\mathrm{H} &\rightarrow {}^{18}\mathrm{O} + 2\,{}^{4}\mathrm{He} \\
^{18}\mathrm{O} + {}^{1}\mathrm{H} &\rightarrow {}^{15}\mathrm{N} + \gamma \\
^{15}\mathrm{N} &\rightarrow {}^{16}\mathrm{O} + e^{+} + \nu_e \\
^{16}\mathrm{N} + {}^{1}\mathrm{H} &\rightarrow {}^{17}\mathrm{F} + \gamma \\
^{17}\mathrm{F} &\rightarrow {}^{17}\mathrm{O} + e^{+} + \nu_e .
\end{aligned} \tag{2.55}$$

Similarly to CNO-III, this process is significant only for massive stars. Therefore, ^{18}F neutrinos are unlikely to emanate from the Sun and be detected at DUNE or Hyper-Kamiokande.

CNO-IV can lead to a sodium-neon cycle. If an ^{18}F combines with an alpha particle to produce ^{22}Na [74]. As a further extension, ^{23}Na from the Ne-Na cycle can combine with an alpha particle, producing ^{27}Al, initiating the magnesium-aluminium-cycle. These extensions to CNO-IV are only prevalent in Red Giants, classical novae, and type 1A supernovae [75, 76].

2.4 Status of Neutrino Physics

Neutrino physics is one of the fastest developing fields of modern physics. The past thirty years of research have given physicists a good understanding of the three flavour oscillation model. The scope of contemporary neutrino physics covers a broad spectrum, including precision measurements of oscillation parameters and understanding the origin of neutrino masses. Additionally, the observation of solar neutrino fluxes, such as HEP and CNO neutrinos, is of interest to the physics community, and studying supernovae through their neutrino emissions (should we be fortunate enough to observe one).

2.4.1 Active and planned Experiments

Current large scale neutrino experiments are in the "accelerator experiment" category, meaning they rely on an artificial beam of neutrinos. With an accelerator experiment, one has more control over the neutrino energies and flavour. When operating over a long baseline, one can tune the experiment to maximise the effect of oscillations over a given propagation distance.

Fermilab's flagship oscillation experiment was MINOS, the Main Injector Neutrino Oscillation Search. With a near detector at Fermilab and a far detector in Northern Minnesota, MINOS examined oscillations of neutrinos from the NuMI (Neutrinos at the Main Injector) beam. NOvA, the NuMI Off-Axis ν_e Appearance experiment, is the follow-up experiment to MINOS. NOvA's near detector is also at Fermilab (in a neighbouring part of the underground laboratory complex), and the far detector is a kilo-tonne scale liquid scintillator detector in Ash River, Minnesota. The experimen-

tal design specifically targets measuring θ_{13} through ν_e appearance from a ν_μ beam. Being an above-ground experiment, NOvA has to reject the ~ 100 kHz background from cosmic ray interactions.

T2K (Tokai-to-Kamioka) is similar to NOνA, using Super-Kamiokande - a water Cherenkov detector - as the far detector for a beam generated at J-PARC, Japan. Much like NOvA, T2K also measures θ_{13} through ν_e appearance.

Both NOvA and T2K utilise an off-axis beam, yielding a more monochromatic energy spectrum. Narrowing the neutrino energy spectrum maximises any oscillation effects, ultimately leading to more accurate measurements. As active experiments, NOvA and T2K are still working on measuring mixing parameters and CP-violation. Through a joint fit, using NOvA and T2K's neutrino analyses, new measurements with higher statistical significance will come before the next phase of neutrino experiments.

The next phase of long-baseline neutrino experiments will be DUNE [77] (detailed in Chapter 3) and Hyper-Kamiokande [78], an upgrade to T2K. Hyper-Kamiokande, like its predecessor Super-Kamiokande, will be a water Cherenkov detector but with a fiducial volume 25 times larger than Super-K. DUNE and Hyper-K aim to start taking data in the late 2020s, posing significant challenges. Physically building the detectors is an engineering challenge, but storing the data from these experiments is difficult too. DUNE will produce hundreds of petabytes of information every year, all of which cannot be stored. Therefore, the information must be curated and cleaned, the uninteresting events removed, and the remaining events stored. A data engineering challenge of this magnitude rivals that of the LHC.

2.4.2 Oscillation Parameters

Modern long-baseline experiments can make precision measurements of neutrino oscillation parameters utilising their control of the neutrino spectrum and baseline. Subsection 2.4.1 describes how T2K and NOvA are suited to measure electron neutrino appearance and muon neutrino disappearance in a ν_μ beam. Observing these processes leads to precision measurements of the oscillation parameters governing this process. By extension, measuring the equivalent processes with antineutrinos allows for limits to be set on the CP-violating phase, δ_{CP}, in the three neutrino mixing framework. According to the Particle Data Group, as outlined in [79], the best values for the neutrino oscillation mixing parameters are as shown in Table 2.1.

Parameter	Current Best Values
Δm^2_{21} $[10^{-5}$ eV$^2]$	7.53 ± 0.18
Δm^2_{32} $[10^{-3}$ eV$^2]$	2.453 ± 0.034 (-2.546 ± 0.034)
$\sin\theta_{12}$	$0.307^{+0.013}_{0.012}$
$\sin\theta_{23}$	0.546 ± 0.021 (0.539 ± 0.022)
$\sin\theta_{13}$	$(2.20 \pm 0.070) \times 10^{-2}$
δ_{CP} [deg]	$1.36^{+0.20}_{-0.16}$

Table 2.1: Table showing the best values of neutrino oscillation parameters at time of writing.

Of all the mixing angles, $\sin\theta_{13}$ is decidedly smaller than the others. θ_{13} was, for a time, assumed to be zero; a value motivated by limits set from global fits to multiple data. However, in 2012 Daya Bay [80] and RENO [81], reactor neutrino experiments in China and South Korea respectively, showed that θ_{13} is non-zero. Since then, long-baseline experiments have also agreed with the reactor experiment results - namely, the measurements from NOvA [82] and T2K [83].

The worst constrained parameter currently is the CP-violating phase, δ_{CP}, making it the most sought-after measurement for current and future neutrino experiments. T2K currently favours a maximal CP-violation value [84], $\delta_{\text{CP}} = -\pi/2$, excluding the CP-conservation regions at a 90% confidence level. Current results from NOvA do not corroborate that of T2K [85], requiring a joint analysis to resolve the tension.

2.4.3 Neutrino Mass

Standard Model neutrinos are only known to exist in a left-handed chiral state. As a result, one cannot construct a Dirac mass term with Standard Model neutrinos, implying neutrinos are massless. Despite this prediction, neutrino oscillations observations show that neutrinos must have mass; otherwise, any neutrino oscillation probability, Equations 2.31 and 2.32, would be zero. Given the three-flavour model, we can attempt to observe two independent mass splittings, Δm^2_{21} and Δ^2_{32}. However, any results obtained only yield the magnitude of these values, not the sign. Not knowing the sign of the Δm^2 values leaves the neutrino mass state orders ambiguous.

To date, only one mass splitting sign is known. Solar neutrinos experience a resonance in the MSW effect, allowing for the determination of the sign of Δm^2_{21}. SNO and other solar neutrino experiments would have observed fewer oscillations had the sign of Δm^2_{21} been negative and not positive.

With this known, there remain only two possible orderings or "hierarchies", normal with m^2_3 above m^2_2 and inverted with m^2_3 below m^2_1. DUNE aims to utilise the MSW effect experienced as neutrinos propagate through the surface of the Earth to resolve the mass hierarchy. When the mass hierarchy is known, accurate mea-

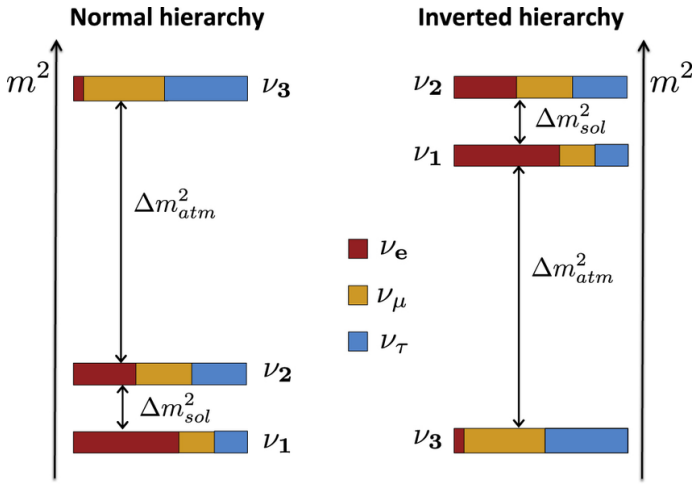

Figure 2.8: A graphical representation of the two possible neutrino mass hierarchies. The left shows the normal neutrino ordering with m_3 as the heaviest neutrino mass state, and the right shows the inverted neutrino ordering with m_3 as the lightest neutrino mass state. The figure is from [6].

surements of δ_{CP} will become possible. There exist asymmetries between neutrinos and antineutrinos that mimic CP violation. These asymmetries have hindered the acquisition of accurate measurements, making knowing the mass hierarchy critical to neutrino physics. NOνA, with its long baseline and significant matter effects, could determine the mass hierarchy before DUNE and Hyper-Kamiokande however, once operational, DUNE and Hyper-K could determine the mass hierarchy after a short period of uptime.

Future long-baseline neutrino experiments will determine the mass hierarchy but not the absolute values of the neutrino masses. To determine the neutrino masses, one can turn to β-decay for information. The mass of $\bar{\nu}_e$ changes the electron spectrum near the endpoint, allowing for precision measurements to be made. Currently, results from experiments studying the β-decay of H^3 have deduced $\bar{\nu}_e < 2.05$ eV to a 95% confidence level [86, 87]. In 2013, the Planck collaboration set a limit on the

sum of the masses of all neutrinos as $\sum m_i < 0.23$ eV to a 95% confidence level [88]. Their result comes from a cosmological analysis that observes the distribution of matter in the Universe using information such as galactic clustering. Testing a mass scale this small remains challenging but not impossible with today's experiments. KATRIN aims to measure the $\bar{\nu}_e$ mass with sub-eV precision [89].

2.4.4 Sterile Neutrinos

Theoretical motivation exists for the addition of more neutrinos to the current model. The lowest level extension is to add one more particle to the neutrino model; a sterile neutrino. Here, the term sterile refers to the fourth neutrino having no electric, colour or isospin charge, meaning it interacts purely via gravity. In addition to adding new mass splittings, one also adds three new mixing angles, θ_{14}, θ_{24}, θ_{34}, and two new CP-violating phases, δ_{14} and δ_{24}.

Chapter 3

The Deep Underground Neutrino Experiment

"We'll soon stage an attack on technology worthy of being chronicled in an anthem by Rush!"

— B. B. Rodríguez

The Deep Underground Neutrino Experiment (DUNE) is a long-baseline neutrino experiment, with construction starting in the mid-2020s. DUNE intends to study a broad physics program, including long-baseline physics, such as neutrino oscillations and mass hierarchy, nucleon decay, supernova and solar neutrino studies, and potentially further BSM physics. Starting at the Fermi National Accelerator Laboratory (Fermilab), the beam is generated and passes through the near detector. 1,300km away, in Lead, South Dakota, the neutrinos will enter the far detector at the Sanford Underground Research Facility (SURF). Figure 3.1 shows a cartoon representation of the experiment.

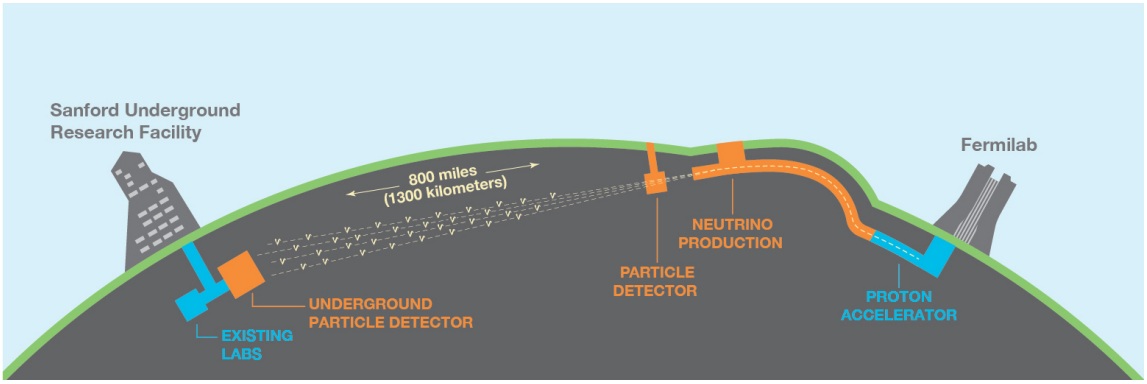

Figure 3.1: A cartoon representation of the DUNE long-baseline setup.

This chapter gives an overview of DUNE, its technology and its physics motivations. We will discuss liquid argon time projection chambers, the principal technology used at DUNE. Then, we will discuss the technologies of DUNE, including the beam, near, and far detectors. Finally, we will discuss the physics programs of DUNE.

3.1 Liquid Argon Time Projection Chamber (LArTPC)

Liquid Argon Time Projection Chamber, LArTPC, technology has undergone swaths of research and development in recent history. LArTPCs have become a staple of neutrino experiments, hailing the success of experiments such as ICARUS [90], ArgoNeuT [91], LArIAT [92] and MicroBooNE [93]. Given this, LArTPC technology has become a mainstay of neutrino physics in the United States [94].

3.1.1 History of Time Projection Chambers

The time projection chamber was first theorised by David R. Nygren in the 1970s while working at the Lawrence Berkeley Laboratory [7]. The concept was to attain the data quality of a bubble chamber but facilitate digital data readout. Altogether, producing excellent spatial and time resolution and quick data acquisition after triggering. The general concept is a drift chamber with a noble gas as a medium placed within an electric field. The electric field would cause ionisation electrons to drift towards a digital readout array. Combining the two-dimensional readout with the drift time information, one can form a three-dimensional reconstruction of an event within the detector. Additionally, the initial concept included a magnetic field that would provide particle identification capabilities. Figure 3.2 shows the initial schematic design of Nygren's TPC.

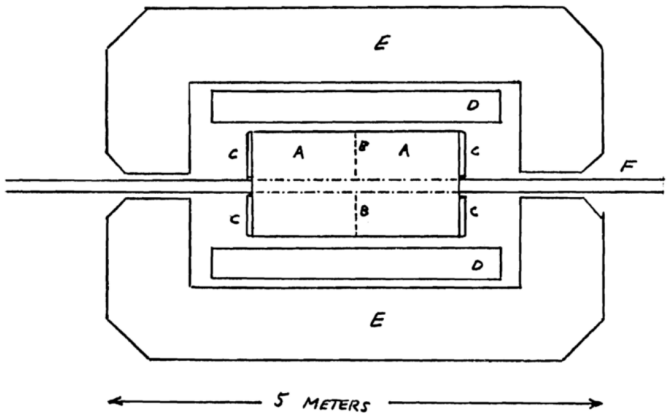

Figure 3.2: The original, hand-drawn design of the TPC by David R. Nygren [7]. (A) is a container filled with methane gas, (B) is a screen that establishes the electric field, (C) denotes the end-cap detectors, (D) is a superconducting solenoid with a magnetic field of 3.33 T, (E) is the iron yoke for the magnetic field, and (F) denotes the beam pipe.

Liquid argon TPCs and their potential as a fine-grained, high-precision detector medium for neutrino physics were proposed in 1977 by Carlo Rubbia [8]. Rubbia proposed that using a noble liquid rather than a noble gas would provide a high enough target mass, increasing the probability of neutrino interactions. Noble liquids have high electron mobility, aiding in detecting particles from ionisation. Additionally, noble liquids have low diffusion, positively impacting scintillation light detection. A high electric field is required to drift the ionisation electrons to the readout planes. As if by design, noble liquids have excellent dielectric properties, facilitating the use of such electric fields. Table 3.1 shows the properties of water and five noble liquids, demonstrating why liquid argon is a close to the ideal candidate for a TPC medium.

Liquid argon has an ionisation threshold of 23.6 ± 0.5 eV [95]. Advantageously, this furnishes liquid argon TPC technology with a low threshold for detection. With all this knowledge, Rubbia proposed that a LArTPC could be the digital replacement for

	Water	He	Ne	Ar	Kr	Xe
Abundance (atmospheric) [ppm]	5×10^4	5.2	18.2	9340.0	1.10	0.09
Boiling Point [K] at 1 atm	373	4.2	27.1	87.3	120.0	165.0
Density [g / cm^3]	1	0.125	1.2	1.4	2.4	3.0
dE/dx [MeV / cm]	1.9	0.24	1.4	2.1	3.0	3.8
Electron mobility [cm^2 / Vs]	low	low	low	400	1200	2200
Radiation length [cm]	36.1	755.2	24.0	14.0	4.9	2.8
Scintillation [γ / MeV]	-	19000	30000	40000	25000	42000
Scintillation λ [nm]	-	80	78	128	150	175

Table 3.1: Table showing the relevant properties when considering the medium for a TPC in a neutrino experiment for water and five noble liquids [22].

bubble chambers, commonly used throughout neutrino physics in the 1970s. Figure 3.3 shows the first design of a LArTPC. There is not much difference between this initial design and the LArTPCs of today.

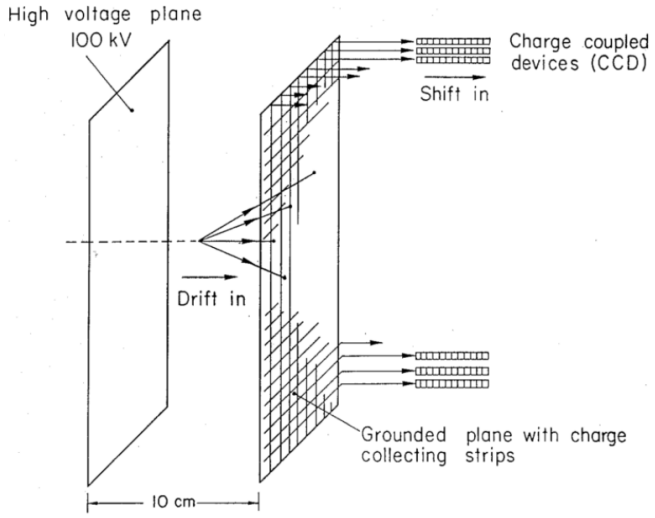

Figure 3.3: The first design of a LArTPC [8].

3.1.2 Operating modes of Liquid Argon Time Projection Chambers

A LArTPC - in its simplest form - is an anode and a cathode (or an array thereof) separated by an active drift region. A charged particle ionises the TPC medium, freeing electrons from the argon atoms. Applying an electric field across the drift region enables these electrons to drift towards the anode. The charge depositions are then read out and exported digitally by whatever data acquisition is being operated.

Initially, DUNE considered two modes of operation for the detector modules, some single-phase and some dual-phase TPC. More recently DUNE has moved away from dual-phase technology, so only a brief description will be given.

In a single-phase LArTPC, only one state (or phase) of argon gets utilised as the TPC medium. An interaction, such as a charge current neutrino interaction, causes an argon atom to release an electron. As this electron propagates through the liquid argon, it ionises the medium, resulting in a charge trail within the detector. This charge trail drifts, following the electric field between the anode and cathode planes. Once at the anode plane, the charge is collected on readout wires, converting it to a digital signal.

Dual-phase TPCs add an extra step before the charge collection. In a dual-phase TPC, there is a volume of gaseous argon above the liquid argon portion of the detector. After drifting vertically through the liquid argon, electrons drift, once more, through the gaseous phase. This procedure can be advantageous as electrons drifting

along an electric field in the gaseous argon causes electron avalanches, amplifying the signal at the readout. Furthermore, the signal amplification in dual-phase TPCs lowers the detection threshold, allowing one to observe much lower energy events.

Two types of wire planes are present on the anode plane assemblies within the TPC. The first is the induction wires, of which there are two. The wires of the induction plane lie at 35.7^o and -35.7^o to the vertical [17] and allow electrons to induce charge on the wires but not terminate on the wires. Because electrons do not terminate on the induction wires, the signals seen on the wires are bipolar. The explanation of the bipolar signal is understandable if one considers the charge on the wire as a function of time. As an electron moves toward an induction wire, it induces a charge on the wire. The induced charge manifests as a positive lobe in the charge vs time distribution. Then, as the electron moves away from the wire one gets a negative lobe of equal magnitude.

The second type of wire plane is the collection plane. On these wires, all field lines terminate, and electrons get collected without being allowed to pass by. As a result, signals on the collection wires are strictly unipolar.

Often, a grid plane gets included in the design of LArTPCs; however, it is not essential to the detector's functionality. The grid plane comes before the induction planes, shielding them from the electron charge until they are close to the induction plane. Without including the grid plane, the bipolar signal on the induction wires becomes very asymmetrical. Figure 3.4 shows this with the wire plane waveforms from simulated MicroBooNE events. Therefore, hit triggering on induction wires is

easier with the inclusion of a grid plane. It isn't clear if the benefit of including the grid plane would outweigh the cost, especially for an experiment of the scale of DUNE.

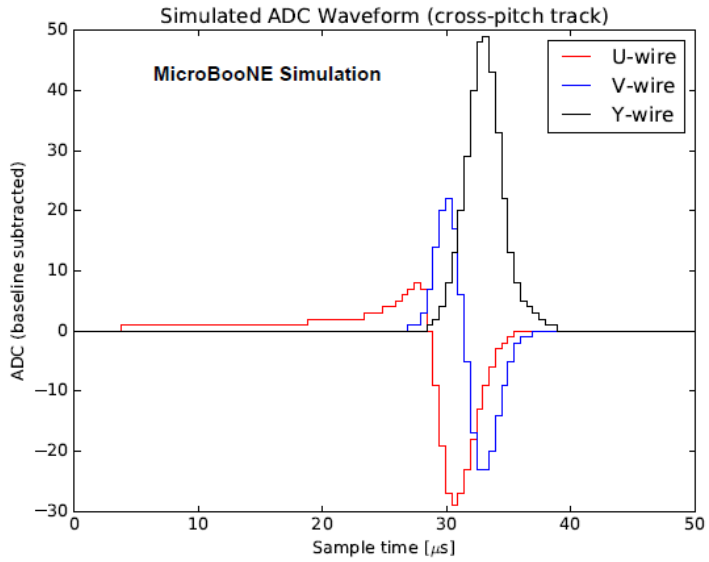

Figure 3.4: Figure displaying the waveforms of the collection (Y) and induction (U and V) planes for a simulated event in MicroBooNE, taken from [9]. Because of the absence of a grid plane, the U-wire waveform is highly asymmetrical, whereas the V-wire waveform is much more symmetrical in its positive and negative regions.

In addition to the charge deposition in a LArTPC, it is critical to account for the scintillation light produced in neutrino-argon interactions. Scintillation light is via two processes in the LArTPC. The first is argon ionisation, where an argon atom has an electron knocked out, producing an ionised argon molecule. Electron recombination results in an argon molecule in a higher energy state, which undergoes de-excitation, producing scintillation light. The second process is an argon atom is directly excited to a higher energy level which, as before, undergoes de-excitation, emitting scintillation light. Equations 3.1 and 3.2 show argon ioniation and excita-

tion respectively.

$$\mathrm{Ar}_2 \rightarrow \mathrm{Ar}_2^+ + e^- \rightarrow \mathrm{Ar}_2^* \rightarrow 2\mathrm{Ar} + \gamma, \tag{3.1}$$

$$\mathrm{Ar}_2^* \rightarrow 2\mathrm{Ar} + \gamma. \tag{3.2}$$

The charge collected on TPC planes only gives a two-dimensional representation of an event in the detector. To reconstruct a complete, three-dimensional event, one must utilise the scintillation light. Electrons in a 500 V/cm field have a drift velocity of approximately 1.633 mm/μs [96]. In the same units, light travels at roughly 3×10^5 mm/μs, so the difference between the light arriving and the charge collections allows for the calculation of the event time. Even with electrons undergoing recombination, which occurs roughly 60% of the time in the given electric field, the event time, or T0, can be used for reconstruction.

Because the scintillation light is integral to event reconstruction, the electric field applied across the anodes and cathodes must be tuned carefully. Larger electric fields minimise the electron recombination effect, simultaneously minimising the scintillation light emitted. In the same way, a smaller electric field maximises the scintillation light emission but would yield far less charge collected on the APAs. With these correlations considered, contemporary LArTPC neutrino detectors generally apply a 500 V/cm field across the anode and cathode planes. Figure 3.5 shows the recombination effect for different values of the drift field.

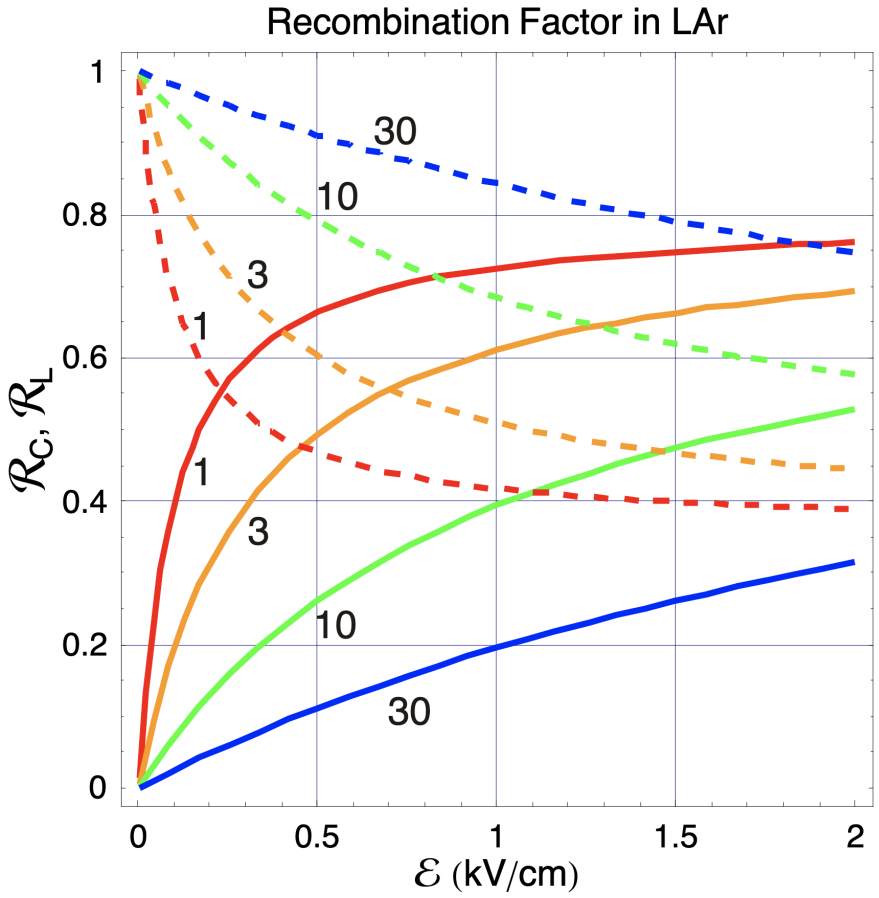

Figure 3.5: Solid lines are the recombination factor for charge (charge collected at finite field divided by charge collected at infinite field) [10, 11]. Dashed lines are the light recombination factor (light collected at field divided by light collected at zero field) [12]. The numbers labelling the curves are the specific energy loss (dE/dx) in units of MIP. Taken from [13].

3.1.3 Obstacles in LArTPC Design

As discussed, LArTPCs require a drift field of 500 V/cm to balance electron recombination and scintillation light emission. To achieve this, the voltage across the CPAs must be of the order 10^6 V. Such a high voltage presents significant challenges regarding engineering and liquid argon integrity. Designing a cryostat that can house

the high voltage system and successfully maintain temperature is difficult. More punishingly to the physics program, high voltage results in a dielectric breakdown of the liquid argon around the CPAs. A dielectric breakdown of the argon could damage the electrical components of the cryostat and compromise the detector medium. Additionally, it could pose a safety risk during the detector's operational period.

Electro-negative contaminants in the liquid argon require consideration as pure liquid argon is challenging to acquire in DUNE scale volumes. As a result, these contaminants may capture ionisation electrons, distorting the observed signal on the APAs. To quantify this, one can define an "electron lifetime", parameterising the probability of electron recombination on electro-negative contaminants. The electron lifetime, τ, is defined as

$$Q(t) = Q_0 e^{-t/\tau}, \tag{3.3}$$

where Q_0 is the initial deposited charge, and Q is the charge collected after some time, t. DUNE expects a contamination of O_2 and N_2 of approximately 100 and 20 ppm respectively [77]. Ensuring the oxygen and nitrogen levels do not rise above the accepted levels requires constant impurity removal and argon recirculation. Furthermore, recondensing any evaporated argon using a liquefier is needed to maintain the liquid argon volume.

In addition to electron recombination due to finite electron lifetimes, electrons may undergo diffusion en route to the APAs. Diffusion occurs when ionisation electrons interact within the detector medium before being collected. As with electron lifetime, understanding electron diffusion is critical to LArTPC operation.

3.2 Technology at DUNE

3.2.1 The Baseline

The baseline of 1,300 km is not an arbitrary value. $P(\nu_\mu \to \nu_e)$ through matter in a constant density approximation, to first order, is [97]:

$$\begin{aligned} P(\nu_\mu \to \nu_e) \approx & \sin^2\theta_{23}\sin^2 2\theta_{13}\frac{\sin^2(\Delta_{31}-aL)}{(\Delta_{31}-aL)^2}\Delta_{31}^2 \\ & + \sin 2\theta_{23}\sin 2\theta_{13}\sin 2\theta_{12}\frac{\sin(\Delta_{31}-aL)}{(\Delta_{31}-aL)}\Delta_{31}\frac{\sin(aL)}{(aL)}\Delta_{21}\cos(\Delta_{31}+\delta_{\mathrm{CP}}) \\ & + \cos^2\theta_{23}\sin^2 2\theta_{12}\frac{sin^2(aL)}{(aL)^2}\Delta_{21}^2, \end{aligned} \tag{3.4}$$

where $\Delta_{ab} = \Delta m^2_{ab} L/4E_\nu$, $a = G_F N_e/\sqrt{2}$, G_F is the Fermi constant, N_e is the number density of electrons in the Earth, L is the baseline in km and E_ν is the neutrino energy in GeV. If one switches from neutrinos to antineutrinos, both δ_{CP} and a switch signs. The implication of this is a neutrino-antineutrino asymmetry gets introduced by CP-violation (δ_{CP}) and the matter effect (a). Therefore, the matter effect gives DUNE sensitivity to the sign of Δ_{31}, specifying the neutrino mass ordering.

The matter effect asymmetry is due to the presence of electrons and, in parallel, the absence of positrons in the Earth's crust. In the 0.1-10 GeV range, the matter asymmetry effect increases with the experiment's baseline (because the neutrinos travel through more matter). Therefore, the longer the baseline, the more sensitive one is to the neutrino mass ordering. For baselines longer than 1,200 km, the degeneracy between the asymmetries from matter and CP-violation effects can be resolved [98].

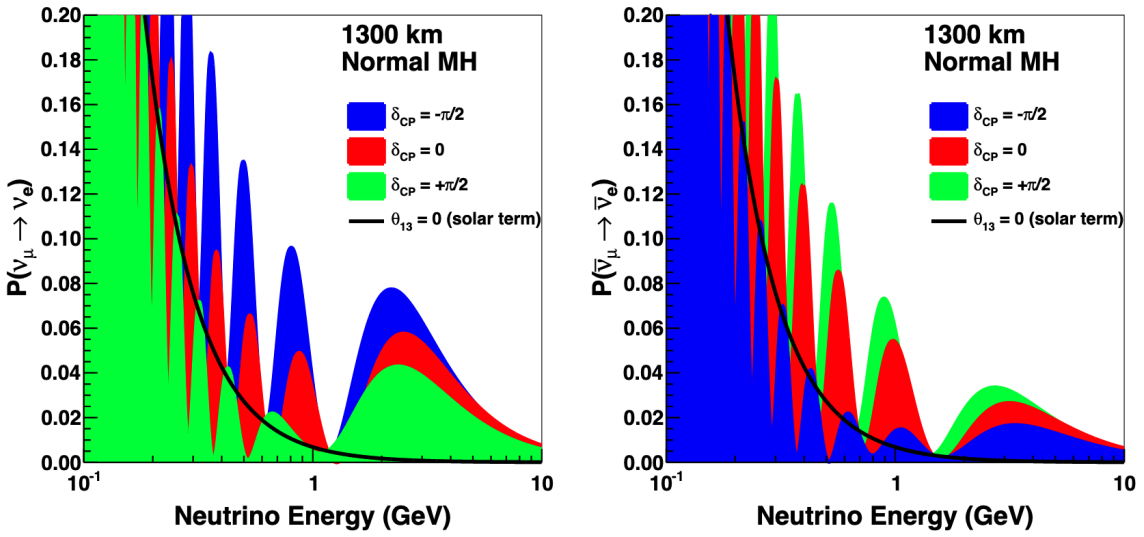

Figure 3.6: The appearance probability at a baseline of 1300 km, as a function of neutrino energy, for $\delta_{\text{CP}} = -\pi/2$ (blue), 0 (red) and $\pi/2$ (green), for neutrinos (left) and antineutrinos (right), for normal ordering. The black line indicates the oscillation probability if θ_{13} were equal to zero [14].

DUNE is on-axis, unlike running experiments, such as NOvA, and future experiments, like Hyper-K, which are off-axis. Off-axis setups allow for a narrow band of neutrino energies, whereas on-axis produces more of a spectrum of neutrino energies. A spectrum can be highly beneficial, though. Plotting the electron neutrino appearance, $P(\nu_\mu \rightarrow \nu_e)$, at a baseline of 1,300 km as a function of neutrino energy for varying δ_{CP}, Figure 3.6, yields some interesting observables. Notably, the value of δ_{CP} affects the oscillation phase and amplitude. Furthermore, the difference in probability amplitude for different values of δ_{CP} is more at higher oscillation nodes and generally lies below the 1.5 GeV. Therefore, having a broad range of neutrino energies allows the mapping out observed oscillations, not just counting the rate of ν_e appearance.

3.2.2 The Neutrino Beam

DUNE's neutrino beam has a broad energy band which, at a baseline of approximately 1,300 km, facilitates access to the first two oscillation maxima. At this baseline, these oscillation maxima occur at 0.8 and 2.4 GeV.

DUNE's beam starts as a proton beam of energies between 60-120 GeV. Protons get extracted from the Fermilab Main Injector, directed up through an artificial knoll, and then down to establish the beam's ultimate trajectory in the direction of the near detector. Once on their proper trajectory, the protons strike a target, producing secondary mesons. The secondary mesons get focused using large magnetic horns before they decay into muons and neutrinos. At this stage, one can specify a neutrino or antineutrino-dominated beam by choosing the polarity of the magnetic focusing horns. This choice furnishes DUNE with multiple neutrino channels to study with only one beam. The general mesonic decays producing neutrinos are listed below.

Forward Horn Current		Reverse Horn Current	
Decay Mode	Branching Ratio	Decay Mode	Branching Ratio
$\pi^+ \to \mu^+ + \nu_\mu$	0.9999	$\pi^- \to \mu^- + \bar{\nu}_\mu$	0.9999
$K^+ \to \mu^+ + \nu_\mu$	0.6355	$K^- \to \mu^- + \bar{\nu}_\mu$	0.6355

Post decay, any muons or other hadronic remnants are stopped, yielding a neutrino (or antineutrino) beam, tuned to have energy between 0.5 - 5 GeV. Figure 3.7 depicts an overview of the neutrino beam.

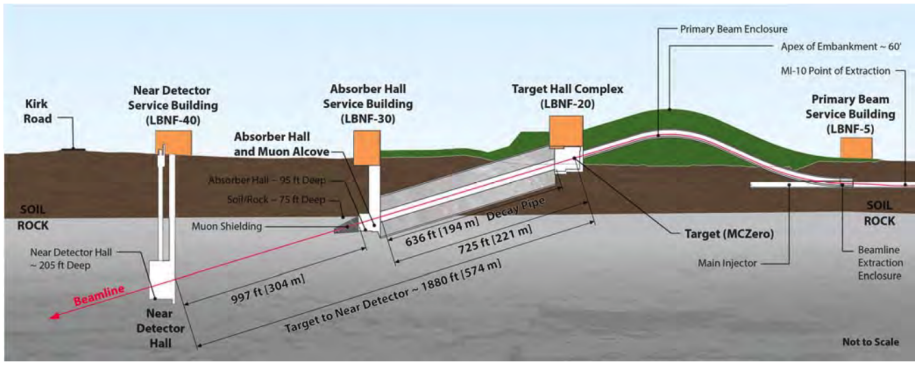

Figure 3.7: LBNF overall project schematic longitudinal section view [15].

For the most part, the dominant neutrino flavour in the beam is the desired one. However, one cannot avoid other neutrinos appearing in the beam. In the Reverse Horn Current mode, RHC, muons can decay before being absorbed,

$$\mu^- \rightarrow \nu_\mu + e^- + \bar{\nu}_e.$$

Muon decay produces a flux of ν_e which needs consideration in electron neutrino appearance studies at DUNE. Additionally, pions of either charge sub-dominantly decay into electrons, and electron neutrinos [99]; however, the branching ratio is almost negligibly small. Lastly, kaon decays also produce an electron neutrino flux through the following processes:

$$K_L^0 \rightarrow \pi^- + e^+ + \nu_e, \tag{3.5}$$

$$K^+ \rightarrow \pi^0 + e^+ + \nu_e. \tag{3.6}$$

Figure 3.8 shows the beam composition for the neutrino and antineutrino modes.

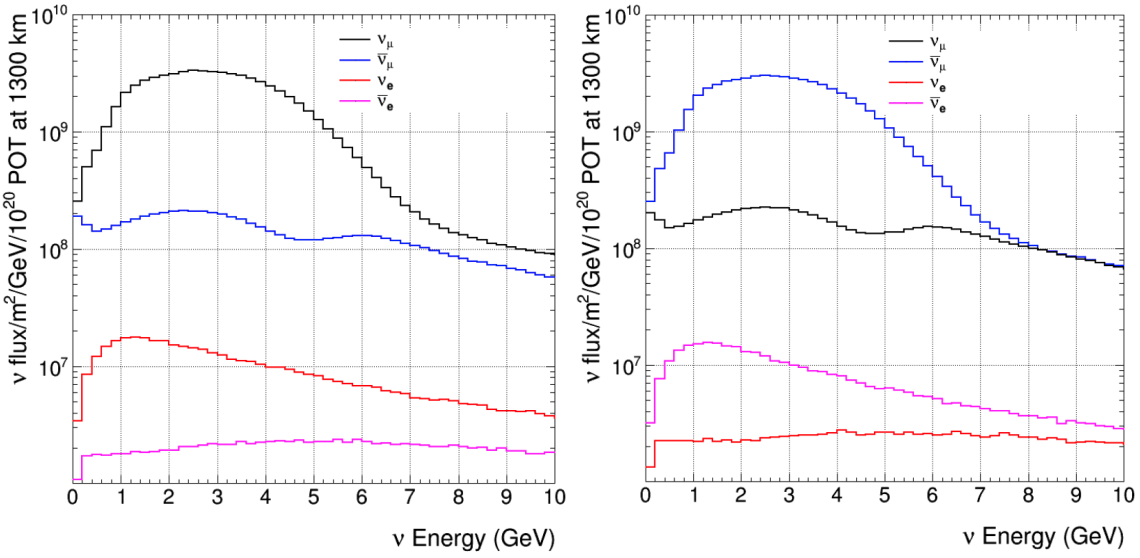

(a) Neutrino mode

(b) Antineutrino mode

Figure 3.8: Neutrino fluxes at the far detector as a function of energy in the absence of oscillations with horns focusing positive, 3.8a, and negative, 3.8b, particles. In addition to the dominant ν_μ ($\bar{\nu}_\mu$) flux, the minor components are also shown [15].

3.2.3 The Near Detector

The primary requirement of a near detector (ND) is to identify neutrino interactions and distinguish between the four prevalent neutrino flavours in the beam. In its current conceptual form, the near detector for DUNE is composed of multiple sub-detectors, all stacked together. This subsection will briefly describe each component moving down the beamline.

ND-LAr ArgonCube structure

Composed of 35 individual LArTPC modules, ND-LAr is a conventional time projection chamber for detecting neutrino interactions [16]. In addition to a wire-based readout, ND-LAr TPC modules include a light collection system and a pixel-based charge readout.

At ND distances, oscillations are negligible, allowing direct examination of the beam composition. Neutrino interactions in ND-LAr produce energetic leptons, predominantly GeV scale muons, and hadronic recoil events. ND-LAr struggles with muon containment at these energies, demanding a magnetic spectrometer downstream as muon direction and charge are critical to neutrino energy reconstruction.

Magnetized Argon Target System: ND-GAr

The following near detector module is a magnetised high-pressure gaseous argon time projection chamber surrounded by an electromagnetic calorimeter (ECAL). The HPgTPC and the ECAL are in a 0.5T magnetic field and a muon detector system.

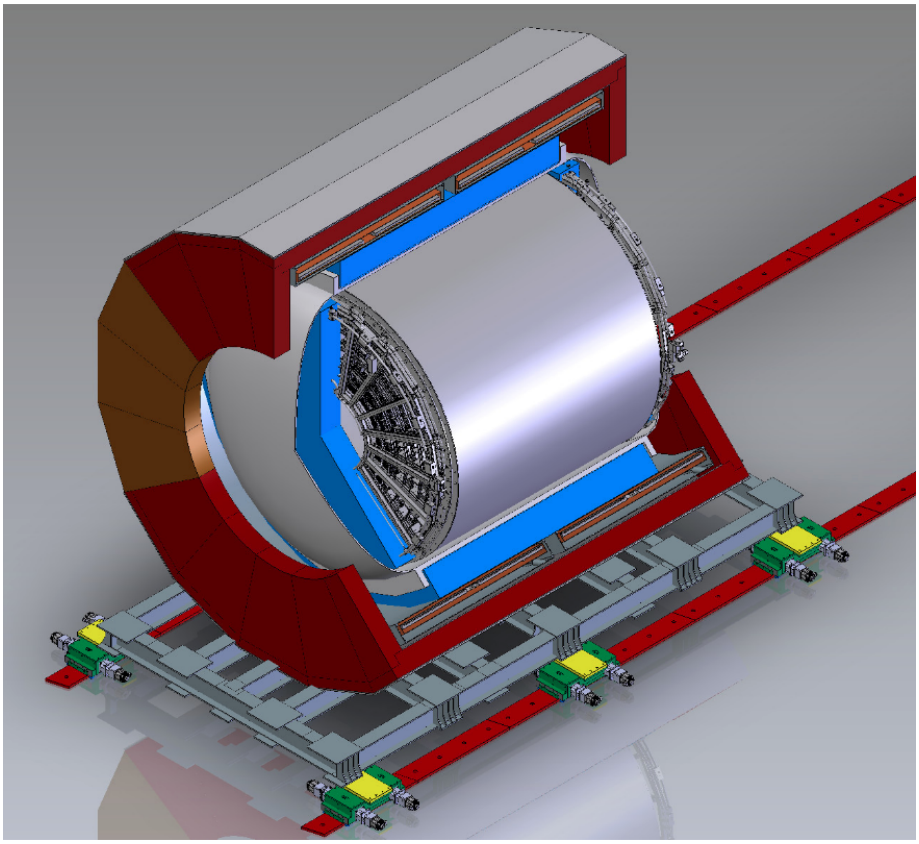

Figure 3.9: Schematic of ND-GAr showing the HPgTPC, its pressure vessel, the ECAL, the magnet, and the return iron. The detectors for the muon-tagging system are not shown [16].

ND-GAr extends the capabilities of the near detector by measuring the sign of charged particles exiting ND-LAr. Furthermore, HPgTPCs have better measurement capabilities at lower energies when compared to the LArTPCs at the near and far detectors. An avalanche effect near the anode wires provides signal amplification proportional to the ionization strength. ND-GAr extends DUNE's particle identification (PID) performance, which helps to constrain beamline systematics.

System for on-Axis Neutrino Detection - SAND

The SAND module reuses the calorimeter and magnet from the KLOE experiment [100]. KLOE aimed to study CP-violation in neutral kaon decays, running for almost 20 years, from 1999 to 2018. Throughout its runtime, KLOE showed stable detector performance. For SAND, the KLOE detector gets instrumented with a tracking system in its drift chamber. Preliminary studies with SAND have concerned the reconstruction of ν_μ CC interactions. Reconstruction information mainly comes from neutrons, photons and neutral pions, reconstructed predominantly with ECAL information. SAND has shown an energy resolution at the core of the energy distribution of better than 7%.

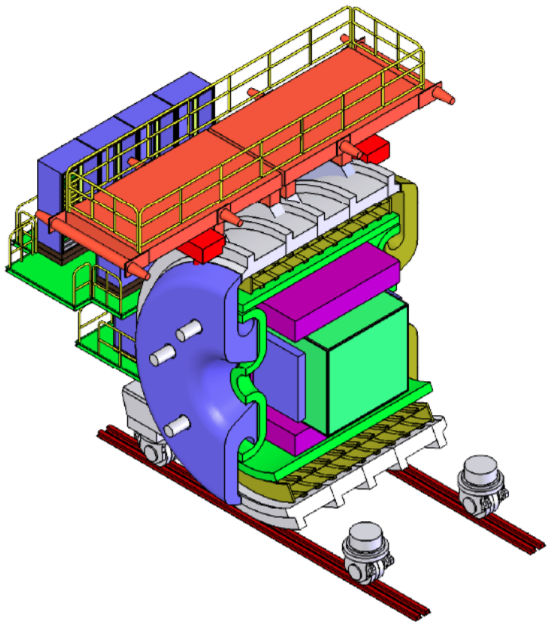

Figure 3.10: Drawing of the SAND system showing 3D scintillator tracker (3DST) and TPCs configuration with 3DST in the centre (light green), low-density tracker (TPC or STT, Magenta), ECAL (green), the magnet coil (gold), and the return yoke (gray) [16].

DUNE-PRISM

The peak energy of a neutrino beam decreases as the observation angle relative to the beam direction increases. Mathematically, the neutrino energy due to pion decay as a function of beam angle follows [101]

$$E_\nu = E_\pi \left(1 - \frac{m_\mu^2}{m_\pi^2}\right) \frac{1}{1 + \theta^2 \gamma^2}, \tag{3.7}$$

where E_π, m_π and γ are the energy, rest mass and Lorentz factor of the parent pion, respectively. In addition, m_μ is the rest mass of the muon, and θ is the angle between the pion and neutrino directions. Figure 3.11 shows the neutrino energy distributions for various angles off the beam axis.

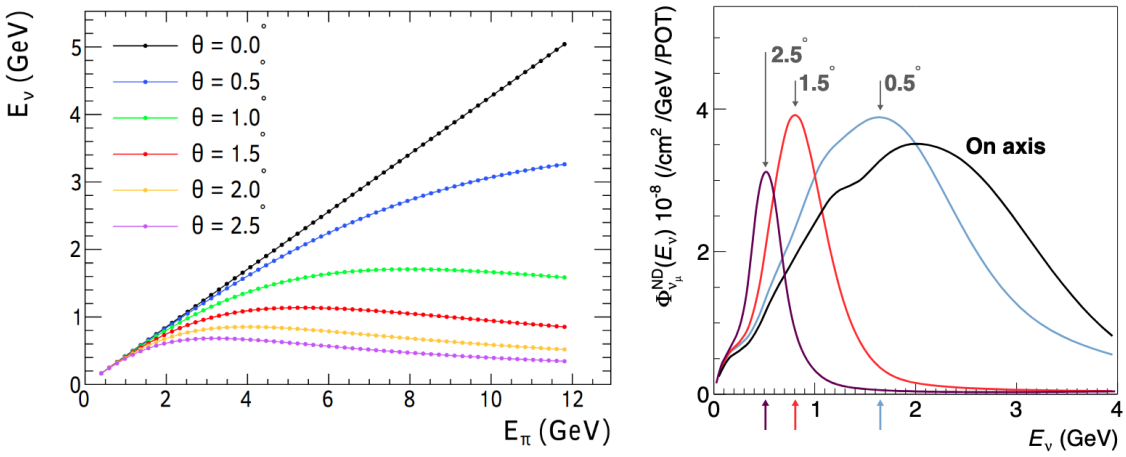

Figure 3.11: Left: the observed neutrino energy in the lab frame from a decay-in-flight pion as a function of pion energy and observation angle away from the pion momentum direction. Right: the predicted DUNE beam muon neutrino flux ad the ND site as a function of off-axis angle. The arrows indicate the peak neutrino energy for three different off-axis angles [16].

Off-axis experiments, such as T2K ($\theta = 44$ mrad) and NOvA ($\theta = 14$ mrad), utilise narrow-band neutrino beams to specify their searches. The DUNE-PRISM (DUNE Precision Reaction-Independent Spectrum Measurement) is a sliding gantry that moves the entire near detector. With this, the near detector can probe various off-axis positions relative to the beam. The collection of measurements adds a degree of freedom for constraining systematic uncertainties for neutrino interaction modelling.

3.2.4 Single Phase Far Detector Module

Numerous potential designs for far detector LArTPCs are under discussion. DUNE has moved away from a combination of single and dual-phase modules. The first two FD modules will be single-phase. However, DUNE has now incorporated horizontal and vertical drift single-phase detectors. The first module to be installed will be a horizontal drift detector, with the following modules using either design. In addition to the single-phase detectors, DUNE opened up the possibility of a "Module of Opportunity", whose design can probe other physics without impacting DUNE's main physics goals.

The baseline DUNE FD modules, the horizontal and vertical drift modules, will have total, active, and fiducial liquid argon masses of 17.1, 13.3 and 10.0 ktonne, respectively. We will not be discussing the vertical drift detector here, as it is still in its infancy, with significant research occurring at the time of writing. The module-of-opportunity discussed in this thesis is the low-background module-of-opportunity, whose masses differ slightly from the baseline modules.

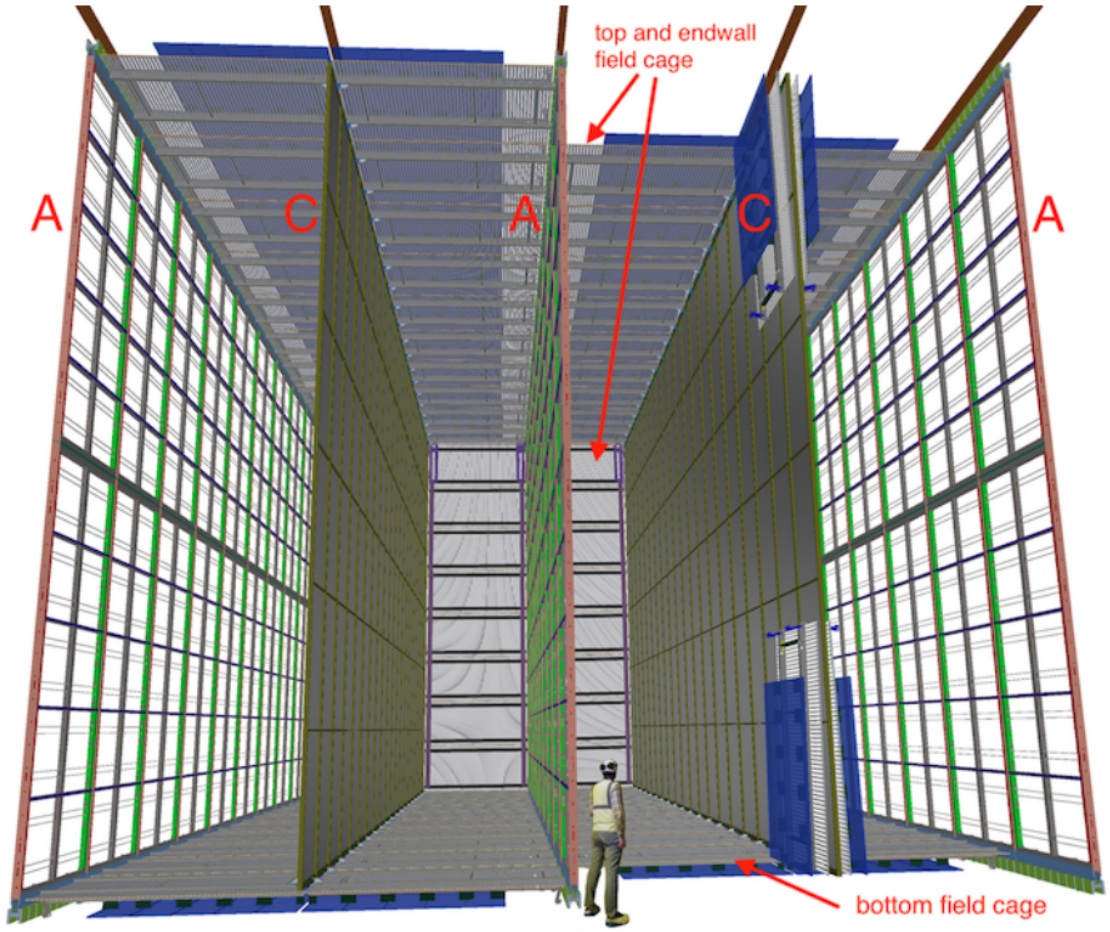

Figure 3.12: A 10 ktonne DUNE far detector single phase module, show the alternating 58.2 m long (into the page), 12.0 m high anode (A) and cathode (C) planes, as well as the field cage that surrounds the drift regions between the anode and the cathode planes. On the right-hand cathode plane, the foremost portion of the field cage is show in its folded state [17].

Figure 3.12 shows a schematic of the single-phase horizontal drift FD. The interior contains several hundred detector units: the Anode and Cathode Plane Assemblies, APAs and CPAs. Each plane measures 2.3 m wide and 6 m tall, leading to a configuration of two high and twenty-five deep walls of APAs and CPAs within the

$12 \times 14.5 \times 58$ m active volume. To facilitate the required 500 V/m field in the drift volume, the CPAs carry a -180 kV voltage. Surrounding the APA-CPA array is an aluminium field cage, terminating any extruding field lines.

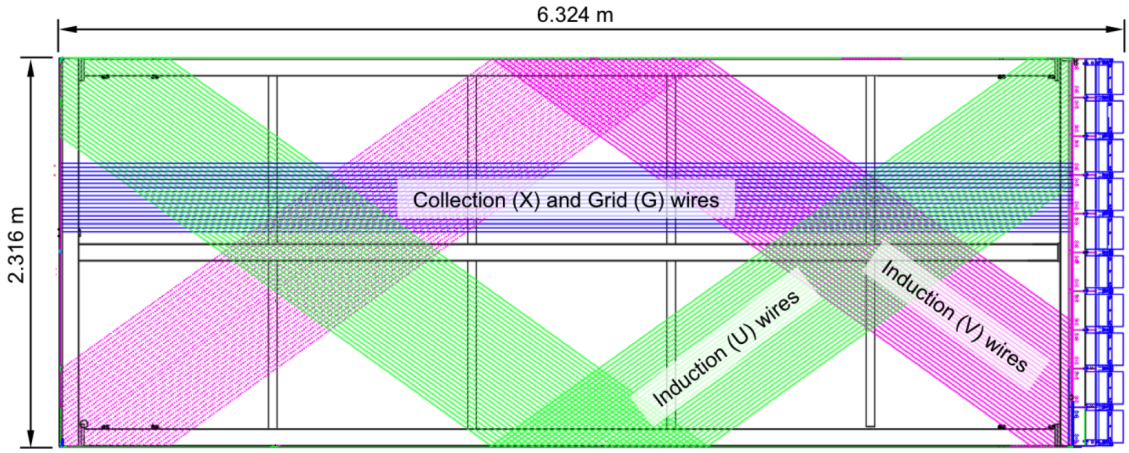

Figure 3.13: Illustration of the DUNE APA wire wrapping scheme showing small portions of the wires from the three signal planes (U, V, X). The fourth wire plane (G) above these three, and parallel to the X, is present to improve the pulse shape on the U plane signals. The TPC electrinic boxes, shown in blue on the right, mount directly to the frame and process signals from both the collection and induction channels. The APA is shown turned on its side in a horizontal orientation [17].

Figure 3.13 illustrates the wire wrapping configuration of the APAs at DUNE. Each APA has four planes, the collection plane (X or Z), two induction planes, V and U, and the grid plane, G. The APAs get stacked on top of each other, facilitating charge readout over various drift regions. As a result, the wire wrapping is critical to APA design, and the angle must remain fixed across different APAs. Interestingly, the number of readout channels required gets reduced because of the wire wrapping. For example, a V plane wire segment on one side of an APA becomes a U plane wire segment on the opposite side. This repurposing could lead to potential ambiguity regarding which drift region a charge deposition originated. The 35-ton prototype

experiment set the wire planes at different angles, reducing the number of induction wire intersections on collection wires. While this works, the solution adopted by DUNE is to set the induction wires at an angle such that an induction wire intersects exactly one collection wire. An angle of $\pm 35.7°$ allows for such a configuration.

The front-end electronics get mounted to the APAs, shown in blue in Figure 3.12. These electronic components are required to function within the cryostat and are, therefore, referred to as the "cold-electronics". The cold-electronics are responsible for two aspects of data acquisition. The first is signal shaping and amplification, and the second is digitizing the analogue signals from the wires.

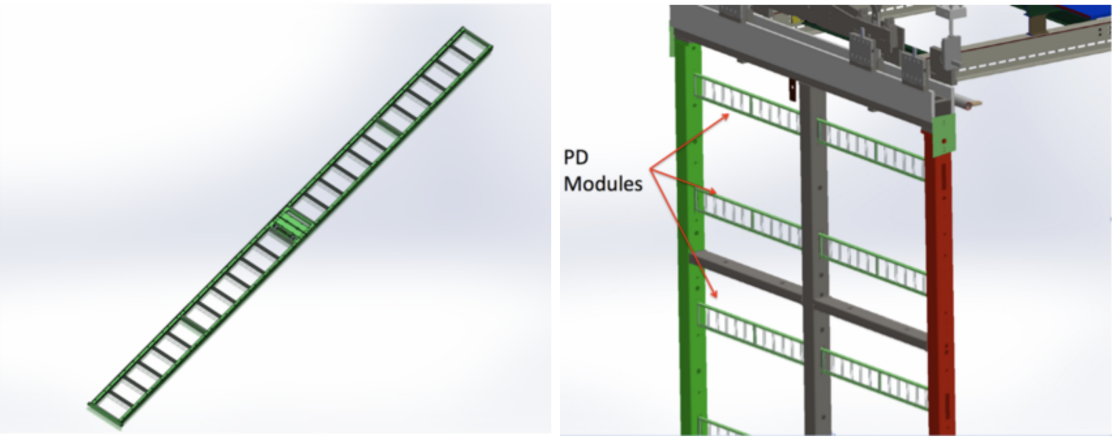

Figure 3.14: Left: an X-ARAPUCA PD module. The 48 SiPMs that detect the light from the 24 cells are along the long edges of the module. Right: X-ARAPUCA PD modules mounted inside an APA [17].

As previously discussed, event reconstruction in LArTPC detectors requires optical information. The specifications (at the time of writing) of the Photon Detector System, PDS, are ten $209 \times 12 \times 2$ cm bars mounted to the APA frames behind the

collection plane. These two meter-long bars contain 24 X-Arapuca[1] cells grouped into four supercells of six cells. Figure 3.14 shows the frames on which the X-Arapuca cells, shown in Figure 3.15, get mounted.

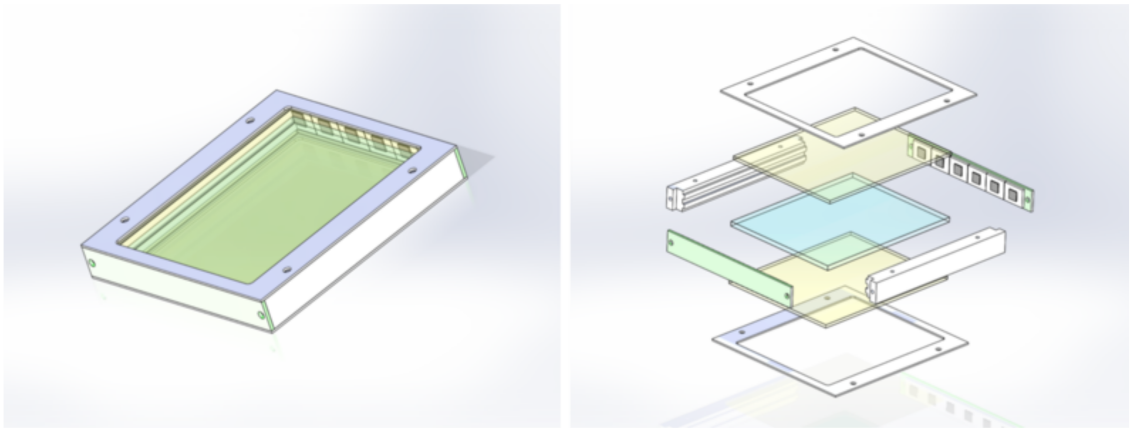

Figure 3.15: Left: an X-Arapuca cell. Right: an exploded view of the X-Arapuca cell, where the blue sheet is the wavelength-shifting plate and the yellow sheets the dichroic filters [17].

An X-Arapuca cell consists of, in its simplest form, two dichroic filters sandwiching a wavelength-shifting (WLS) plate, spanning the length of a supercell which converts UV photons into 430 nm photons in the visible spectrum. Visible photons emitted within the WLS plates, provided their angle to the surface is greater than the critical angle, get collected in silicon photomultipliers, SiPMs, at the edge of the plates. Any photons that escape the plates get reflected off the dichroic filters back into the WLS plates, as their optical cutoff reflects photons with wavelengths exceeding 400 nm.

[1]The name "Arapuca" is a homage to the South American bird trap of the same name. The way an X-Arapuca traps light is analogous to the bird trap's functionality.

3.2.5 Low Background Far Detector Module

The low-background far detector is, in essence, a single-phase far detector module that is highly optimised to reduce radiological backgrounds and impurities. Figure 3.16 shows one configuration of a potential DUNE-like low-background module of opportunity.

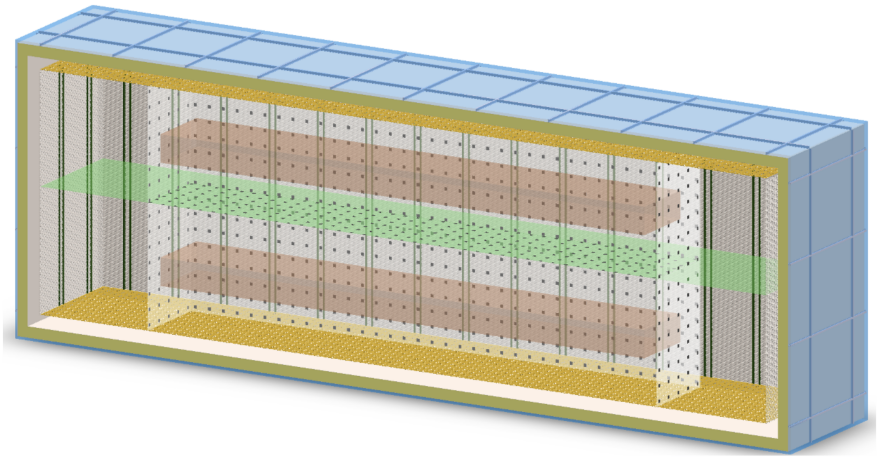

Figure 3.16: Shown is the base design for the proposed low background detector. Blue shows external water "brick". The top and bottom yellow planes are the Charge Readout Panels unchanged from the Vertical Detector design. The central cathode is in green. The white box of acrylic (full interior volume) is of dimensions 6x12x20 (12x12x60) m^3. The black points are SiPM modules shown here at a low coverage of 10% for viewing's sake, while some studies in this paper use up to 80% coverage. A proposed fiducial volume totalling 2-ktonne is shown in the two beige boxes [18].

Hydrogen-rich materials are highly effective at shielding neutrons. With this knowledge, the low-background cryostat gets lined with "bricks" of water. Functionally, these water bricks would get nestled within the I-beam support structure around the cryostat. As suggested in [102] and [19], water shielding around a DUNE-like

cryostat could, and a thickness of 40 cm, reduce the neutron capture rate by approximately there orders of magnitude. Figure 3.17 illustrates the neutron capture rate as a function of water shielding thickness.

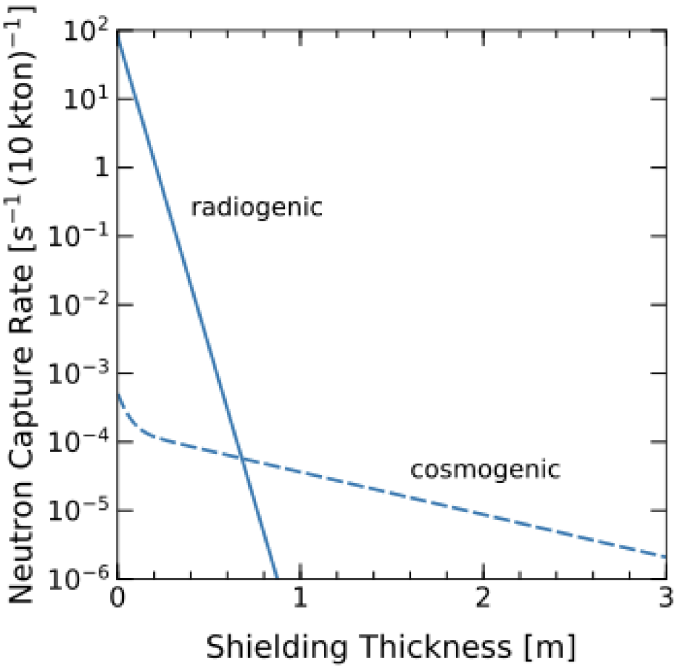

Figure 3.17: Radiological and cosmogenic neutron capture rate as a function of water shielding thickness [19].

A three order of magnitude reduction of external neutrons means internal neutron generators become the leading contributors. The I-beam support structure comprises a total of 1-ktonne of stainless steel, an active neutron generator due to its aluminium content. The low-background module aims to echo the external reduction inside the detector through three techniques. The first is an informed selection of construction materials that are as radiologically neutral as possible. The second is additional internal neutron shielding. The module-of-opportunity proposes doping a higher

density polyurethane foam with boron, lithium or gadolinium to improve its neutron mitigating capabilities. Lastly, software developed to remove neutron events is to be implemented, rejecting neutron captures from the data.

Target radon levels in the low-background module are 2 μBq/kg. DUNE expects radon levels of 1 mBq/kg [103], roughly three orders of magnitude greater than the low-background module target. DarkSide-50 [104] has achieved radon at this level, and DEAP-3600 [105] has exceeded this with radon levels of 0.2 μBq/kg. Radon reduction techniques include

- Radon removal during purification via an inline radon trap,
- emanation measurements and materials campaign,
- surface treatments,
- dust control,
- radon reduction system during instillation and operation,
- drifting of charged daughters to the cathode,
- alpha tagging through pulse shape discrimination.

The low-background module proposes using underground argon (UAr) as the detector medium. Natural argon is, predominantly, ^{40}Ar, with some contaminant isotopes, including ^{39}Ar ($T_{1/2}$ = 269yr, Q_β = 565 keV), ^{37}Ar ($T_{1/2}$ = 35d, Q_β = 813 keV), ^{42}Ar ($T_{1/2}$ = 32.9yr, Q_β = 599 keV). Atmospheric argon (AAr) has its limitations in large-scale LArTPC detectors due to the high ^{39}Ar activity (approximately 1Bq per kg of argon [106]).

DarkSide-50 is the only experiment to use UAr as the detector medium and measured a ^{39}Ar activity of 0.73 mBq/kg [107], 1,400 times lower than that of AAr. In addition to the significantly lower ^{39}Ar activity, UAr will be notably depleted of ^{42}Ar as it gets formed primarily in the upper atmosphere in cosmic ray interactions.

^{85}Kr, a β-emitter, is a significant radiological background in detectors using AAr as the detector medium. Generally, ^{85}Kr gets produced via neutron capture on ^{84}Kr, nuclear fission of uranium and plutonium, and in human-induced fissions in nuclear reactors [108]. UAr data from DarkSide-50 yielded a ^{85}Kr activity of 2 mBq/kg [107], several orders of magnitude below that of AAr. Naturally, the concentration of ^{85}Kr will vary depending on where the argon gets extracted.

3.3 The DUNE Physics Program

The DUNE science program has several primary and some ancillary aims. First and foremost, DUNE, as a long-baseline neutrino experiment, aims to evaluate the neutrino oscillation parameters, such as mixing angles, mass splittings and the value of δ_{CP}. In conjunction, DUNE aims to evaluate the neutrino mass ordering. Additional goals include probing the physics of supernovae, examination of baryon number violation, observation of solar neutrino fluxes and other Beyond-Standard-Model physics, BSM.

3.3.1 CP-violation and Mass Hierarchy

The Pontecorvo-Maki-Nakagawa-Sakata matrix describing the mixing between neutrino mass and flavour eigenstates is:

$$\begin{pmatrix} \nu_e \\ \nu_\mu \\ \nu_\tau \end{pmatrix} = \begin{pmatrix} U_{e1} & U_{e2} & U_{e3} \\ U_{\mu 1} & U_{\mu 2} & U_{\mu 3} \\ U_{\tau 1} & U_{\tau 2} & U_{\tau 3} \end{pmatrix} \begin{pmatrix} \nu_1 \\ \nu_2 \\ \nu_3 \end{pmatrix}. \tag{3.8}$$

Like the CKM-matrix, the PMNS-matrix gets characterised by three mixing angles and one complex phase. By convention [109], the mixing angles and complex phase get defined as:

$$\sin^2\theta_{12} = \frac{|U_{e2}|^2}{1-|U_{e3}|^2}, \tag{3.9}$$

$$\sin^2\theta_{23} = \frac{|U_{\mu 3}|^2}{1-|U_{e3}|^2}, \tag{3.10}$$

$$\sin^2\theta_{13} = |U_{e3}|^2 \tag{3.11}$$

$$\delta_{\mathrm{CP}} = -\arg(U_{e3}). \tag{3.12}$$

Assuming the CP-violating phase follows $\delta_{\mathrm{CP}} \neq 0,\ \pi$ and all values of $U_{\alpha i}$ are nonvanishing, then the PMNS matrix is complex and CP-invariance is violated. Ultimately, CP-violating implies oscillation probabilities for neutrinos are not the same for antineutrinos.

DUNE aims to evaluate the neutrino mass ordering. With the detector volume, beam intensity and sensitivity, DUNE will discover the mass ordering at a 5σ or greater significance within the first few years. Furthermore, this is possible without knowing the value of δ_{CP}. This agnosticism toward δ_{CP} is due to significant matter effects in a 1300 km baseline neutrino experiment.

In the case of maximal CP-violation, DUNE will measure δ_{CP} at a 5σ confidence level within 14 years of running under the current operation plan. Fortunately, results from T2K imply near-maximal CP-violation [84]. When the beam gets upgraded to a multi-megawatt power beam, the precision on the δ_{CP} will approach 5%; comparable to that of the analogous measurement in quark mixing described by the CKM-matrix.

3.3.2 Oscillation Parameters

Precision measurements of the mixing parameters will get evaluated at DUNE. The value of θ_{23}, important when evaluating the muon disappearance and electron appearance probabilities, will be measured to a precision equal to or better than 1°. DUNE will also match the world-leading measurement of θ_{13} from reactor neutrino experiments with a long enough exposure. This analysis utilises electron and anti-electron neutrino appearance, Equation 2.31. In addition, the resolution of Δm^2_{31} will get significantly tightened.

3.3.3 Baryon number violation

The question *"Are protons stable?"* is profoundly upsetting, as its simplicity mocks the potential answer's implications. Observations show protons to be stable and not decay into any lighter particles. However, no known symmetry of nature requires them to be stable. DUNE will search for proton decay through the $p \rightarrow K^{+}\bar{\nu}$ channel [110]. Assuming no observations of proton decay occur in a 400 ktonne-year exposure, DUNE would limit the proton lifetime to approximately $1.3{\times}10^{34}$ years. The current best limit (at the time of writing) is $5.9{\times}10^{34}$ years, set by Super-Kameokande [111]. Interestingly, were the proton lifetime equal to the limit set by Super-K, DUNE would observe five candidate events in ten years of being fully operational.

3.3.4 Supernova and Solar neutrinos

The most famous supernova in particle physics, Supernova 1987A, instantiated a new era of extragalactic neutrino astronomy [112, 113]. SN1987A released a burst of neutrinos which travelled 50 kiloparsecs from the Large Magellanic Cloud (LMC) to Earth. In total, 25 antineutrinos got detected between Kamiokande-II, IMB and Baksan.

DUNE is uniquely sensitive to ν_e interactions via

$$\nu_e + {}^{40}\mathrm{Ar} \rightarrow e^{-} + {}^{40}\mathrm{K}^{*}, \tag{3.13}$$

a channel inaccessible to liquid scintillator and water Cherenkov detectors whose sensitivity is mainly towards $\bar{\nu}_e$ through inverse beta decay. Should a supernova occur in DUNE's lifetime, DUNE will be able to make world-leading observations of supernova features. These features are the flavour, energy spectrum and time structure of the event lasting only a few tens of seconds, with neutrinos of energies of the order 10 MeV [114, 115]. The neutrinos from a supernova burst (SNB) carry intrinsic information about the progenitor star, the collapse, the explosion, and the result of the supernova - whether a neutron star or black hole forms. Detection of such low-energy neutrinos presents its challenges, not least of which is the slim likelihood of observing the ν_x[2] flux. The SNB neutrino energies are below the charge current threshold for ν_x interactions, and so only neutral-current ν_x interactions would occur.

Despite the limitations, low-energy neutrino interaction theory and measurement have evolved significantly since 1987. Great leaps in SNB modelling have yielded full 3D simulations of core-collapse supernovae. Furthermore, neutrino detector technology has come a long way. DUNE will detect several thousand supernova neutrinos in the event of a supernova within 100 kpc of Earth.

DUNE's sensitivity to ν_e and capabilities in the tens of MeV range make it a prime candidate as a solar neutrino observatory. The processes generating helium in the Sun release a steady flux of neutrinos, dubbed solar neutrinos. The ^{8}B neutrinos, which have relatively high flux and energy on the solar neutrino scale, helped resolve the solar neutrino problem. Other channels, such as the *hep* neutrinos, whose energies are comparatively high but have significantly lower flux, have yet to be observed. DUNE is in a competitive position to make the first measurement of the *hep* neutrino

[2]Here, ν_x refers to the combined flux of ν_μ, $\bar{\nu}_\mu$, ν_τ, and $\bar{\nu}_\tau$.

flux. In addition, DUNE has the potential to measure the CNO neutrino flux, a subdominant helium production mechanism in the Sun. Furthermore, measuring the CNO flux would also lead to assessing the Sun's metallicity.

3.3.5 Beyond Standard Model Physics

DUNE has a myriad of supplemental BSM searches it could perform. These include:

- searches for active-sterile neutrino mixing,
- searches for non-unitarity of the PMNS matrix,
- searches for nonstandard interactions,
- searches for violation of Lorentz symmetry or charge, parity, and time reversal symmetry,

to name a few. Several searches involving theoretical models of dark matter will also occur at DUNE.

Chapter 4

Radiological backgrounds in the DUNE detector

"I hate these filthy Neutrals, Kif. With enemies you know where they stand but with Neutrals, who knows? It sickens me."

— Z. Brannigan

4.1 Low Energy Backgrounds in the DUNE Detector

Numerous radiological backgrounds get considered throughout low-energy simulations. Here, we classify backgrounds into two categories: internal and external background sources. Internal background sources are those due to contaminants in the liquid argon or detector components. External backgrounds are those emanating from outside the cryostat. Additionally, background signals that are both internal and external are present in low-energy physics simulations. Modelling the background signals requires specificity when attempting to study low-energy events that push DUNE's capabilities.

4.1.1 Argon Isotopes

DUNE's detector medium is liquid argon; therefore, some percentage of radioactive argon isotopes will be in the detector. Of all the radioactive argon isotopes, the two prominent radiological backgrounds are ^{39}Ar and ^{42}Ar.

^{39}Ar is a beta-emitter with a Q-value of 565 keV [116]. With such low energy, one would imagine it doesn't present a threat to DUNE physics studies. Unfortunately for DUNE, ^{39}Ar has an activity of $1.01 \pm 0.02(\text{stat.}) \pm 0.08(\text{syst.})$ Bq per kg in atmospheric argon [106]. As a result, ^{39}Ar charge depositions can become absorbed into those from neutrino interactions. Additionally, ^{39}Ar pileup, where multiple individual events occur at similar enough times resulting in the perception of one super-event, can appear as a low-energy neutrino event.

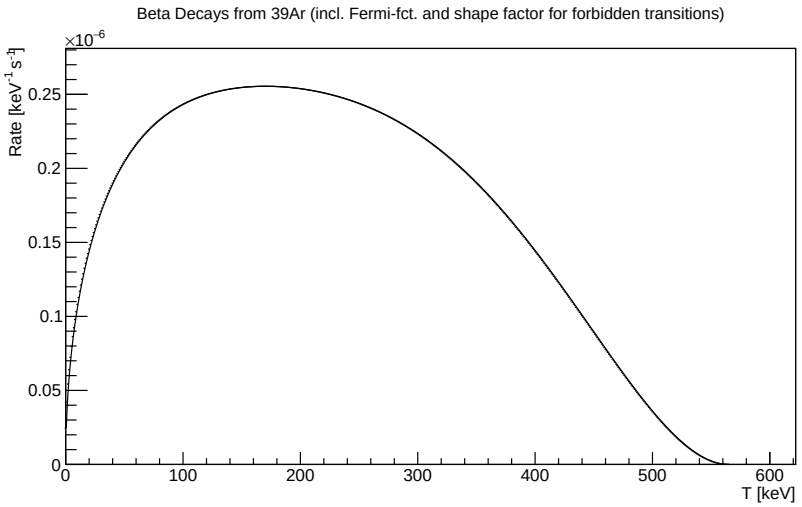

Figure 4.1: The beta spectrum of ^{39}Ar decays.

^{42}Ar is similarly a beta emitter with a Q-value of 599 keV [117]. ^{42}Ar will always decay into ^{42}K, which subsequently beta-decays to ^{42}Ca with a Q-value of 3525.4 [118]. Within DUNE radiological background simulations, ^{42}Ar is modelled as a beta-spectrum with an endpoint of 3.5 MeV. Currently, the best measurement of its activity in atmospheric argon is 92^{+22}_{-46} μBq per kg [119].

4.1.2 Radiological Decays in the APA and CPAs

^{60}Co and ^{40}K decays are simulated, starting at the APAs and CPAs, respectively. The decay channel for ^{60}Co is beta-decay, which results in a ^{60}Ni atom in one of two excited states. Subsequently, the ^{60}Ni atom will release either one or two photons, depending on the energy level occupied. Ultimately, 2.8 MeV is liberated under ^{60}Co decay, carried by the beta-particle and up to two photons.

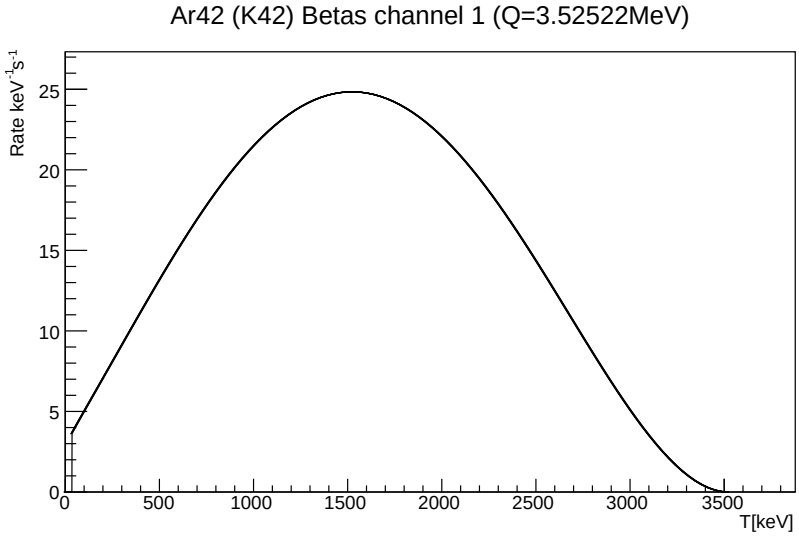

Figure 4.2: The beta spectrum of ^{42}Ar(^{42}K) decays.

^{40}K can decay in several ways. Approximately 90% of the time, it undergoes β^--decay, resulting in a ^{40}Ca, an antineutrino and up to a 1.31 MeV photon. Alternatively, roughly 10% of the time, it forms ^{40}Ar via electron capture, emitting a neutrino and a 1.46 MeV photon. Potassium undergoing electron capture rationalises the abundance of argon in Earth's atmosphere and the prevalence of ^{40}Ar above other isotopes. A third decay mode is also available to ^{40}K: it can β^+-decay to ^{40}Ar; however, this only occurs 0.01% of the time.

4.1.3 Ambiant Radiological Contaminants

The nuclear fallout from atomic weapons testing and nuclear power reactors has produced trace quantities of radioactive isotopes in Earth's atmosphere. One of the more pernicious isotopes to DUNE's low-energy studies is ^{85}Kr. ^{85}Kr is mainly a

Rock type	Uranium (ppm)	Thorium	Th/U ratio
Granite	2.2-6.1	8-33	3.5-6.3
Gabbros	0.8	3.8	4.3
Basalts	0.1-1	0.2-5	1-5
Ultramafics	<0.015	<0.05	variable
Schist	2.5	7.5-19	≥3
Phyllite	1.9	5.5	2.9
Slate	2.7	7.5	2.8

Table 4.1: Table of the uranium and thorium concentrations for different rock types, adapted from [23].

byproduct of nuclear reactors; however, production via spontaneous fission of ^{238}U also contributes. Since the DUNE far site in Lead, South Dakota, has granite deposits [120], contamination by spontaneous fission requires consideration.

^{85}Kr understanding in low-energy physics studies is critical because of its decay modes. Most commonly, ^{85}Kr undergoes beta decay with a Q value of 687 keV [121]. Additionally, however subdominant, it undergoes beta decay with a Q value of 173 keV, followed by a photon emission of 514 keV [122]. In both scenarios, the decay signatures can look deceptively similar to low-energy neutrino interactions. In liquid argon, ^{85}Kr has an activity of 2.23×10^{-1} Bq per kg [106], meaning its rate is low, but important to consider, nonetheless.

Another ambient background that is particularly pernicious to low-energy physics studies is radon. Radon is produced in the decay chains of ^{235}U, ^{238}U and ^{232}Th; all naturally occurring in rock. Table 4.1 shows the concentrations of uranium and thorium in various rock types. Of all the radon isotopes produced, ^{222}Rn is the most important for background consideration. This isotope comes from the ^{238}U decay chain, following an alpha decay of ^{226}Ra.

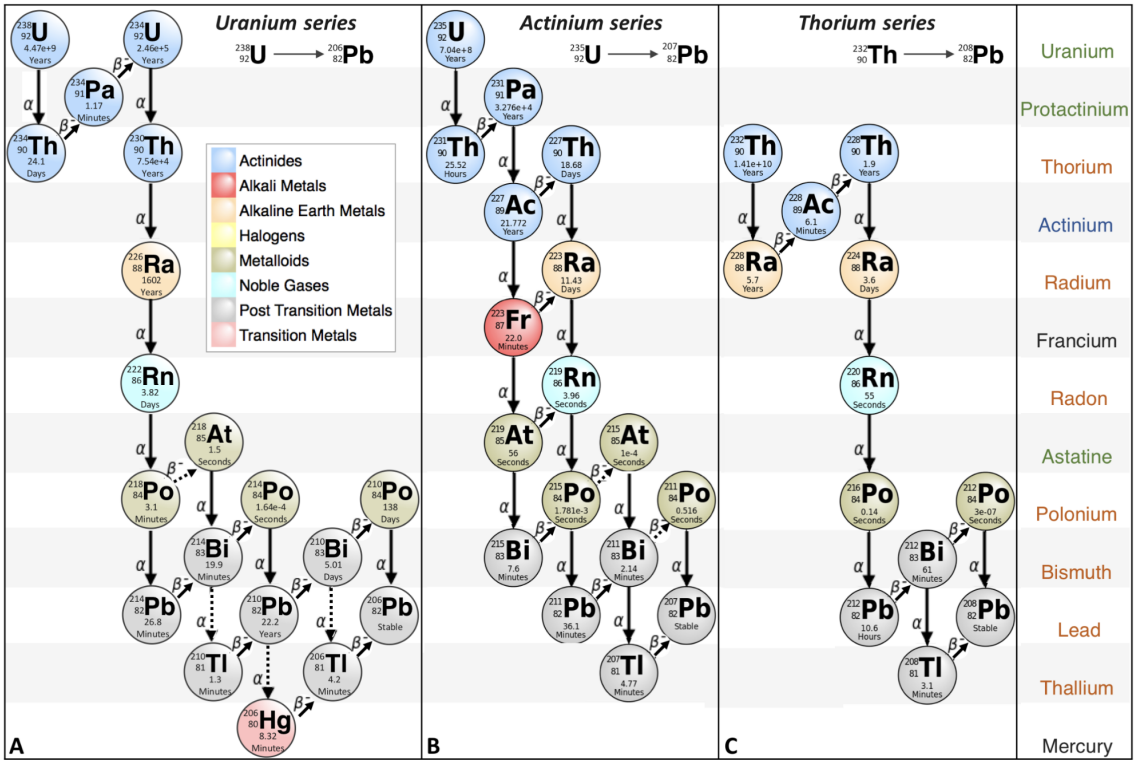

Figure 4.3: The decay chains of a) the ^{235}U b) ^{238}U and c) ^{232}Th [20].

^{222}Rn is responsible for producing several radioactive isotopes, including ^{210}Pb. The presence of this lead isotope is worrisome, as its long half-life (22 years) means it remains in the detector, barring any purification methods. Furthermore, ^{210}Pb leads to ^{210}Bi, which beta-decays to ^{210}Po with a Q value of 1.16 MeV [123]. Additionally, ^{214}Bi is a byproduct of this particular decay chain, which decays to ^{214}Po with a Q value of 3.27 MeV [124].

Isotope	Branching ratio SF/total	Neutron multiplicity
^{235}U	7.0×10^{-11}	
^{238}U	5.45×10^{-7}	1.99 ± 0.03 [125]
^{232}Th	$< 1.8 \times 10^{-11}$	

Table 4.2: Table of the branching ratios and neutron multiplicities for uranium and thorium.

4.1.4 Radiological Neutrons

Neutrons emanate from multiple sources at DUNE. Internal sources include all steel components of the detector, including the cryostat walls, I-beams, APA and CPA frames, to name a few. Additionally, neutrons emanate from external sources, such as cavern rock, concrete and shotcrete. The principal method of neutron production is (α, n) reactions initiated by alpha emitters in the uranium and thorium chains. Subdominant to (α, n) reactions, neutron production also occurs via spontaneous fission (SF) of uranium. When this occurs, multiple neutron emission is possible. In general, ^{238}U is the only isotope contributing to neutron production via spontaneous fission. Table 4.2 shows the branching ratios and neutron multiplicities for spontaneous fission of uranium and thorium.

4.2 Building a Complete 17-ktonne Geometry

4.2.1 Limitations of the Neutron Simulation

The geometry is a fundamental component of the DUNE simulation chain. The propagation of particles handled by `GEANT4` interfaces directly with the geometry, taking into account the dimensions and material compositions of the defined volumes. Commonly, the geometry used in DUNE simulations is the simplified workspace geometry, configured to have 12 APAs arranged in a 1×2×6 configuration in the x, y and z-axes, with z representing the beam axis. For strictly internal studies, such as beam event pattern recognition and DAQ trigger algorithm development, the workspace geometry is sufficiently large. Additionally, one requires significantly less computing power and streamlines the simulation procedure. Unfortunately, when studying phenomena that originate outside the detector, the workspace geometry is not appropriate.

Neutrons emanating from the cavern walls, concrete and shotcrete dominate the total neutron exposure in the DUNE far detectors. Simulating neutrons from these sources cannot be accurately done in the workspace geometry. Primarily, this is due to the absence of volumes such as the I-beams and polyurethane foam insulation that absorb external neutrons. Additionally, neutrons can travel between 30-100 meters in liquid argon between scatters. The workspace geometry is not large enough to contain these events. A 10-ktonne geometry is available in `LArSoft`. It is, however, very simplified compared to the detector design schematics and contains some outdated

material definitions. These reasons motivated the construction of an updated DUNE far detector geometry that more closely resembles the physical detector module, as described in [17].

Constructing the complete 17-ktonne far detector geometry is done using the General Geometry Description (GEGEDE) [126] Python library. This library allows one to design the individual components of a detector geometry and then imbed them within one another sequentially. Essentially, the geometry is constructed from the inside outwards. The library then parses the configuration and produces a `GDML` file, which is usable in pre-existing `LArSoft` simulations.

4.2.2 Volume Hierarchy

Figure 4.4 shows the hierarchal structure of the DUNE geometry. The physical volumes that incase one another define the hierarchy of the geometry volumes. For example, the cryostat must be within the detector enclosure, and the TPC planes must be within the cryostat. Additionally, the dependence of the smaller volumes, like the TPCs, is defined by how `LArSoft` interprets the geometry. The individual volumes and their dependencies will be discussed in detail in Sections 4.2.3-4.2.7

4.2.3 TPC Planes and Active Volumes

Each side of each APA in all DUNE detectors geometries (including the workspace and protoDUNE geometries) has three planes of wires. From outside to inside, these are the two induction planes and the collection plane, labelled U, V and Z,

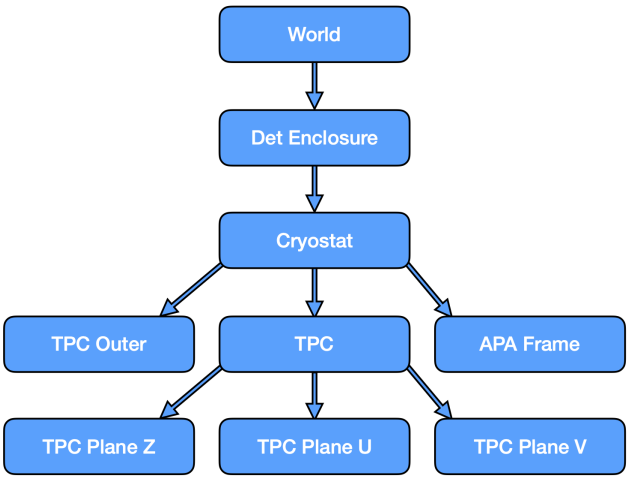

Figure 4.4: This flow diagram describes the top down hierarchy of the DUNE horizontal drift far detector geometry. The connecting arrows denote which features are dependent on a given sub-feature.

respectively. The DUNE technical design papers specify a grounding or G plane as an additional wire plane not present in the geometries. Table 4.3 shows the configuration of the wires in each plane.

Wire Plane	Number of Wires	Wire Pitch [mm]	Wire Angle [deg]	Wire Diameter [μm]
U	400	0.4667	35.71	152
V	400	0.4667	35.71	152
Z	480	0.479	90.00	152

Table 4.3: Configuration of wire planes on the DUNE far detector APAs.

The collection plane is the simplest to construct. Each collection wire runs parallel to the vertical edge of the APA frame. The length of each wire segment doesn't change; therefore, each wire segment is positioned on the plane iteratively.

The induction planes are not as simple to construct. Accuracy is ensured by following a four-step construction process. Step one is calculating the induction plane wire offset. The offset ensures the following induction plane wires are in the correct position, according to the specifications in Table 4.3. The offset values for the U and V planes are 8.74 mm and 10.59 mm, respectively.

Step two is to place the 400 wire segments along the bottom edge of the APA frame. These wire segments extend from the bottom of the APA frame to the horizontal edge of the frame. The lengths of the wire segments are different but easily calculated given the dimensions of the APA frame, the wire offset and the wire pitch.

Step three is placing 348 wire segments that span the entire x-axis of the wire plane. Fortunately, every wire segment is equivalent to one another. Therefore placing the central wire segments is very simple, provided the wire spacing remains consistent.

Finally, step four is very similar to step two. The top and bottom of the wire plane are not exactly rotationally symmetric, but the construction processes have similarities. The top wires complete the induction wire plane with all 1148 wire segments positioned correctly.

The completed TPC volumes in the geometry consist of the wire planes, as specified above, and a cuboid of liquid argon. The liquid argon cuboid covers the APA frame and extends for one drift distance, defined as 3.6 m. With the liquid argon and three wire-planes combined, we have a completed `volTPCActive`. It is only within `volTPCActive`'s that any physics phenomena get simulated. Similar vol-

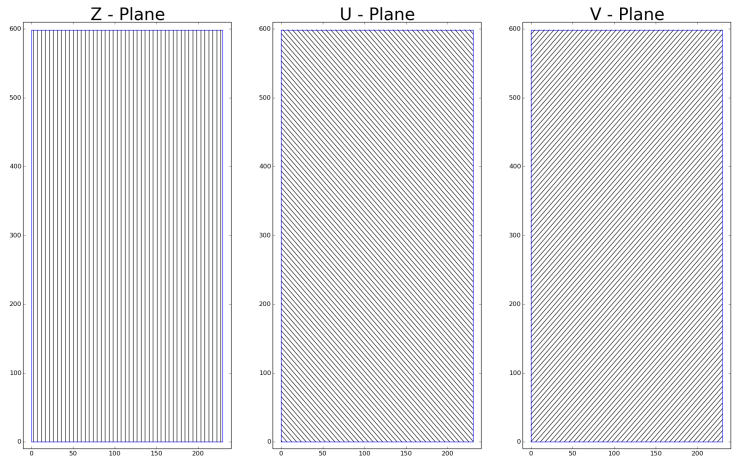

Figure 4.5: Wire configuration for all three wire planes. Only one-tenth of the wires are present to be able to illustrate the wire plane structure.

umes exist on the APA frames next to the cryostat wall. There isn't enough room for a full drift length of liquid argon, so a shorter cuboid is needed. These volumes are `volTPCActiveOuter`'s and can also contain simulated physics phenomena.

In addition to each geometry with the wire segments included, there must be a geometry with no wires. The reason is that generating events and running `GEANT4` doesn't require the wire planes. Running these stages with a `nowires` geometry requires less computing resources and speeds up the processing.

4.2.4 Anode and Cathode Plane Assembly Frames

Hollow steel bars make up the frames of the APA and CPA frames. Four steel bars form a cuboid with dimensions 2.32 m×6.06 m×0.10 m. The ten light paddles get mounted to a central, structural steel beam. Horizontally, there are four structural beams and ten ARAPUCA paddles. Figure 4.6 shows the complete frame structure.

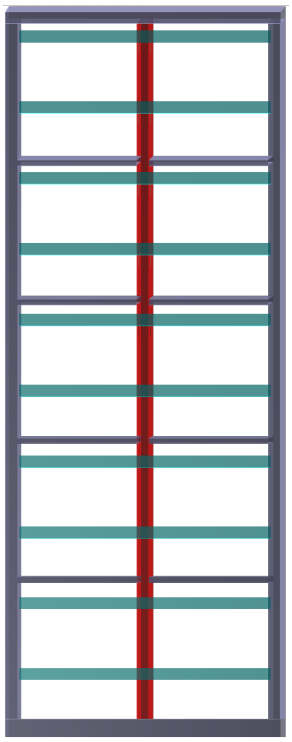

Figure 4.6: A 3D rendering of an individual completed APA frame. The grey and red bars are the structural steel, and the cyan bars are the light paddles that house the ARAPUCA light detectors.

The light paddles are uniformly but not symmetrically spaced. This spacing ensures that when two APA frames get stacked, the spacing between the top and bottom paddles on consecutive frames is consistent. Additionally, acrylic ARAPUCA light detectors sit in the cyan bars, responsible for collecting photon signals from both sides of the frame.

4.2.5 The Cryostat

In its simplest form, the cryostat is a hollow steel box with dimensions 15.1 m $\times$ 14.0 m $\times$ 62.0 m. Around this, two layers provide both structural support and insulation. The first is a layer of plywood, then a thick layer of polyurethane foam. In

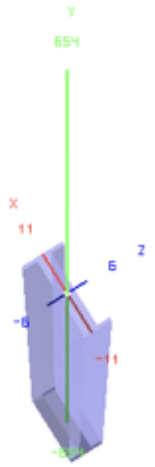

Figure 4.7: The cross-section of the cryostat I-beam.
shows the cross section of the I-beam used to make this structure.

addition to insulating the cryostat, plywood and polyurethane foam are hydrogen-rich materials. These layers will passively shield the detector from external radiological neutrons. Around these layers is another layer of stainless steel, completing the more simple layers of the cryostat.

The most complex feature of the external cryostat is the lattice of I-beams. Figure 4.7 shows the cross-section of the I-beam used to make this structure. Figure 4.8 shows the arrangement of the I-beams around the cryostat shell.

The improved I-beam structure is the most noticeable improvement over previous geometries. With the new structure, we can examine the passive shielding effects the steel beams have on the neutron rate in the detector. Unfortunately, the S460ML steel is radiologically active, making it a neutron source. Ultimately, the I-beam structure will both mitigate and emit neutrons. The neutron production must be accounted for as the overall neutron rate significantly impacts DUNE's low energy physics program.

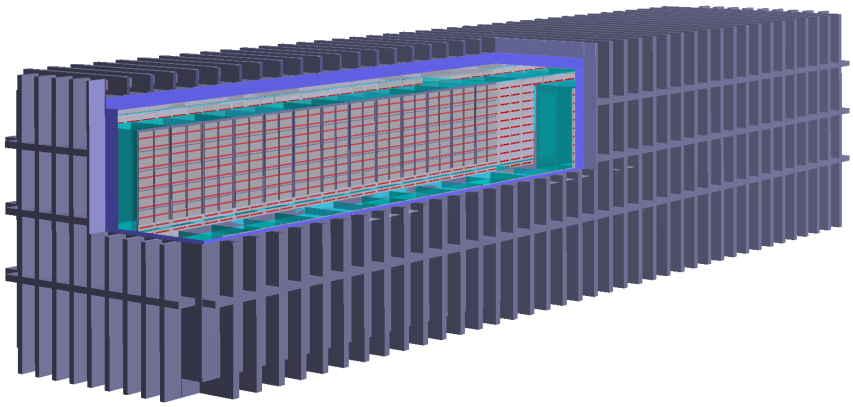

Figure 4.8: Figure showing the arrangement of the I-beams around the cryostat.

Internally, 150 APAs are arranged in a 3 × 2 × 25 configuration. Currently, DUNE uses the "APA-out" configuration, meaning the APAs are closest to the cryostat walls, not the CPAs. Each side of each APA has a `volTPCActive` placed, as described in 4.2.3. There is a dead volume of liquid argon at the up and downs stream ends of the cryostat, defined in the design specifications. Figure 4.9 shows a top-down view of the completed cryostat.

4.2.6 Detector enclosure

The detector enclosure is the hollowed-out underground cavern, inside which the DUNE far detector modules will operate. The detector cavern geometry is defined to have the dimensions specified in the DUNE design reports. Furthermore, the material compositions of the cavern rock more accurately represent the actual rock compositions, similarly to the shotcrete and concrete. Figure 4.10 shows the detector enclosure volume with one detector module in its proper position.

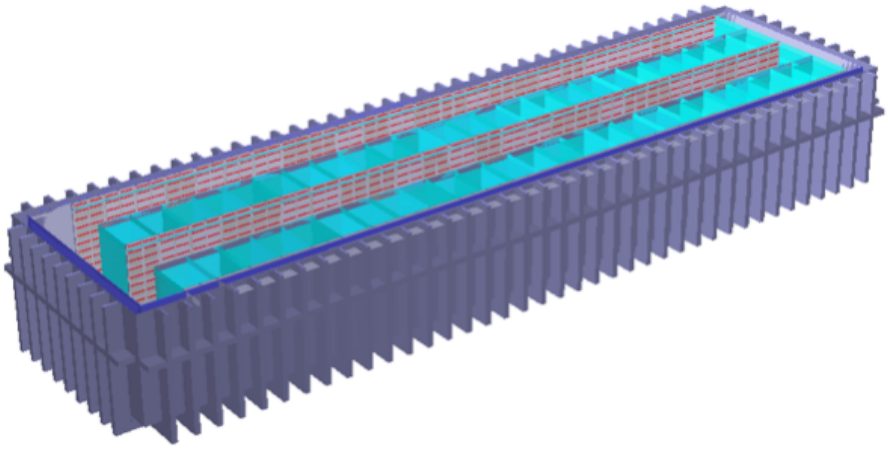

Figure 4.9: A top-down cross-section of the cryostat. The blue boxes show the `volTPCActives` and the red and grey volumes are the APAs.

The detector enclosure geometry includes a material layer that runs along the inside of the faces of the cavern walls. Radiological neutrons are generated in this layer instead of throughout the entire rock volume in the geometry. For simulation purposes, the rock layer's material name gets prefixed with `Radio` and the composition remains the same. Subsection 4.3.1 discusses this layer in more detail as the `RadioRock` volume configuration is integral to ensuring accurate simulations.

Structural materials, such as concrete and shotcrete, are included in the cavern geometry. Due to the inhomogeneity of the cavern walls, it is not possible to perfectly model the shotcrete. Instead, a uniform four-inch layer of shotcrete is defined, which is assumed to reasonably represent the shotcrete. Figure 4.11 shows a zoomed-in corner of the cavern to visualise these layers.

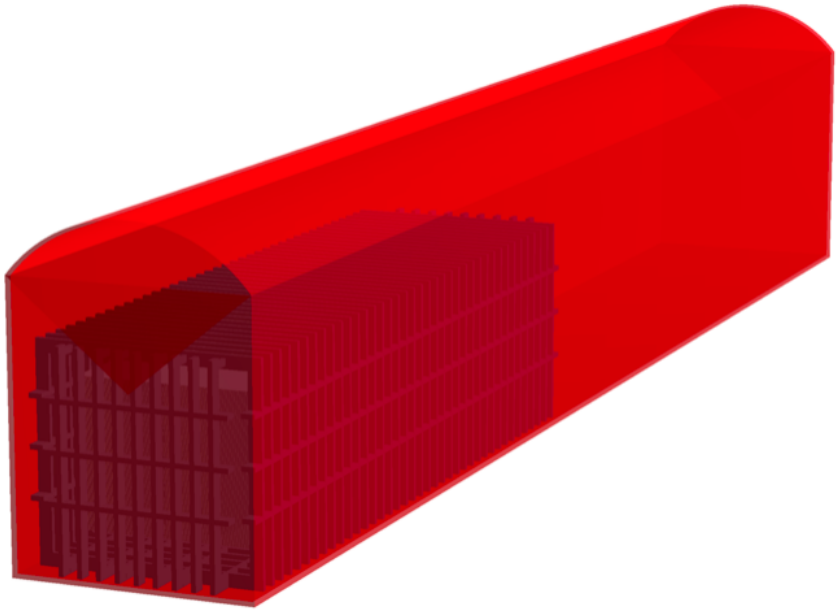

Figure 4.10: A 3D rendering of the detector cavern with one detector module.

4.2.7 Consistency Checks on New Geometries

Two main requirements are the volume naming convention and the position of the volumetric origin. The naming convention is simple to get correct, but, if done inaccurately, `LArSoft` will not generate nor propagate particles. Placing the origin is less simple but very well defined:

- $x = 0$ is the middle of the central wall of APAs,
- $y = 0$ is in the middle of the uppermost and lowermost APAs,
- $z = 0$ is on the front edge of the leading APA.

Figure 4.12 shows the physical position of the (0, 0, 0) coordinate.

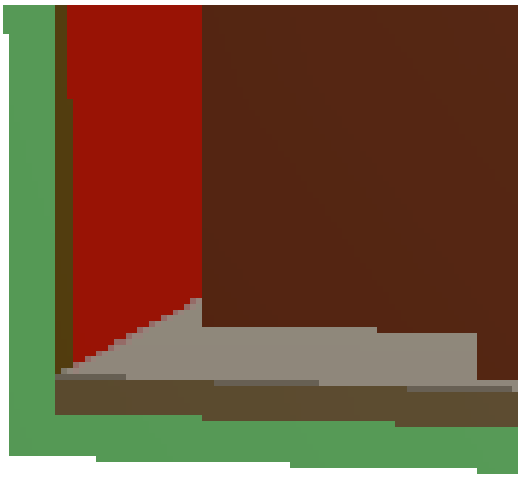

Figure 4.11: A corner of the detector geometry to show the new structural layers. The green layer is the radiologically active rock layer; the red is the shotcrete, brown is the concrete, and grey is the grout.

If any volumes get placed incorrectly or have the wrong dimensions, overlapping volumes can occur in the geometry. Overlaps do not stop the simulations from running but do lead to `GEANT4` potentially confusing the material definitions. Any mistakes of this kind will lead to any physics processes being simulated wrong. Fortunately, `ROOT`'s `TGeoManager` class includes a member function, `CheckOverlaps`, that identifies any errant overlapping volumes in the geometry. Any discovered overlaps get corrected until there are none present in the geometry.

The last check before running any simulations is making sure no gaps are present in the geometry. A gap could present, for example, as air in the cryostat where there should be liquid argon. An additional macro can find any gaps in the geometry. It works by following a particle as it travels through the geometry and outputting the materials as it moves from one to the next. Any gaps found are corrected before using the geometry within `LArSoft`.

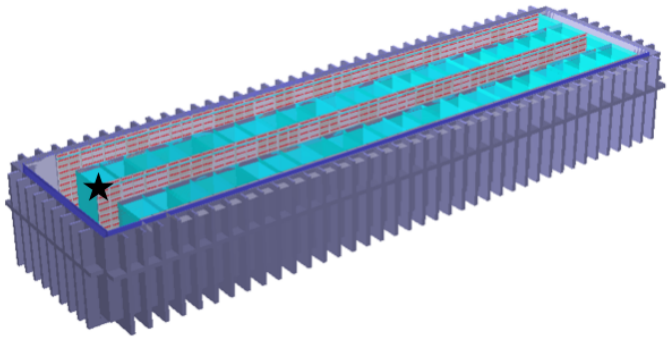

Figure 4.12: The (0, 0, 0) coordinate of the detector geometry, represented by a black star.

4.3 Neutron Simulation in the 17-ktonne Geometry

There are six primary sources of radiological neutrons in the DUNE far detector. These include cavern rock, shotcrete, concrete, steel I-beams, stainless steel warm skin and steel cold skin. Each source gets treated separately to ensure accurate simulations and results.

The 10-ktonne geometry simulations require updated neutron production spectra. Previously, the neutron spectrum used represented a general flux on the detector that combines the (α, n) and spontaneous fission interactions from Uranium and Thorium. Figure 4.13 shows the spectrum previously used in neutron simulations. The neutron production model needs updating to generate physically accurate simulations. The reason is that, for example, the neutron production from the rock will be different to that of the stainless steel. Each material has a different chemical composition leading to different abundances of radioactive isotopes driving neutron production. Furthermore, the spectrum shown in Figure 4.13 assumes the uranium

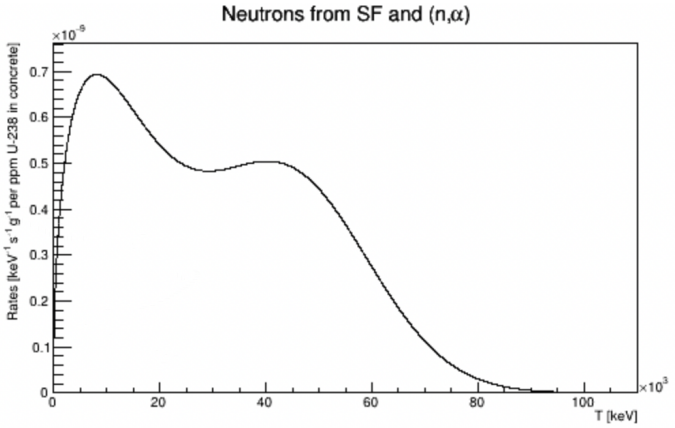

Figure 4.13: The general neutron production spectrum previously used in simulations.

and thorium chains to be in secular equilibrium. Detailed spectroscopic and radiological analyses of the materials offer input to software such as `SOURCES4C` which generates individual neutron production rates.

4.3.1 Neutrons from the Cavern Walls

As mentioned in Subsection 4.2.6, a configurable layer of rock with the material reference `RadioRock` is present in the geometry. `RadioRock` is included so the particle generator, `RadioGen`, only produces neutrons in the specific region. The thickness of the layer is configurable because it is not necessary to generate neutrons throughout the entire rock volume. Defining neutrons to be generated in the `RadioRock` and not the bulk of the cavern rock limits the number of particles simulated and vastly improves simulation efficiency and runtime.

The chemical composition of the rock is used as input to `SOURCES4C` to generate neutron production spectra. The output of this process is four spectra:

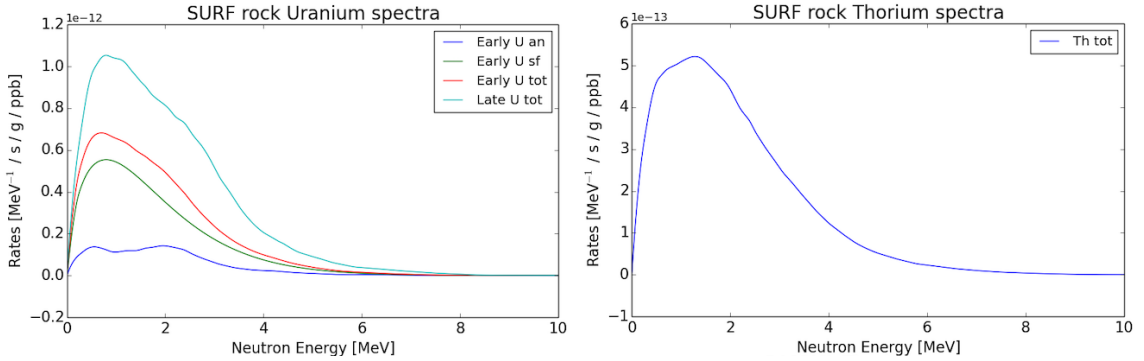

(a) (b)

Figure 4.14: The neutron production spectra for the cavern rock. Figure (a) shows the uranium spectra, and Figure (b) shows the thorium spectrum.

- the (α, n) rate for the uranium chain above radon,
- the spontaneous fission rate for the uranium chain above radon,
- the total rate for the uranium chain below radon,
- the total rate for the thorium chain;

each represented in Figure 4.14.

The rates calculated by `SOURCES4C` are in [MeV s^{-1} g^{-1} ppb^{-1}], meaning evaluating the simulation time is not as simple as counting the number of time windows simulated. Instead, the mass of each volume and the concentration of radiological contaminants are required to evaluate the simulation time and calculate a neutron capture rate. Calculating the simulation time is discussed in detail in Subsection 4.3.3.

4.3.2 Neutrons from Radiologically Active Cryostat Layers

Neutron production from the other radiologically active volumes is similar to that described previously. For each volume, the compositions are inputted to `SOURCES4C` to produce neutron production spectra. These neutron production spectra inform the particle generator when placing neutrons in the appropriate volumes.

4.3.3 Evaluating the Real Time of the Neutron Simulations

`LArSoft` simulations are generally defined to run within a given time window. In previous radiological simulations, this was approximately 4.5 ms. With the neutron simulation described above, one cannot define the simulation time in this way. Instead, the neutron production spectrum and the number of particles produced are combined to evaluate the simulation time.

Evaluating the simulation time is as follows: suppose 10^3 neutrons get produced in the I-beams around the cryostat from the thorium decay chain. The thorium production spectrum for the I-beams steel, when integrated, gives a total rate of 1.28×10^{-12} neutron s^{-1} g^{-1} per ppb of thorium. The measured thorium content in the steel is 24.6 ppb. Therefore the simulation time is

$$T_{\text{sim}} \;=\; \frac{N_{\text{n}}}{C\; M_{\text{vol}}\; \Phi}, \tag{4.1}$$

where N_{n}, C, M_{vol} and Φ are the number of neutrons, radiological contamination in ppb, volume mass and integrated production spectrum respectively. So, for this example, the simulation time would be 1.99×10^4 s or 5.52 hours.

4.3.4 Material Definitions and Radiological Activities

As discussed in Subsection 4.3.1, the chemical composition of the radiologically active materials is an integral feature of the simulations and geometry. The different concentrations of various radioactive isotopes directly impact the neutron production rate and energy spectrum. Additionally, depending on the concentration of hydrogen, different materials can act as passive neutron shielding. Fortunately, the composition is known on the atomic level for materials like steel. For those that are not known, spectroscopic analyses give us the molecular compositions of the undefined materials.

The two types of steel used in the detector are S460Ml and SS304L. Table 4.4 shows the atomic compositions of the two steel types.

	S460ML (by percentage)	SS304L (by atomic content)
ρ [g cm^{-3}]	7.85	8.00
Fe	0.9535	1219
Mn	0.017	36
Ni	0.008	170
Si	0.006	27
Cu	0.0055	-
C	0.0018	3
P	0.0003	1
S	0.00025	1
Al	0.0002	4
N	0.00025	-
Nb	0.0005	-
V	0.0012	-
Ti	0.0005	-
Cr	0.003	365
Mo	0.002	-

Table 4.4: The atomic composition of S460ML and SS304L steels used in the DUNE far detector cryostat.

There are several different kinds of rock naturally occurring at the Homestake Mine. It is unclear which rock type will be dominant in the detector cavern, and the rock composition is not necessarily homogeneous. In light of these approximations, four rock samples are analysed and averaged to provide an approximative input for the simulations.

The four rock samples analysed are #4 Winze, #6 Winze, Governor's Corner and Test Blast Site. These names all refer to different areas of the mine. These samples are processed mechanically and analysed to evaluate their molecular composition and radiological activity. Table 4.5 shows the molecular breakdown of the four rock samples and the average rock calculated based on the samples.

	#4 Winze	#6 Winze	Governor's Corner	Test Blast Site	Average
ρ [g cm^{-3}]	2.60	2.67	2.65	2.68	2.65
Fe_2O_3	0.0	18.0	3.8	16. 4	9.6
MnO_2	0.0	0.1	0.3	0.1	0.1
TiO_2	0.0	0.0	0.0	0.0	0.0
CaO	0.6	0.0	0.0	0.2	0.2
K_2O	8.0	0.7	4.4	0.9	3.5
SiO_2	73.3	40.7	74.9	39.3	57.1
Al_2O_3	15.1	24.8	12.7	27.7	20.1
MgO	0.0	8.9	1.4	8.1	4.6
Na_2O	2.8	0.3	0.8	0.2	1.0
N_2O	0.0	0.0	0.0	0.0	0.0
CO_2	0.0	0.0	0.0	0.0	0.0
H_2O	0.2	6.5	1.7	7.1	3.9

Table 4.5: Table showing the molecular composition of rock samples found in the DUNE far detector cavern.

Interestingly, the water content varies considerably. Ideally, the water content of the rock would be as high as possible, as water is very good at absorbing neutrons. Similarly, the aluminium content varies significantly. The aluminium content of the rock directly correlates to the overall neutron production rate. Therefore, it is best if as little aluminium as possible is present in the materials. Unfortunately, this is not clearly controllable in naturally occurring materials.

The composition of the concrete and shotcrete is possible to control, not necessarily to maximise the water content, but to minimise their radioactivity. Concrete and shotcrete are mixtures of sand, gravel, cement, fly ash and water. We can conscientiously choose sand and gravel from particular suppliers, being mindful of the radiological activity of the components. Table 4.6 shows the composition of the shotcrete and concrete used in the simulations.

	Atomic percentage
ρ [g cm^{-3}]	2.332
O	56.538
Fe	0.132
Mn	0.001
Ca	21.061
K	0.283
Si	4.173
Al	0.514
Mg	0.382
Na	0.120
N	0.067
C	12.005
H	4.724

Table 4.6: Table showing the atomic composition of concrete and shotcrete used to reinforce the DUNE far detector cavern.

Of the various suppliers considered, all mixtures contain the same quantity of hydrogen. The reason is that the amount of water required to make concrete and shotcrete is strictly defined, and no other material other than the fly ash, which comes from a singular provider, contains water. Of all the sand and gravel compositions considered, the one outlined in Table 4.6 minimises the aluminium content. Minimising the aluminium content ensures we use the most radiologically neutral concrete and shotcrete composition.

The only material currently poorly defined and unaccounted for as a neutron source is the polyurethane foam used as insulation in the cryostat. Currently, the polyurethane foam's atomic composition is $C_{54}H_{60}O_{15}N_4$, deduced via spectroscopic analysis on a sample from protoDUNE. The polyurethane foam used in the DUNE far detector will have a silicate content because of the glass fibres within the foam, currently un-

accounted for in the far detector geometry. These glass fibres will have two effects: the neutron attenuation rate will change - presumably lessening the neutron shielding - and increase the overall neutron production due to silicates being radiologically active. Further work is required to account for the addition of the glass fibres; however, the geometry in its present form provides a reasonable first approximation of the experiment.

4.4 Results of Neutron Simulations in the 10-ktonne Geometry

This Section outlines the three studies undertaken on the 10-ktonne DUNE far detector geometry. The first study aims to evaluate the appropriate thickness of the `RadioRock` layer from which rock-neutrons start. The second study evaluates the passive shielding of the layers of the cryostat. Passive shielding is possible to probe with the updated geometry and specified material compositions. Finally, we evaluate the predicted neutron capture rate in one DUNE far-detector module.

4.4.1 Determining the Appropriate Dimensions of Active Radiological Layer of Cavern Rock

Neutrons produced in the rock with energy in the 0 - 10 MeV range can travel around 30 cm between scatters in rock. Therefore, if the radiologically active rock layer is too thin, we may be miss-simulating our events. In contrast, if the radiologically active rock layer is too thick, we simulate more neutrons than is strictly necessary.

In this case, simulations require much more computational resources putting strain on the computer systems. Furthermore, the real-time required to simulate an event increases as the active rock layer thickness increases. Therefore, optimising the thickness of the active rock layer has a two-fold benefit: ensuring physically accurate results and optimising the simulations on a computational level.

The procedure for evaluating the active volume's dimensions has three stages. Initially, six pairs of geometries (ones containing wires and ones without, as required by `LArSoft`) with their `RadioRock` layer thicknesses varied between 20 - 200 cm. Secondly, three 10,000 event simulations get run using each geometry. One for the early uranium chain (everything before ^{222}Rn in the ^{238}U chain), one for the late uranium chain (everything after and including ^{222}Rn) and one for the ^{232}Th chain. Upon completion of stages one and two, the capture rate from each simulation on a particular geometry gets summed. Finally, we compare the neutron capture rate variation as a function of `RadioRock` thickness to deduce the optimised dimensions required.

It is critical to clarify what neutron capture is within this analysis. Four variables from running `GEANT4` are required to verify if an event is a neutron capture. First, the `PDG` code for the particle must be 2112, verifying it is a neutron. Secondly, the end material of the given particle must be LAr. Following this, the position of the capture is crucial. As described in Subsection 4.2.5, there is a dead volume of liquid argon at the up and downstream ends of the cryostat. If a neutron capture occurs within these volumes, it will not produce charge depositions within the view of the APAs. Therefore, the two volumetric cuts are applied, excluding neutron captures whose positions extend past the APAs in the y- (vertical) and z- (beam)

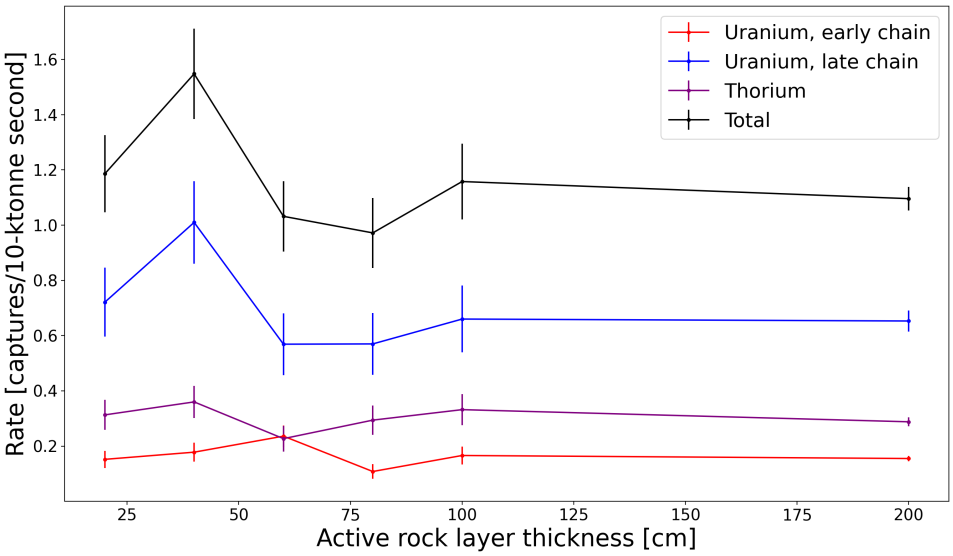

Figure 4.15: The neutron capture rate as a function of radiologically active rock thickness.

axes. No cut on the x-axis is required as there are `volTPCActives`'s at the very outer portion of the liquid argon volume, as described in Subsection 4.2.3. Finally, the end process from `GEANT4` of the interaction must be `nCapture`. Only when all of these conditions are satisfied is a neutron capture considered.

Figure 4.16 shows the variation in neutron capture rate as a function of `RadioRock` thickness. The figure shows a significant fluctuation in capture rate with thinner volumes of radiologically active rock, dominated by the late uranium chain neutrons. These fluctuations level out with thicker active rock volumes and remain consistent towards the upper end of the x-axis.

This study motivated the usage of a 200 cm shell of `RadioRock`. A 200 cm shell of `RadioRock` allows for neutrons to be generated sufficiently deep within the cavern walls and accounts for any neutron saturation that might occur as the particles

propagate within the geometry. Additionally, this value is in agreement with similar studies, such as that carried out by Zhu, Weishi Li and Beacom in their examination of the MeV potential of DUNE [102]. With this configuration, the neutron capture rate contribution from the radiologically active rock is 1.10 ± 0.04 Hz. In comparison, the equivalent contribution from [102] is approximately 81 Hz; however, there are significant differences in the simulations. The first difference is minor but noteworthy - the particle transport library used within `LArSoft` is `GEANT4`, specifically version `v4_10_6_p01`, whereas the equivalent study uses `FLUKA` for particle transport. A difference in particle propagation libraries should not affect the simulations dramatically. Additionally, the other study generated neutron production spectra with `NeuCBoT` using a different material composition. Fundamentally, however, the difference lies in the geometries implemented in the two simulations. In this study, we use the more precise representation of the DUNE far detector module. The comparable study approximated the detector module as a 10-ktonne cuboid of liquid argon. By making this approximation, it does not account for the passive shielding of the cryostat layers, such as the polyurethane insulation and, to a lesser extent, the concrete and shotcrete. The effect of including these layers around the liquid argon is evaluated in the next section. Ultimately, moving forward, we must use a 200 cm layer of active rock in neutron simulations to ensure physically accurate outputs.

4.4.2 Evaluation of the Passive Shielding of the Cryostat

Evaluating the passive shielding of the cryostat layers requires the generation of several new geometries. The general idea is that one starts from a cuboid of liquid argon and then sequentially adds the layers back to the cryostat one at a time. The order of operations is the following:

1. Initially, start with a cuboid of liquid argon,
2. wrap the cold steel around the liquid argon,
3. place the polyurethane foam and plywood around the cold steel,
4. wrap the warm steel around the insulation,
5. order the I-beams around the warm steel,
6. place the concrete and shotcrete volumes against the cavern walls.

For each of the points above, a geometry pair gets constructed. Then, 10,000 events get generated with neutrons originating within the radiologically active rock. Finally, the neutron capture rate gets calculated for each geometry in the same manner as described in Subsection 4.4.1.

Considering only a cuboid of liquid argon, we attain a capture rate of $(1.53 \pm 0.02) \times 10^2$ Hz. Following this, the addition of the SS304L cold steel provides an immediate 30% reduction in the overall capture rate. The next addition to the geometry is the polyurethane foam and plywood layers that compose the insulation around the cryostat. Both materials have high atomic percentages of hydrogen. Therefore, one should expect a significant reduction in the neutron capture rate upon

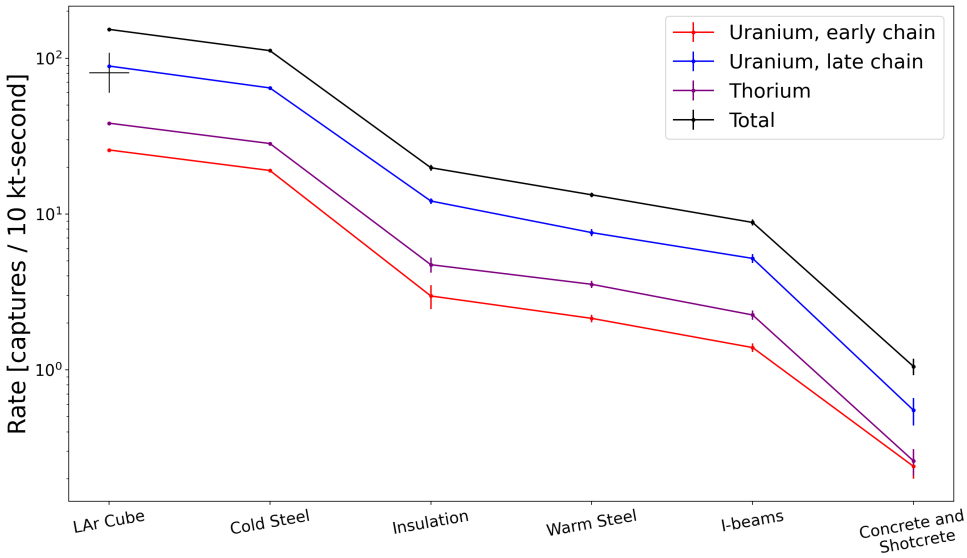

Figure 4.16: The neutron rate attenuation as successive layers of the geometry get added. The black cross above "LAr Cube" represents the points evaluated in [19] for a similar geometry.

the inclusion of these layers. Indeed, we see a reduction from 111.85 Hz to 19.83 Hz going from Cold Steel to Cold Steel and Insulation; a reduction of 82%. Adding the S460ML Warm Skin and I-beams continues to contribute to the reduction in the neutron capture rate. The final significant mitigating layers are the concrete and shotcrete. As mentioned in Subsection 4.3.4 and illustrated in Table 4.6, concrete and shotcrete have significant water content. Therefore, similarly to the insulation, we expect significant neutron mitigation due to these volumes. This expectation is confirmed as the total neutron capture rate falls from 8.83 Hz to 1.04 Hz - a reduction of 88%. Unfortunately, concrete and shotcrete are radiologically active and, therefore, contribute to the neutron capture rate while also attenuating the neutron

flux from the cavern rock. Therefore, this 88% refers only to the attenuation effect. The contribution from the shotcrete and concrete to the neutron capture rate still requires evaluation.

From this study, we see a significant benefit from thick insulation layers and the presence of the shotcrete and concrete. The complex structure of the DUNE far detector modules provides significant passive shielding from radiological neutrons. Without these structures, a detector module would experience a neutron capture rate of 153 Hz. With all of the complexities included, this rate is reduced to 1.05 $\pm$ 0.13 Hz, an overall reduction of 99.3%. Two points arise from this study. Firstly, the radiological activity of the concrete and shotcrete should not negate the shielding they provide. Secondly, these studies do not account for the radiological activity of the polyurethane foam due to the silicate content. Sourcing concrete and shotcrete components from vendors providing the lowest radiological activity controls the first issue. Further analyses are required to determine the specific silicate content of the polyurethane foam and its radiological activity. Once this information is available, two updates must occur. First, all geometries will include an up-to-date polyurethane composition. Secondly, simulations of neutrons emanating from the polyurethane will get the same treatment as those discussed in this Subsection.

4.4.3 Water shielding on the 17-ktonne geometry

As discussed, hydrogen-rich materials are excellent neutron absorbers. One might imagine filling the space in the I-beam structure of the cryostat with water containers. Naively, this should reduce the neutron capture rate observed. The question is: to what extent?

As before, events get generated within the cavern rock, shotcrete, concrete and I-beams. Following generation, the neutrons are allowed to propagate about the geometry. Of the 1,000 events generated, no neutron record of captures emerged for rock, shotcrete or concrete. Of the neutrons generated in the I-beams, less than 1% got captured in the active area of the liquid argon. Table 4.7 displays the component by component contribution to the overall capture rate. Where no captures occurred, a statistical limit is, instead, given.

Source	U_{early}	U_{late}	Th
Rock	$< 1.22 \times 10^{-4}$	$< 1.44 \times 10^{-3}$	$< 2.79 \times 10^{-4}$
Concrete	$< 2.16 \times 10^{-5}$	$< 1.10 \times 10^{-5}$	$< 4.81 \times 10^{-7}$
Shotcrete	$< 2.18 \times 10^{-5}$	$< 1.14 \times 10^{-5}$	$< 4.80 \times 10^{-7}$
I-Beams	$(2.68 \pm 0.07) \times 10^{-2}$		$(2.35 \pm 0.01) \times 10^{-3}$

Table 4.7: The neutron capture for external neutron sources with water shielding present between the detector I-beams. All values given in units of captures / 10 ktonne-second

Observations of the effect of water shielding show it to be very effective for shielding neutrons. Effectively, all of the neutrons from the cavern rock, shotcrete and concrete get blocked, with only those emanating from the I-beams piercing the water shielding and all cryostat layers. Placing water blocks around the cryostat would drastically help mitigate the neutron background without impacting neutrino searches. If it is possible to wrap a 17-ktonne detector in water is less apparent.

4.4.4 Evaluation of the Total Neutron Capture Rate

The information gathered in Subsection 4.4.1 about the simulated rock thickness, and the spectra described in Subsections 4.3.1 and 4.3.2, the total neutron background rate can be estimated. The simulation procedure is similar to that previously described. 10^4 events get generated for each radiologically active material for each of the decay chains. Table 4.8 shows the results of all the simulations run.

	Capture rate [Hz]	Total [Hz]
Concrete U-early	$(6.81 \pm 0.42) \times 10^{-2}$	
Concrete U-late	$(3.44 \pm 0.25) \times 10^{-2}$	$(1.11 \pm 0.05) \times 10^{-1}$
Concrete Th	$(8.99 \pm 0.59) \times 10^{-3}$	
Shotcrete U-early	$(7.90 \pm 0.14) \times 10^{-1}$	
Shotcrete U-late	$(4.90 \pm 0.10) \times 10^{-1}$	1.40 ± 0.02
Shotcrete Th	$(1.15 \pm 0.02) \times 10^{-2}$	
I-Beams U-early	$(1.47 \pm 0.03) \times 10^{-1}$	
I-Beams U-late	$(6.42 \pm 0.14) \times 10^{-2}$	$(2.13 \pm 0.04) \times 10^{-1}$
I-Beams Th	$(1.42 \pm 0.03) \times 10^{-3}$	
Warm Skin U-early	$(5.91 \pm 0.21) \times 10^{-2}$	
Warm Skin U-late	$(2.56 \pm 0.09) \times 10^{-2}$	$(8.53 \pm 0.23) \times 10^{-2}$
Warm Skin Th	$(5.97 \pm 0.21) \times 10^{-4}$	
Cold Steel U-early	$(1.33 \pm 0.04) \times 10^{-1}$	
Cold Steel U-late	$(6.92 \pm 0.23) \times 10^{-2}$	$(2.03 \pm 0.05) \times 10^{-1}$
Cold Steel Th	$(1.04 \pm 0.03) \times 10^{-3}$	

Table 4.8: Table showing the capture rates and simulations statistics for neutrons produced in radiologically active sources other than rock.

From combining the values in Table 4.8 with those calculated in Subsection 4.4.1, the total neutron capture rate in one detector module is estimated to be 3.05 ± 0.13 neutron-captures / 10-ktonne second. Interestingly, the dominating contributor to the neutron capture rate is the shotcrete. The shotcrete is on all four vertical walls

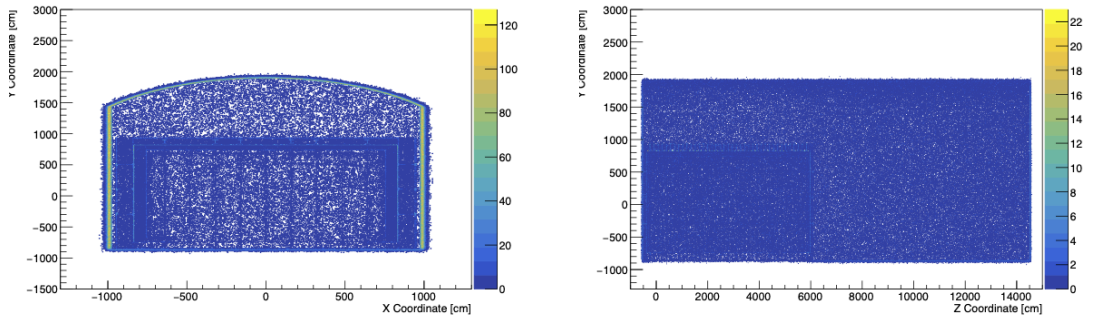

(a) (b)

Figure 4.17: The capture position of neutrons generated within the shotcrete around the geometry. Figure a) shows the x-y view, figure b) shows the z-y view.

and the ceiling; therefore, there is a large surface area for neutrons to emanate. If we look at the positions of neutron capture in the cavern, we see neutrons from the shotcrete suffuse over the entire cavern and hit the cryostat. One might think neutrons from the rock would be the leading contributor to the neutron capture rate. However, aided by their water content, the concrete and shotcrete layers act as passive shielding against the rock neutrons. Ultimately, the higher flux of neutrons produced in the rock gets significantly diminished before the neutrons reach the interior of the cryostat.

By comparison, the concrete contributes far less overall neutron capture rate, despite being a much thicker volume. The rear half of the concrete is not incident to the cryostat, making it more unlikely for these neutrons to penetrate the liquid argon. Figure 4.18 shows the capture position of neutrons generated in the concrete.

Intuitively, one might predict that the cold steel would be a notable contributor to the total neutron capture rate. There are no layers between it and the liquid argon to act as passive shielding. Fortunately, the cold steel is thin, and its radiological

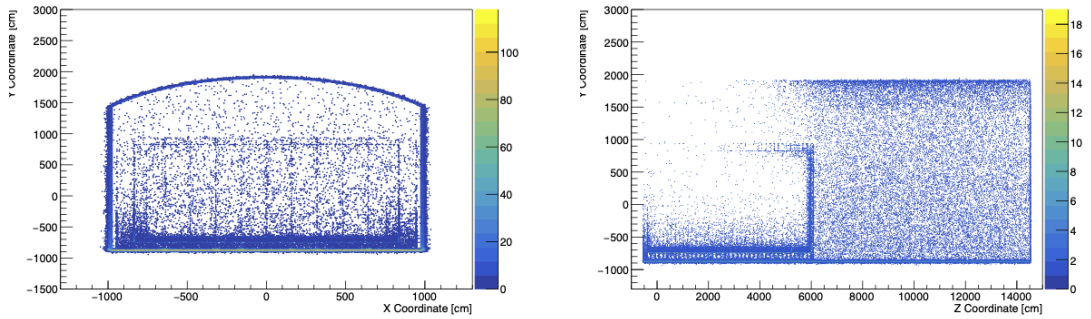

(a) (b)

Figure 4.18: The capture position of neutrons generated within the concrete around the geometry. Figure a) shows the x-y view, figure b) shows the z-y view.

impurity is low. These features result in the neutron production rate being relatively slow. For example, for the late uranium chain, 9179 neutrons are generated, equating to 3.8 hours of real time being simulated, following Equation 4.1.

This study is not entirely complete in its current form. Materials, such as the copper-beryllium alloy wires on the APA and the steel frames of the APAs and CPAs, are radiologically active. Additionally, the PCBs on the APAs will also generate neutrons. There is limited scope for shielding neutrons from these materials as they are directly inside the liquid argon. Fortunately, these are all considered subdominant neutron sources and, therefore, should not impact the physics potential of DUNE.

As previously mentioned, the radiologically active silicates in the polyurethane foam are not implemented in the geometry nor accounted for as a neutron source. As material assays progress and further information are released, the polyurethane contribution to the neutron background rate will be simulated and added to the results tables.

Chapter 5

Solar Neutrino Analysis

"They said it couldn't be done, Kif. But here we are, stealing an unlimited supply of birthday-grade helium from the unsuspecting moon." "Sun." "At night, it's called the moon."

— Z. Brannigan and K. Kroker

Solar neutrinos are of particular interest to DUNE. Observation of the ^{8}B solar neutrino flux was possibly one of the most paradigm-changing measurements in particle physics. Beyond ^{8}B, numerous helium-generating interactions produce neutrino fluxes. One example is the CNO neutrinos, which have high flux compared to ^{8}B but significantly lower energies, ranging from 0-2 MeV.

CNO neutrinos encode intrinsic information about the Sun's metallicity. A high solar metallicity would result in a higher CNO neutrino flux. A measurement of the CNO flux would elucidate which metallicity model more accurately represents our Sun.

This chapter discusses the procedure followed for a CNO analysis at DUNE. The analysis aims to answer two questions: what is the feasibility of detecting CNO neutrinos at DUNE, and what are the requirements thereof? Additionally, if DUNE can detect CNO neutrinos, is DUNE sensitive to intrinsic solar metallicity? First, the simulations required in the analysis get described. These include the main radiological backgrounds and solar neutrinos and how these get translated into digital detector information. Following the simulation, the extraction of the CNO interaction rate at DUNE gets discussed. Various optimisations are considered to minimise the uncertainty of the CNO rate. Finally, a likelihood approach gets explored to determine two queries: what is DUNE's likelihood of observing CNO neutrinos and are different metallicity models separable at DUNE?

5.1 Simulations

Numerous simulations are required to perform any analysis pre-data. Great care is required when designing and running these simulations, as they must approximate the expectations of the DUNE modules. The `LArSoft` framework generated all simulations discussed hereon.

5.1.1 Simulating radiological backgrounds

Seven main low-energy radiological backgrounds comprise the expected backgrounds at the DUNE far detector. These include: ^{39}Ar, ^{42}Ar, ^{60}Co, ^{40}K, ^{85}Kr, ^{222}Rn and radiological neutrons. To simulate these, one requires accurate nuclear decay models. Amongst the options for generating nuclear decays, the best choice was to implement `Decay0` [127] into the simulation pipeline. `Decay0` offers many solutions to issues not addressed in legacy `LArSoft` simulations. Initially developed for SuperNEMO [128], a low-energy $0\nu\beta\beta$ experiment, `Decay0` has been adopted by others including SNO+.

Previously, the generation of nuclear decays involved simply sampling energy spectra for an alpha, beta and gamma emission. While this is valid for decays such as ^{39}Ar, no considerations of decay chains are taken. Accurately simulating ^{42}Ar and ^{222}Rn requires the components of the decay chains to which they belong. `Decay0` allows for singular isotope decays and decay chains, assuming they're in equilibrium.

Singular isotope decays require some key variable definitions to run within `LArSoft`. In the simplest form, these are the isotope that will be decaying, the geometry volume within which the decay occurs (such as those discussed in Subsections 4.2.2-4.2.6), the material the decay occurs in, and the decay rate per unit volume. For example, for ^{39}Ar, the `LArSoft` generator definition would look as follows.

```
dune10kt_1x2x6_39Ar_in_LAr:{
    module_type: "Decay0Gen"
    isotope: "Ar39"
    volume_rand: "volCryostat"
    material: "LAr"
    BqPercc: 0.00141
}
```

Listing 5.1: An example code block for generating nuclear decays.

Functionally, the structure of this block is the same for ^{85}Kr and ^{60}Co, with updated parameters where appropriate.

Structurally, simulating decay chains is similar to that of single isotopes. The difference is the definition of a `decay_chain` list, containing arbitrarily many isotopes. When a `decay_chain` is declared, `Decay0` knows to generate nuclear decays for each isotope in the chain. One issue at the time of writing is that all isotopes are assumed to be in equilibrium. If, for example, the ^{238}U chain is not in secular equilibrium, one must define separate generators for separate sections of the total decay chain. Listing 5.2 shows a section of the generator definition for the uranium chain. The generator for ^{42}Ar is functionally similar.

```
decay_chain:{
    isotope_0:"U238"
    isotope_1:"Th234"
    isotope_2:"Pa234m"
    isotope_3:"U234"
    isotope_4:"Th230"
    isotope_5:"Ra226"
    isotope_6:"Rn222"
    isotope_7:"Po218"
    isotope_8:"Pb214"
    isotope_9:"Bi214"
    isotope_10:"Pb210"
    isotope_11:"Bi210"
    isotope_12:"Po210"
}
```

Listing 5.2: An example code block for generating nuclear decay chains.

Lastly, simulating neutrons in the workspace geometry is unique compared to decaying isotopes. Because neutron generation occurs inside and outside of the cryostat, accurate simulation is challenging. It does not suffice to generate neutrons outside the geometry and propagate them into the smaller geometry. Unfortunately, the workspace geometry is a representative portion of the 10-ktonne geometry, not a scaled-down version of the detector.

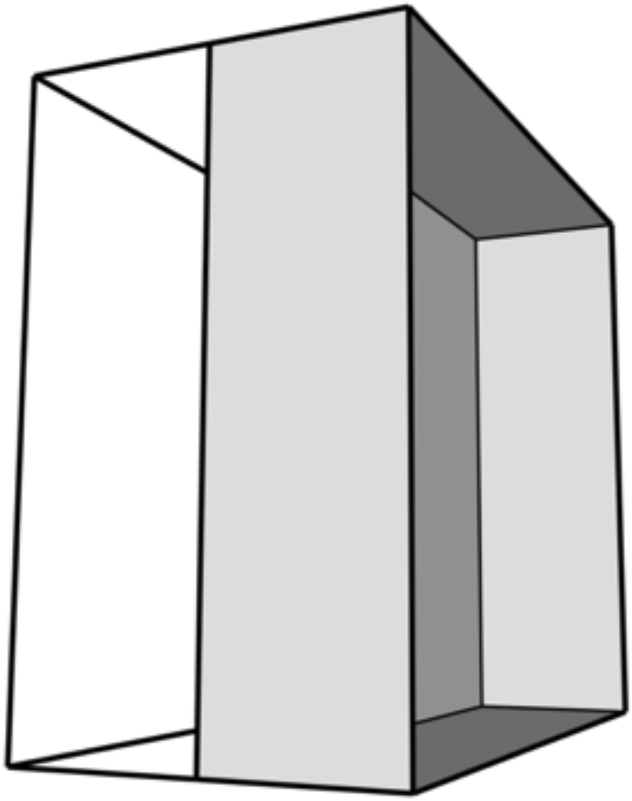

Figure 5.1: A wireframe representation of the workspace geometry with grey panels showing the neutron origins.

Neutrons seed in five representative panels within the geometry. Four panels spanning one drift length on the front, back, top and bottom of the geometry represent neutrons entering along the y and z-axes of the detector. The fifth panel covers the array of APAs, representing neutrons entering the detector along the x-axis. The shaded panels in Figure 5.1 represent the panels from which neutrons emanate.

The neutron rate per unit volume implemented in legacy simulations assumes 10 neutrons/y/g per 10 ppm of concrete, with an assumed density of 2.40 g cm^{-3}. These parameters equate to a rate of 7.6×10^{-6} Bq cm^{-3}. However, with this input, the radiological neutron capture rate is significantly higher than calculated

in the 10-ktonne geometry, 4.4.4. Therefore, the neutron production rate requires tuning. Iteratively, one alters the rate value, and a new sample of 10,000 events gets generated. Then, the neutron capture rate is re-evaluated and compared to the estimate from the 10-ktonne simulations. This process continues until the capture rate in the workspace geometry matches that of the complete geometry. Ultimately, the production rate implemented is over one hundred times smaller than the initial value.

Background simulations consist of 10,000 events[1], with each background present in each running of the simulation. Calculating an event rate for a radiological background is simple. A `LArSoft` event is a determined length of time, and radiological backgrounds have a defined activity in the simulations. Therefore, calculating an event rate is simply the number of interactions in the total time simulated:

$$R = \frac{N_{inter.}}{N_{evts.} T_{evt.}}. \tag{5.1}$$

It is not necessarily this simple for other simulations.

5.1.2 Simulating solar neutrinos

Low energy neutrino simulation of the $\mathcal{O}(1-100)$ MeV starts with `MARLEY`, Model of Argon Reaction Low Energy Yields [129]. Two interaction processes are available in `MARLEY`, charge-current (CC) and elastic scattering (ES) interactions. Technically,

[1] An event is one drift window.

MARLEY can simulate neutral-current (NC) interactions; however, the inputs for NC interactions are comparatively basic, containing only one Fermi matrix element, $B(F)$.

MARLEY can generate events in numerous energy configurations, including monoenergetic neutrinos, energies sampled from a beta function, flat spectra, and others. Here, sampling energy values from a TGraph is the most appropriate. Solar neutrino energy spectra taken from [130] are formatted into individual TGraphs for input. The integral of each solar neutrino spectrum is 1, meaning it is a probability density function, PDF, and does not represent the neutrino flux. Whether the spectra are probabilities or actual fluxes is unimportant, as MARLEY is agnostic to the integral of the spectrum when interfacing with LArSoft. MARLEY 's sampling modality becomes particularly convenient should one want to study different metallicity models of the Sun without running twice as many simulations.

With an energy value sampled from the relevant distribution, MARLEY produces one interaction of a given type (in this case, either CC or ES) somewhere random within the active volume of the detector geometry[2].

Similarly to the radiological backgrounds, each solar neutrino spectrum informs 10,000 isotropically simulated events. In contrast to the radiological backgrounds, however, only one neutrino interaction is simulated per event. Therefore, the number of interactions is not related to an interaction rate. Evaluating the solar neutrino rate is discussed in Subsection 5.3.1.

[2]See 4.2.3 for information on active-volumes.

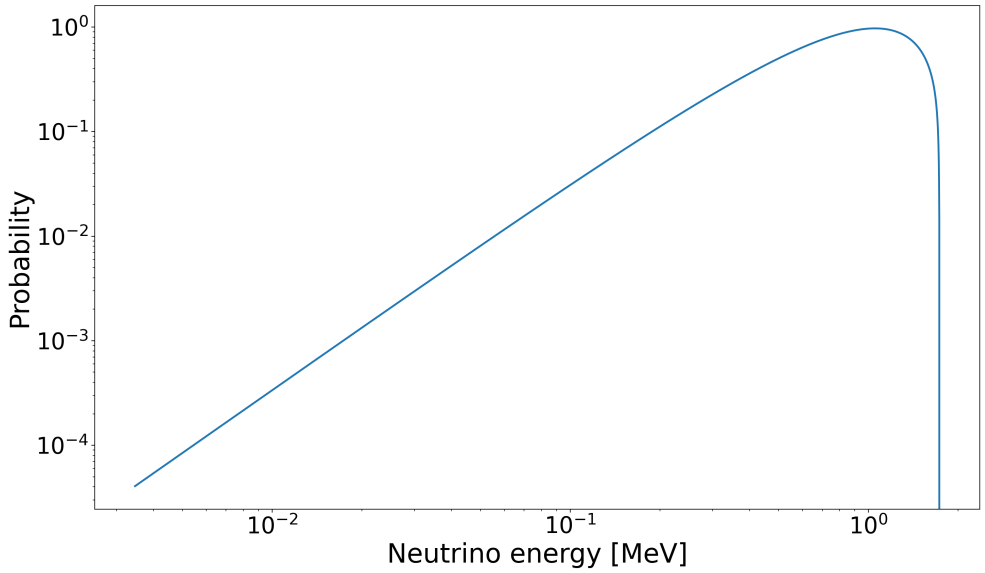

Figure 5.2: The neutrino energy PDF for ^{15}O neutrinos [21].

5.2 Event Clustering and Triggering

The DUNE detector does not see events like pictures of particles but as depositions of charge in time and space. On their own, charge depositions, or hits, do not give an informative view of physics processes. However, by combining hits into larger groups of hits - or clusters - one gets a much more informative view of physics processes inside the detector.

There are many clustering algorithms to choose from, as clustering is an integral part of modern machine learning. Some examples are:

- k-means clustering [131], where an algorithm attempts to organise points into k unique clusters,

- hierarchical clustering [132], which (as the name suggests) attempts to build a hierarchy of clusters,
- density-based clustering [133], which assumes clusters are regions of high information density.

There are many more clustering algorithms available, but they all share a flaw making them inappropriate for low-energy physics studies: they are complex computationally and in terms of memory.

As an example, one can look at the complexity of hierarchical clustering. Hierarchical agglomerative clustering is a procedure whereby every datum seeds a unique cluster, and these clusters are combined when appropriate. The time complexity of this algorithm is $\mathcal{O}(n^3)$ and the space complexity is $\Omega(n^2)$. These complexities make hierarchical clustering too inefficient for modest datasets, let alone the quantity of data DUNE will produce. One can improve the time efficiency by utilising heap data structures. Doing so improves the time complexity to $\mathcal{O}(n^2 \log n)$, with the tradeoff of diminishing the space complexity to $\Omega(n^3)$. Despite this improvement, the memory costs make this clustering approach impractical. K-means clustering is significantly more efficient but requires knowledge of the number of clusters before execution.

5.2.1 Low-energy clustering algorithm

A clustering module, `Clustering` [134], is available for low-energy physics studies at DUNE. Within this module, some specific data objects require definition. These are hits and clusters.

The `Hit` object represents all the information one can acquire from a single charge or light deposition. Focussing on charge depositions, the variables of interest are:

- View, the wire plane the charge deposition comes from (U, V, Z),
- Gen type, the Monte Carlo generator responsible for producing the charge deposition,
- Channel, the APA channel number the charge deposition occurred on,
- Time, the time (in ticks[3]) the charge deposition occurred at,
- SADC, the summed ADC of the charge deposition (approximately the integral of the charge deposition waveform),
- RMS, the length of time the deposition's waveform is over the hit-finder threshold.

The clustering begins with a vector of `Hit` objects. These get ordered by their channel numbers with a `quicksort` algorithm, a highly efficient sorting algorithm[4]. Following this, one can define a new vector to hold `Hit` objects, which we will refer to as channel clusters. These channel clusters get populated with `Hit` objects whose channel numbers are within a defined window.

To illustrate this, suppose we have hits with channel numbers as follows:

15	19	16	18	5	8	2	3	1	9

.

[3]Ticks are the detector time unit based on the sampling frequency of the DAQ, equivalent to 0.5 μs.

[4]The quicksort algorithm is elaborated on in Appendix A.

This would become

| 1 | 2 | 3 | 5 | 8 | 9 | 15 | 16 | 18 | 19 |.

If we impose that consecutive hits must be within two channels of each other (as an example), then our hits would be grouped as follows:

| 1 | 2 | 3 | 5 | | 8 | 9 | | 15 | 16 | 18 | 19 |.

Following this, the `Hit` objects within the channel clusters get ordered in terms of hit-time. In continuation, each cell is now represented with an $\mathrm{HT}_{\mathrm{HC}}$ value, where HT is hit-time, and HC is hit-channel. So, the leftmost cluster becomes

| 12_1 | 15_2 | 20_3 | 13_5 |.

Ordering in terms of hit-time yields

| 12_1 | 13_5 | 15_2 | 20_3 |.

If we impose that consecutive `Hit` objects must be within two ticks of each other (as an example), our clusters become

| 12_1 | 13_5 | 15_2 | | 20_3 |.

A cluster must contain more than one `Hit` by definition. Therefore, | 20_3 | would be discarded, leaving | 12_1 | 13_5 | 15_2 | as a fully formed TPC cluster.

5.2.2 Clustering complexity

Ordering a vector has a time complexity of, at best, $\mathcal{O}(n \log n)$. Splitting the vector into channel clusters is a strictly linear process, $\mathcal{O}(n)$. Fortunately, the number of new vectors that require storage will always be less than or equal to the number of entries. Because vectors in C++ are linear in space, the space complexity so far is, at worst, $\Omega(n)$.

Repeating this process, but replacing n with m where $m \leq n$ makes the overall time complexity, at worst, $\mathcal{O}(n^2 \log n)$. By extension, the overall space complexity is $\Omega(n^2)$. This procedure is more time-efficient than previously described clustering algorithms. However, this is a simple algorithm designed to be lightweight. The precision of this algorithm is likely to be lower than that of more complex algorithms.

5.2.3 Trigger conditions

The trigger model utilised in low-energy studies is simple by design. Essentially, the trigger is a list of thresholds on various cluster parameters. Each parameter gets set to reflect the difficulty of observing low-energy events, such as solar neutrinos, at DUNE. As much information as possible is allowed to get through the trigger; in theory, maximising the low-energy data from solar neutrinos but simultaneously allowing low-energy background data through too.

The trigger parameters for TPC clusters are:

- the minimum required hits in a cluster,

- the minimum number of channels hit in a cluster,
- the minimum breadth of channels hit by a cluster,
- the minimum required charge deposited by a cluster.

As noted in Subsection 5.2.1, the minimum number of hits required to constitute a cluster is two. Therefore, the minimum number of hits required to go through this loose trigger is also two. The minimum number of channels a cluster must span gets set to one. Because low-energy clusters can be only two hits, they may occur on the same wire. The minimum channel breadth and charge deposition are both set to zero. This allows as much low-energy information through the selection model as possible.

5.2.4 Solar Neutrino Trigger Efficiency

Trigger efficiency curves represent DUNE's ability to record a given event. They allow one to say a neutrino of energy E has a probability p of passing the low-energy trigger thresholds. Knowing the trigger efficiency later allows one to predict the overall solar neutrino rate.

Calculating the trigger efficiency involves analysing many events over a range of energies. For the study discussed in this chapter, 10^4 neutrinos generated in the energy domain of ^{17}F solar neutrinos inform the efficiency curve. ^{17}F has the highest energy endpoint of the CNO neutrinos expected from the Sun. Therefore, its energy range gives the most extensive efficiency curve. From this point, three different triggering options get considered.

Collection plane only triggering

With the event simulation and clustering executed, the neutrino energy is extracted from the simulation's truth information. The neutrino energy gets added to a `TEfficiency` object, weighted by a true or false value depending on whether the cluster did or did not pass the trigger. Using a `TEfficiency` is convenient as it is essentially a histogram, scaled such that the maximum value is 1. Only clusters formed on the collection plane that pass the trigger criteria get considered under this model.

Collection plane or induction plane triggering

The *collection-or-induction* trigger model is largely similar to collection plane only clustering. The clustering and triggering procedure is executed, as before, on the collection plane. In addition, the same procedure gets executed on both induction planes. Then, if a triggering cluster occurs on any plane, the `TEfficiency` plot is updated. The collection-or-induction plane model increases the number of opportunities for a charge deposition cluster to trigger by a factor of three.

Collection plane and induction plane triggering.

The third trigger model involves a cluster passing the trigger conditions on the collection plane and at least one induction plane. However, naively pairing clusters on different planes does not imply that they're from the same event. To this end, additional conditions on cluster pairing require implementation. These include:

- paired clusters must be on the same APA,
- paired clusters must be in the same TPC active volume,
- paired clusters must occur within a specified time frame, with induction plane clusters occurring before collection plane clusters.

Only when the conditions above are met is the `TEfficiency` updated to reflect the trigger status of a given simulated neutrino.

In summary, the neutrino energy from the `MARLEY` generator gets recorded. Under collection plane only triggering, the event is assigned a true or false value reflecting whether a cluster passing the triggering conditions occurs on the collection plane. Under collection-or-induction plane triggering, the event gets assigned a true or false value reflecting whether a cluster passing the triggering conditions occurs on any plane. Finally, under collection-and-induction plane triggering, the event gets assigned a true or false value reflecting whether at least two coincident clusters occur, with one being on the collection plane. The energy-trigger-status indicators get added to a `TEfficiency` `ROOT` object.

A large sample size, in this case, 10^4 ^{17}F CNO neutrinos, forms the dataset with which the efficiency curves get calculated. Figure 5.3 shows the efficiency curves for each trigger model. The key observable from the trigger efficiency curves is a non-zero efficiency in the energy regime of the CNO neutrinos. Fundamentally, this implies the DUNE is not blind to CNO neutrinos, purely by design. One also sees the efficiency with collection-or-induction triggering is, overall, higher than collection plane only triggering. Logically, this makes sense; however, higher efficiency in triggering CNO neutrinos implies radiological backgrounds in the same energy regime

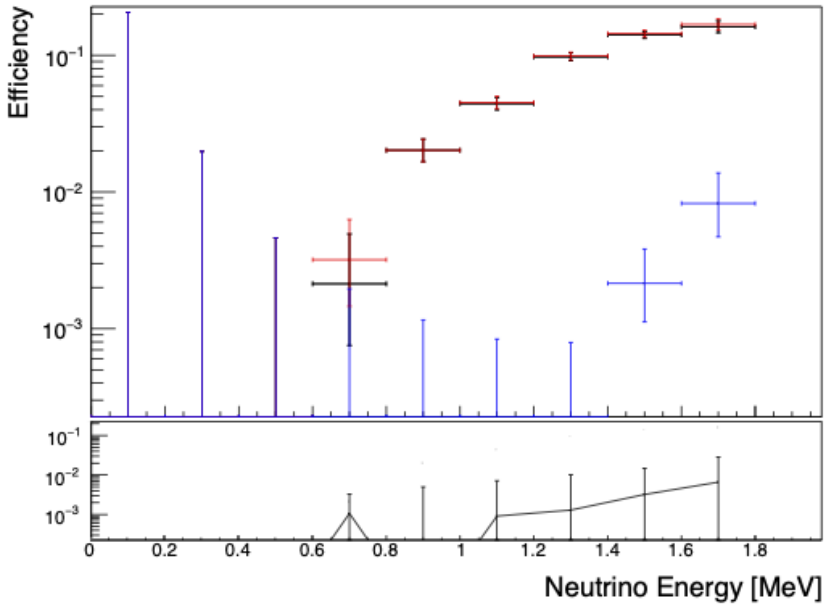

Figure 5.3: The efficiency curves for three different trigger models tested in DUNE CNO neutrino studies. The black, red and blue points represent the collection plane only, collection-or-induction plane, and collection-and-induction plane trigger models, respectively. The subplot represents the difference between collection only and collection or induction triggering.

also pass the trigger criteria. The extent to which this occurs requires evaluation, as a higher signal at the cost of a significantly higher background may limit DUNE's capabilities regarding CNO neutrinos. Lastly, the collection-and-induction plane triggering model has the lowest efficiency. This model only becomes sensitive at the upper end of the energy range. Under these conditions, the ^{13}N neutrinos would be invisible to DUNE. However, this trigger model would likely reduce the radiological background rate.

5.3 Event rates in DUNE

Hereon, all predictions concerning event rates come from collection-and-induction plane triggering. Results from conventional and collection-or-induction plane triggering are not discussed in detail, as the background event rates exceeded the square of the CNO rate.

5.3.1 Solar Neutrino Interaction Rate in DUNE

Calculating the solar neutrino interaction rate for DUNE simulations is a multi-step process. As discussed, solar neutrinos get generated one at a time, so the event window used in the simulation does not reflect real-time neutrino interactions.

Fortunately, estimating the number of interactions is straightforward. The general equation is:

$$N_{\text{int. pred.}} = \mathcal{D}\phi_\nu E_{\text{trig.}}\sigma_{\nu,e}P_{\text{MSW}}. \tag{5.2}$$

ϕ_ν represents the flux of a given neutrino from the CNO cycle; spectra taken from [130], and total fluxes taken from Table 6 of [135]. E_{trig} is the trigger efficiency for a given trigger model, and $\sigma_{\nu,e}$ is the ES cross-section from `MARLEY` (see 7.4.2 of [136]). P_{MSW} is the averaged day-night Mikheyev–Smirnov–Wolfenstein survival probability, taken from [130]. $\mathcal{D}$ represents a detector constant that encodes how long a given exposure on the detector is and the number of target particles with units Hz per nucleus. The exposure time is variable; however, the number of target particles gets defined to be constant, reflecting the number of argon atoms in 10-ktonne of liquid argon.

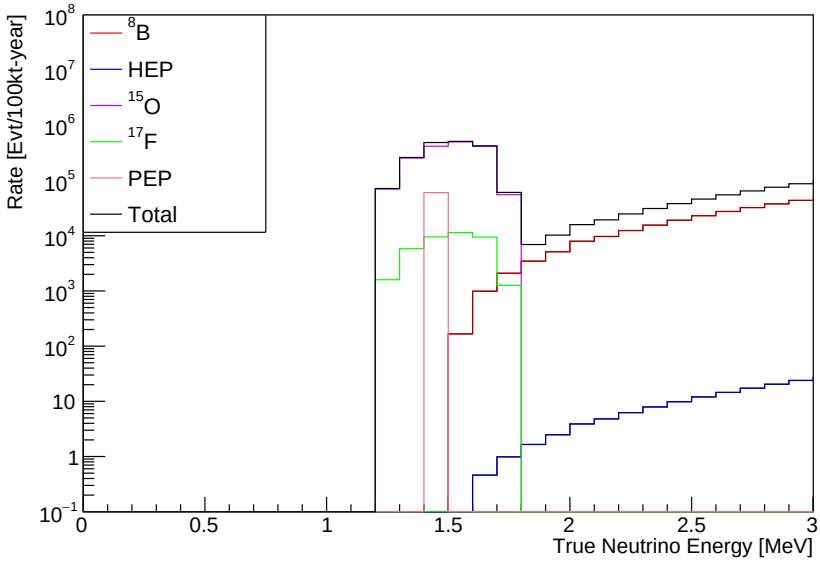

Figure 5.4: The predicted triggered event rate for solar neutrinos at DUNE in 100 keV bins for a 100 ktonne-year exposure. The purple and green lines represent the ^{15}O and ^{17}F CNO neutrino spectra respectively. The red, blue and pink lines represent the ^{8}B, HEP and *pep* neutrino spectra, respectively. Lastly, the black line is the total event rate of all solar neutrino spectra combined.

Figure 5.4 illustrates the predicted event rate for solar neutrinos at DUNE. The collection-and-induction plane trigger model was used to calculate the solar neutrino event rates. Therefore, there is a hard cutoff at 1.2 MeV in neutrino energy as there is zero trigger efficiency at that energy. By extension, the ^{13}N neutrinos are not present for the same reason.

One can examine different solar metallicity models under this procedure; this presents a great advantage to using this method. As nothing gets encoded into the simulations, one only has to change the flux of a given neutrino spectrum. At DUNE, one can expect the event rates given in Table 5.1.

	low metallicity	high metallicity
$^8B_{CC}$	1.57×10^7	1.95×10^7
$^8B_{ES}$	3.78×10^7	4.86×10^6
HEP_{CC}	7.70×10^4	9.31×10^4
HEP_{ES}	9.68×10^4	1.17×10^4
pep	6.05×10^4	6.22×10^4
^{13}N	0	0
^{15}O	1.37×10^5	2.44×10^5
^{17}F	3.13×10^3	6.34×10^3

Table 5.1: The predicted event rates for ^{8}B, HEP, *pep* and CNO neutrinos at DUNE. The values given represent a 1-year exposure on a 10-ktonne fiducial volume or 10 ktonne-year. For comparison, low and high metallicity models get calculated separately. The associated uncertainties are statistical.

5.3.2 Background Rates

Compared to calculating the solar neutrino event rates in DUNE simulations, the radiological background rate is simple to calculate. Every background simulation ran for exactly 10,000 events. These many events provide enough statistics to evaluate event rates but aren't so many that the computational cost is too high. Because background simulation events have a time window of 4.492 ms, the total simulated time for each background is 44.92 s. Therefore, one must only count the number of clusters that pass the trigger requirements, discern the event type that generated it, and keep a record over the 10,000 events. Finally, using this many events means the background rate is calculable with 1% associated uncertainty.

The collection-and-induction plane trigger model has the benefit of actively discriminating against particular radiological backgrounds. Chiefly, under this trigger model, the ^{39}Ar is entirely mitigated. Intuitively, this is reasonable as the maximum charge

deposition of an ^{39}Ar decay is 600 keV. From Figure 5.3, we see that this trigger model is effectively blind to events of such low energy. Furthermore, two ^{39}Ar decays coincident in time and space would still struggle to pass the triggering conditions. Fortunate as this is, it does not eliminate ^{39}Ar charge depositions from being clustered into those from separate decays.

Additionally, in 10,000 events under collection-and-induction plane triggering, there was no record of ^{60}Co or ^{40}K clusters passing the trigger conditions appeared. One can rationalise this absence with two arguments. First, the energy depositions of ^{60}Co and ^{40}K are barely above the "turn-on" point of this trigger model's efficiency curve. We know, due to electron recombination, that not all of a decay's ionisation gets collected on the APAs. Therefore, it becomes unlikely that a cluster from these sources would pass the triggering conditions. Secondly, the number of decays simulated is proportional to the decay rate and the size of the volume from which the nuclear decays originate. Because the volume of the CPA and APA volumes in the geometry are small compared to, for example, the liquid argon, the number of nuclear decays occurring is, by extension, also small. Ultimately, the low probability of passing the trigger thresholds and the low production rate results in no triggering clusters in a sample of 10,000 events.

The event rates for the radiological backgrounds that pass the triggering conditions are the following.

Radiological background	Rate [events / 10-ktonne second]
^{42}Ar	26.7
Neutrons	0.54
^{222}Rn	41.98

Table 5.2: The event rates of the radiological backgrounds that pass the trigger conditions.

5.3.3 Neutrino energy reconstruction

The detector is physics agnostic to all clusters that pass the trigger conditions. We know CNO neutrinos only appear in a finite energy range; therefore, it follows that reconstructing the neutrino energy from the charge depositions is necessary. For high-energy events, this task is more straightforward. One can assess the total charge deposited, examine the topology of any tracks and showers and reconstruct a neutrino's energy with excellent accuracy. For low-energy events, where we have neither tracks nor showers, we have only a handful of hits to analyse.

Machine learning (ML) is a helpful tool for this problem. One can produce arbitrarily many neutrino events and feed the cluster information and true-neutrino energies into a machine learning algorithm. Over time, the ML algorithm can, in principle, learn to predict the neutrino energy accurately given cluster parameters.

Numerous ML predictors are available. Popular prediction models include:

- neural networks that imitate the networks of biological neurons in brains [137],
- decision trees that start with a single input node and ask a series of "if this then this otherwise that" questions,

- ensembles of decision trees called a random forest that works to output an agreed, most likely prediction between all trees.

The classifiers described above can yield good results but are also cumbersome to implement. Instead, a linear regression model was used to reconstruct neutrino energy from charge deposition clusters. Linear regression models are similar to polynomial fitting. Polynomial fitting takes a collection of points on a 2D plane and fits some function, $f(x)$, to those points while attempting to maximise the quality-of-fit by minimising the χ^2. A linear regression model does the same but in n-dimensional space.

The inputs into a linear regression model require consideration. There is no use in supplying the model with redundant variables as this will impact its training and, ultimately, its predictive power. Here, a redundant variable means one that has little or no impact or variation between data. For example, suppose the direction of every cluster was travelling in the positive x-direction. Giving an ML prediction model this information is as relevant as not giving it this information. Other inputs to avoid are those that vary but are not relevant to the prediction. An example would be the APA number on which the charge gets collected. One assumes that two identical clusters occurring on different APAs have the same neutrino energy and that APA_n is not functionally dissimilar to APA_m.

With these considerations, the following variables get given to the linear regression model:

- the number of hits in the cluster,

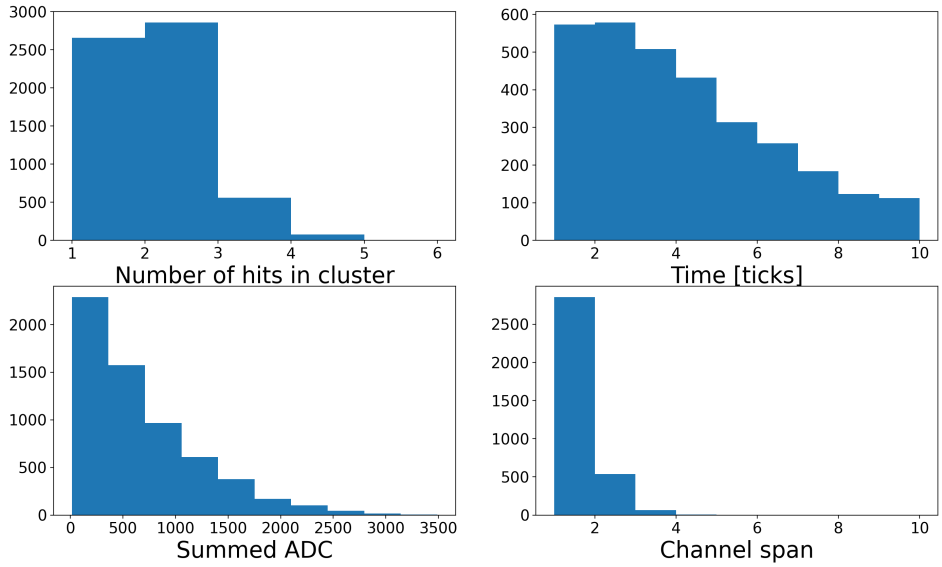

Figure 5.5: The distribution of the input variables to the linear regression model responsible for reconstructing neutrino energy.

- the time-span of the cluster, loosely representing the cluster's dimension along the drift axis,
- the channel-span of the cluster, representing the cluster's dimension along the beam axis,
- the summed ADC of the hits within the cluster.

Figure 5.5 shows the distributions of each variable used as input.

In total, 6,160 low-energy neutrino events served as the training set for the linear regression model. The input energies range from 1-5 MeV. The radiological backgrounds often have energies above that of CNO neutrinos. Therefore, the input energy range for the ML model is defined to reflect that and, hopefully, give the

model better accuracy over a range of energies - not singularly targetting CNO neutrinos. The test dataset is a further ∼4,000 low-energy events. Figure 5.6 shows the actual and reconstructed neutrino energies on the x- and y-axes, respectively. We see that the average of the histogram (the red-dashed line) closely follows a $y = x$ profile, implying, on average, that the energy reconstruction is working. The solid-red lines enclosing the red-shaded region represent one standard deviation from the mean. We see that the energy gets significantly smeared upon reconstruction, despite being centred on the true-energy value. The extent of the smearing varies with neutrino energy, which one can examine by testing the reconstruction quality in various bins of neutrino energy. The subplots in Figure 5.7 show the distribution of reconstructed energy values around the true neutrino energy. The vertical orange lines denotes the true neutrino energy sampled, and the green profiles show the best Gaussian fit to the distribution of reconstructed energy values. As noted from the 2D histogram, the mean of the Gaussian fits agree, in general, with the position of the sampled neutrino energy, validating that the ML model is reconstructing the neutrino energy to some accuracy. The parameters of the Gaussians allow one to calculate the resolution of the model's energy reconstruction. For a Gaussian distribution of the form,

$$\mathcal{G}(x : \mu, \sigma, A) = \frac{A}{\sigma\sqrt{2\pi}} e^{-\frac{(x-\mu)^2}{2\sigma^2}}, \tag{5.3}$$

the full width at half maximum is,

$$\text{FWHM} = 2\sqrt{2\ln 2}\sigma \approx 2.355\sigma. \tag{5.4}$$

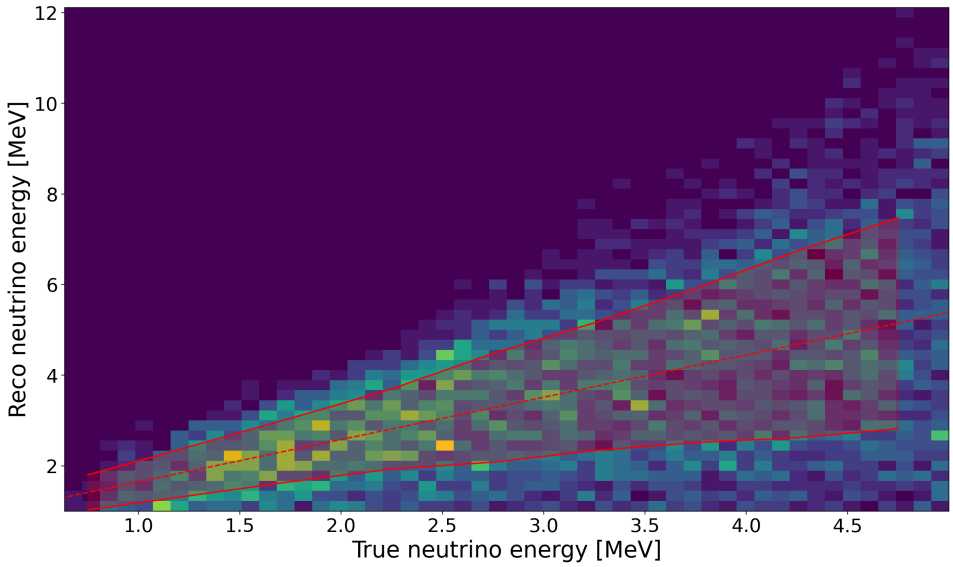

Figure 5.6: Neutrino energies before and after reconstruction. The dashed red line shows the distribution's average, and the two solid red lines enclosing the red-shaded region represent one standard deviation from the mean.

The resolution at a given energy is defined as

$$\phi = \text{FWHM}/E_{\mu}. \tag{5.5}$$

Applying Equation 5.5 to each bin of Figure 5.7 yields an average resolution of 56% across the energy range considered. Since DUNE's design did not aim to probe the 1-5 MeV region with any specificity, a better than 100% resolution is remarkable. For a feasibility study, using less optimised energy reconstruction still allows for making inferences. The same would not be permissible for analysing DUNE data. In that case, energy reconstruction would require a significantly more precise evaluation.

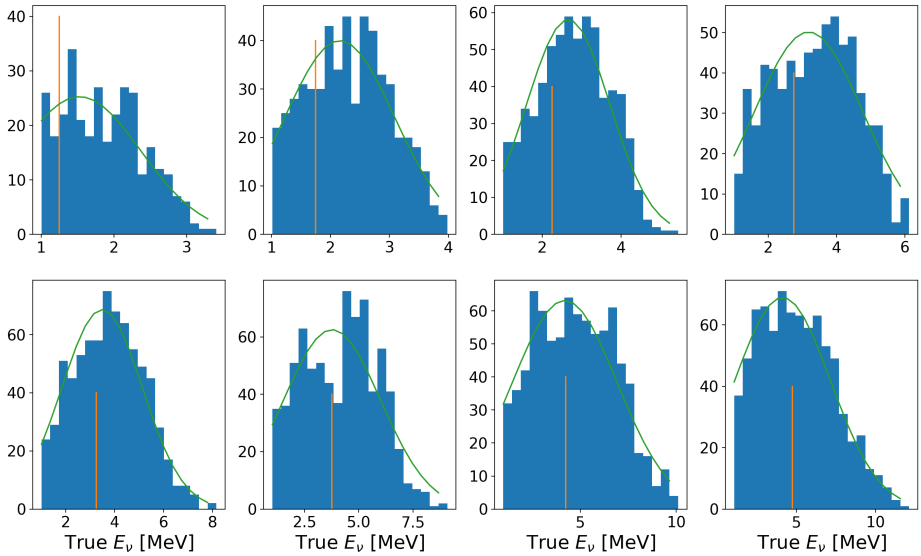

Figure 5.7: Banded samples of the quality of energy reconstruction evaluated in distinct energy values. The vertical orange lines represent the specific neutrino energy sampled. The blue histogram shows the distribution of reconstructed neutrino energy for events of the specified energy, and the green profile is the gaussian best fit.

A noteworthy observation on the energy reconstruction is that, despite smearing, neutrinos with energies at the upper end of the CNO spectrum do not get reconstructed above 5 MeV. Knowing that a CNO neutrino's reconstructed energy does not exceed 5 MeV means one can define a CNO "region-of-interest", or ROI, of 0-5 MeV (reconstructed). By extension, one can probe outside this ROI to examine other physics phenomena, excluding CNO neutrinos as a background

5.3.4 Events rates after energy reconstruction

With a reconstruction algorithm, one can take hit clusters of any kind - background or signal - and reconstruct 'neutrino' energy. Following this, individual spectra for each physics process get produced, ultimately serving as inputs to an overarching solar neutrino analysis. Utilising reconstructed energy spectra is crucial as it more closely mimics the information one can expect from the DUNE detectors.

Reconstructed CNO neutrino spectra

As before, ^{13}N neutrinos are too low-energy to pass the triggering criteria. Figure 5.8 shows the ^{15}O (blue), ^{17}F (orange) and total CNO spectrum (green) after energy reconstruction for an exposure of 10 ktonne-years. As the rate of the ^{15}O neutrinos is two orders of magnitude higher than that of the ^{17}F neutrinos, the total CNO spectrum appears barely over the ^{15}O reconstructed energy spectrum.

Reconstructed ^{8}B, HEP and *pep* neutrinos and radiological backgrounds

Of the radiological backgrounds, ^{42}Ar and ^{222}Rn dominate, as implied from Subsection 5.3.2. As before, the energy values get smeared for all spectra; however, the general forms remain consistent with the original inputs. Observing the reconstructed ^{42}Ar profile (the green line of Figure 5.9), we see the beta profile expected of this nuclear decay but stretched along the x-axis. The ^{222}Rn and neutron background spectra are approximately flat along the energy domain, with radon posing as the dominant radiological background.

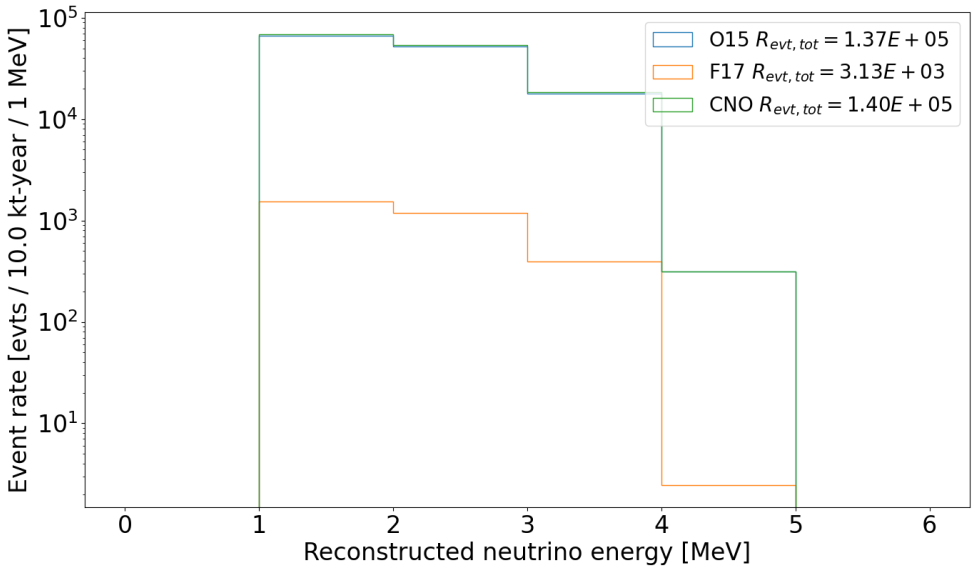

Figure 5.8: The reconstructed energy spectra of CNO neutrinos for a 10 ktonne-year exposure. A low solar metallicity model informed the event rate calculations.

The ^{8}B and HEP spectra, after undergoing energy reconstruction, similarly imitate the original flux spectra. The *pep* neutrinos get noticably smeared following the energy reconstruction. Prevalent, mainly in the ^{8}B event rate, at higher energies, the energy reconstruction fails, breaking the expected smooth spectrum. One expects this particular reconstruction approach to fail at higher energies. The linear regression model used was trained on 1-5 MeV events. Therefore, at higher energies, it attempts to perform accurate reconstruction but has no prior knowledge on how to do so. Ultimately, this poses no issue, as in our region of interest - events of $\mathcal{O}(1)$ MeV - are reconstructed to the same quality as the CNO events of Subsection 5.3.4.

Separating the five main signals: CNO neutrinos, ^{8}B neutrinos, HEP neutrinos, *pep* neutrinos and radiological backgrounds, one can form an expectation event rate spectrum. Figure 5.11 shows such a spectrum. The radiological backgrounds dominate

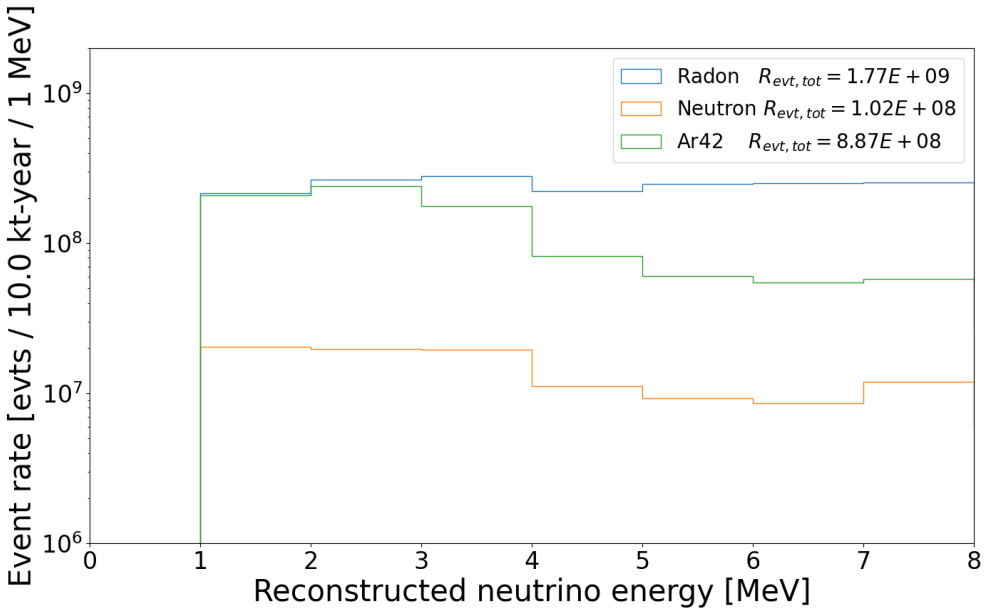

Figure 5.9: The radiological background event rate after applying energy reconstruction for an exposure of 10 ktonne-years.

the event rate, with any given bin approximately three orders of magnitude above the next-to-leading spectrum. The lilac line marked "Backgrounds" represents the combination of radiological backgrounds, HEP and ^{8}B neutrinos. The orange "Radiological", lilac "backgrounds" and brown "All Signal" lines in Figure 5.11 appear to overlap because the radiological backgrounds completely dominate the event spectrum.

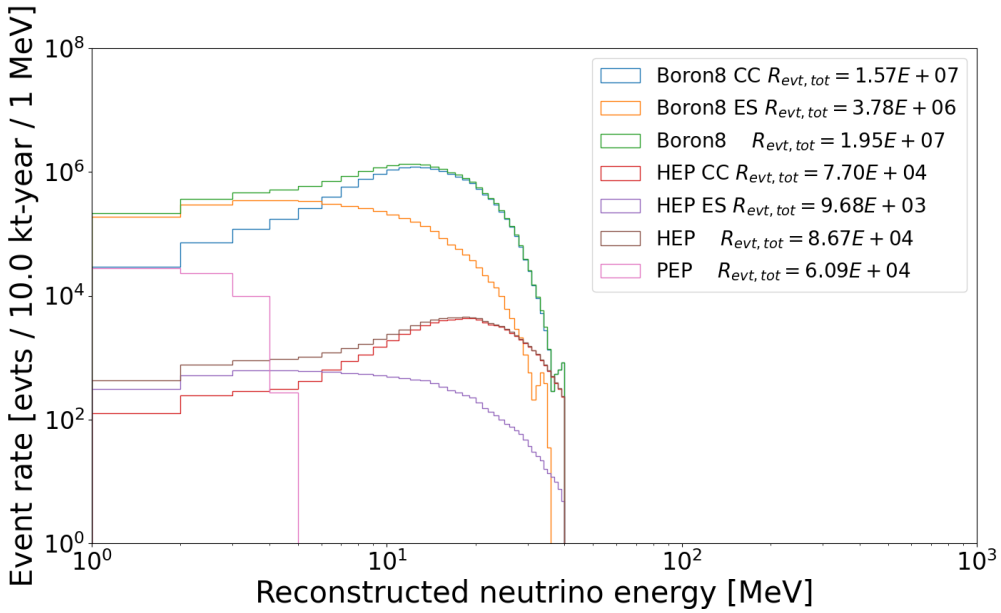

Figure 5.10: The ^{8}B, HEP and *pep* event rates after applying energy reconstruction for an exposure of 10 ktonne-years.

5.4 CNO neutrino rate and uncertainties at DUNE

5.4.1 The counting experiment procedure

In a counting experiment, one evaluates the total number of events within an ROI and successively subtracts backgrounds based on predictions from one's underlying physics model. Counting experiments rely on realistic modelling of the backgrounds. Ideally, one would be able to measure individual background components; however, when this is not available, accurate simulations are crucial.

A counting experiment can be generalised as the following:

$$R_{\text{target}} = \frac{1}{\varepsilon_{\text{target}}} \left(r_{\text{total}} - \sum \varepsilon_n \tilde{r}_n - \tilde{r}_o \right), \tag{5.6}$$

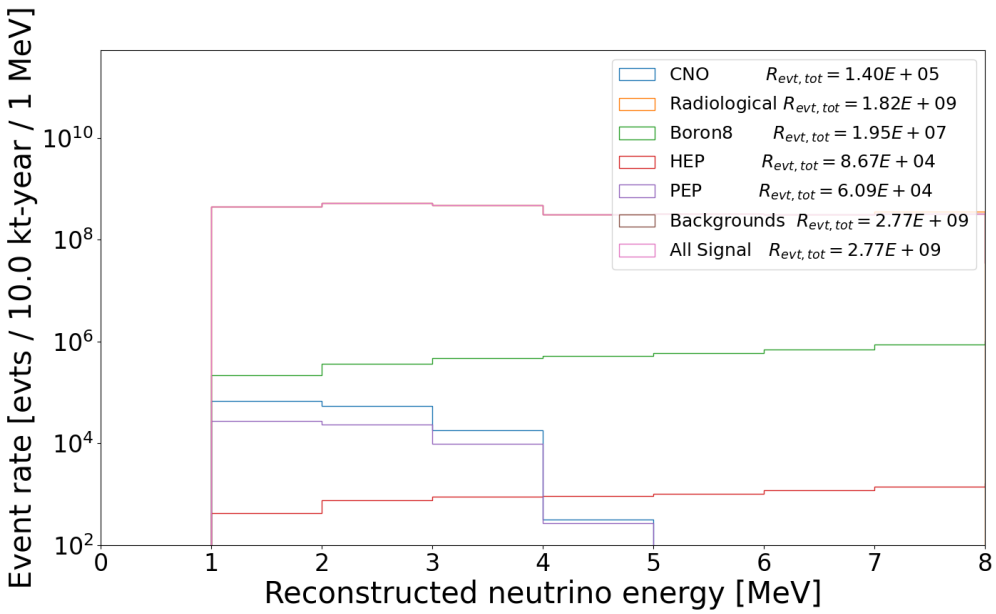

Figure 5.11: The total event rate spectrum after applying energy reconstruction for an exposure of 10 ktonne-years.

$$\sigma_{\text{target}} = \frac{1}{\varepsilon_{\text{target}}} \left(\sigma_{\text{total}} \oplus \sigma_o \oplus \sigma_i \oplus \sigma_j \oplus \cdots \right). \tag{5.7}$$

Here, R_{target} is the event rate of the physics process in question. r_{total} is the total event rate, $\tilde{r}_n$ is the event rate of the n-th background in the ROI. $\tilde{r}_o$ is the event rate of the background components not determined by simulation Lastly, ε is the fraction of events of a given process within the ROI. In Equation 5.7, $\sigma_{i,j,\ldots}$ is the uncertainty of a given physics process and $x \oplus y \equiv \sqrt{x^2 + y^2}$. The combination of uncertainties in this manner assumes the individual errors are Gaussian.

For evaluating the CNO rate at DUNE, Equations 5.6 and 5.7 would become

$$R_{\text{CNO}} = \frac{1}{\varepsilon_{\text{CNO}}} \left(r_{\text{total}} - \varepsilon_{^8\text{B}} \tilde{r}_{^8\text{B}} - \varepsilon_{\text{HEP}} \tilde{r}_{\text{HEP}} - \varepsilon_{pep} \tilde{r}_{pep} - \varepsilon_{^{222}\text{Rn}} \tilde{r}_{^{222}\text{Rn}} - \varepsilon_{^{42}\text{Ar}} \tilde{r}_{^{42}\text{Ar}} - \varepsilon_{\text{n}} \tilde{r}_{\text{n}} \right), \tag{5.8}$$

$$\sigma_{\mathrm{CNO}} = \frac{1}{\varepsilon_{\mathrm{CNO}}} \left(\sigma_{^8\mathrm{B}} \oplus \sigma_{\mathrm{HEP}} \oplus \sigma_{pep} \oplus \sigma_{^{222}\mathrm{Rn}} \oplus \sigma_{^{42}\mathrm{Ar}} \oplus \sigma_{\mathrm{n}} \right), \tag{5.9}$$

where $\tilde{r}_{\mathrm{n}}$, ε_{n} and σ_{n} now return to the event rate, fraction of events and uncertainty on neutrons.

5.4.2 Systematic uncertainties in CNO counting experiment

Evaluating σ_{CNO} from Equation 5.9 requires careful consideration of the uncertainties included. Numerous stages lead to the final value of any given event rate, and at each step, several uncertainties emerge. The systematic uncertainties discussed hereon directly impact the error on the CNO neutrino rate under a counting experiment paradigm. Other systematics may be relevant; therefore, this is not an exhaustive list.

Uncertainties on solar neutrino fluxes

The uncertainties on the ^{8}B, HEP and *pep* neutrino fluxes used are 4% [138], 30% [135] and 1% [135], respectively. The ^{8}B uncertainty comes from the SNO collaboration's combined fit of their three phases of data taking. The HEP and *pep* uncertainties are theoretical.

Uncertainties on radiological backgrounds

Applying uncertainty to the radiological backgrounds is difficult, as measurements from the detector aren't available. Therefore, one can either apply a reasonable approximation or use information gleaned from similar experiments.

One such radiological background where relevant information is available is ^{42}Ar. The DBA experiment [139] - a double beta-decay experiment using a liquid argon TPC detector - provided data from which the ^{42}Ar concentration in atmospheric argon was calculable. In total the ^{42}Ar concentration in atmospheric argon is $9.2^{+2.2}_{-4.6} \times 10^{-21}$ atoms per atom of ^{40}Ar, corresponding to an activity of 92^{+22}_{-46} μBq/kg [119]. The calculated activity informed the ^{42}Ar simulations; therefore, a 50% uncertainty gets associated with its production rate as a worst-case-scenario.

There are difficulties in assigning uncertainty to radiological neutrons. As discussed, neutrons enter the liquid argon from as far out as the cavern rock and as internally as the cold steel membrane. `LArSoft` simulations approximate neutron production from multiple sources using five representative panels around the workspace geometry. The neutron production rate gets informed by large-scale simulations in the 10-ktonne geometry. Until accurate measurements in the detector cavern get performed, one must estimate the uncertainty given the production spectra and statistical information. Under these considerations, a 20% uncertainty is associated with radiological neutrons [140].

No measurement of the ^{222}Rn contamination in the DUNE detector is available. Therefore, simulations get driven by a requirement set on the radon activity. Currently, the standard radon level requirement is 1 mBq/kg. This value ensures that in the event the ^{238}U chain is in perfect secular equilibrium, the induced rates are still one order of magnitude below the ^{39}Ar rate [141]. As a place-holder, until more accurate measurements are available, a general uncertainty on the radon rate gets set to 20%. As the radon background has the highest rate, it is imperative this value gets specified in the future.

Model specific systematic uncertainties

All interactions simulated carry an uncertainty based on the trigger model used. Similarly, uncertainty in the energy reconstruction applies to all signals. Specifically to solar neutrino signals, one must also consider a cross-section uncertainty[5] and uncertainty in the survival probability.

The uncertainty on the energy reconstruction is, as previously mentioned, 56%. Calculating the triggering efficiency involved the examination of 10^4 low-energy neutrino events. Based on simulation statistics, a 1% triggering efficiency systematic uncertainty is applied. Such a low value is not impossible, as DUNE physics goals include SNB detection, implying a complete knowledge of the trigger model during run-time.

The electron-neutrino elastic scattering cross-section is known with sub-percent precision [45]. Unfortunately, the charge current interaction cross-section is less tightly constrained, with literature suggesting an optimistic uncertainty of $\lesssim 10\%$ [19]. The charge-current cross-section uncertainty is likely to be higher. Direct observation is required to ascertain a more robust value of the cross-section uncertainty.

The timescale of the exposures is assumed to be of order ktonne-year, not ktonne-hour. However, as the Earth rotates, solar neutrinos travel through varying thicknesses of Earth before reaching the detector. Ultimately, this affects the electron neutrino survival probability depending on the time of day. Accounting for this, the averaged day-night MSW survival probability gets implemented. Figure 5.12 shows the day, night and average MSW survival probabilities for solar neutrinos. The separation between the day and night spectra becomes substantial at energies above

[5]For the CNO ROI, the interactions are all considered strictly elastic scattering.

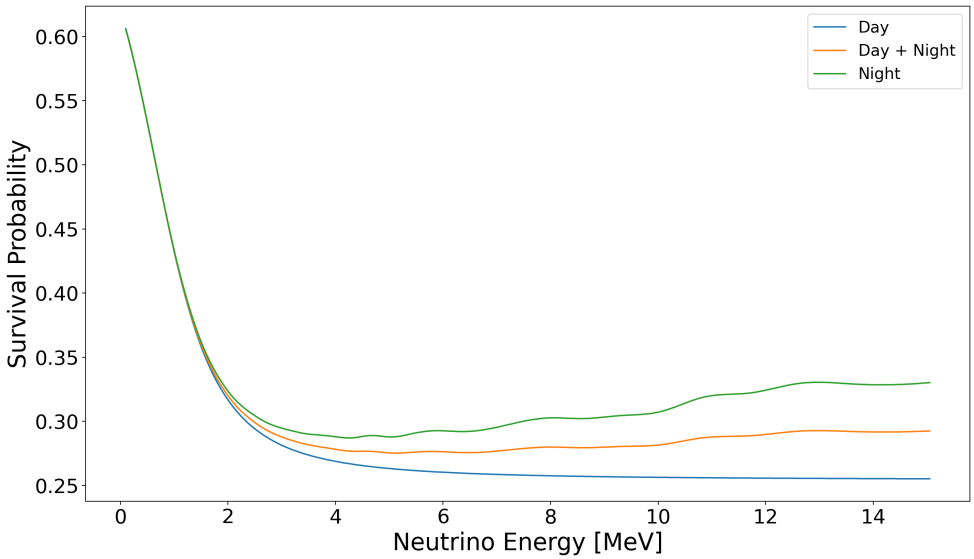

Figure 5.12: The day, night and averaged Mikheyev–Smirnov–Wolfenstein survival probability as a function of neutrino energy, taken from [21].

5 MeV. Therefore, fluxes such as ^{8}B and HEP neutrinos are much more likely to be affected by the day-night asymmetry. An uncertainty on the MSW survival probability was determined by evaluating the average difference between the mean value and the day and night values. Calculating these ratios along the complete energy regime yields a general uncertainty of 2%.

Summary of systematic uncertainties

Table 5.3 catalogues the systematic uncertainties in the CNO rate counting experiment. As mentioned, this should not be considered an exhaustive list of systematic uncertainties. Instead, it is a collection of the dominant uncertainties. Reconsideration of the list and the values will be required once DUNE is operational.

Description	Percentage uncertainty
^{8}B neutrino flux	4% [138]
HEP neutrino flux	30% [135]
pep neutrino flux	1% [135]
Radiological ^{42}Ar activity	+24%/-50% [119]
Radiological neutron activity	20% [140]
Radiological ^{222}Rn activity	20% (assumed)
MSW survival probability	2%
Trigger efficiency	1%
Energy reconstruction	56%
Elastic scattering cross section	0.5% [45]
Charge current cross section	10% [19]

Table 5.3: Table showing the percentage uncertainties on CNO interaction rate calculation elements. Values above the central line are specific to individual components. Values below the central line pertain to neutrino and background events.

One can combine the uncertainties in Table 5.3 to evaluate the total percentage uncertainties of each element contribution to the CNO rate in Equation 5.9.

Description	Percentage uncertainty
$\sigma_{^{8}\mathrm{B}}$	57%
σ_{HEP}	64%
σ_{pep}	57%
$\sigma_{^{42}\mathrm{Ar}}$	61%
σ_{n}	59%
$\sigma_{^{222}\mathrm{Rn}}$	59%

Table 5.4: Table showing the percentage uncertainty of each element in the CNO rate uncertainty.

Table 5.6 show each element's uncertainty is around 60%. HEP neutrinos carry the highest uncertainty due to their significant flux uncertainty. Fortunately, the HEP neutrino interaction rate is significantly lower than all other sources and, in turn, poses little issue. The same is not applicable for the other backgrounds, whose rates will contribute substantially to the CNO rate uncertainty.

5.4.3 Evaluating the CNO rate

The values of ε and $\tilde{r}$ of Equation 5.8 are trivially extractable given we're using simulated data. Therefore, any rate values calculated will return the value inputted into the simulation. However, the uncertainties calculated do carry relevance.

A region-of-interest between 1-4 MeV reconstructed neutrino energy gets defined as the principle search region. Within the bounds of the ROI, the number of events gets counted for each signal - signal here refers to radiological backgrounds and solar neutrinos. At the same time, the total integrated rate of each signal gets calculated over their complete energy domain. With the total rate, R_{tot}, and the rate within the ROI, $\tilde{r}$, evaluated, the ε values are

$$\varepsilon = \tilde{r}/R_{\text{tot}}. \tag{5.10}$$

Executing Equations 5.8 and 5.9 yields

$$R_{\text{CNO, HZ}} = 2.50 \pm 0.01(\text{stat.})^{+5.94\times10^{3}}_{-6.54\times10^{3}}(\text{syst.})\ [10^5\ \text{evts / 10 ktonne-year}]$$

$$R_{\text{CNO, LZ}} = 1.40 \pm 0.004(\text{stat.})^{+5.94\times10^{3}}_{-6.54\times10^{3}}(\text{syst.})\ [10^5\ \text{evts / 10 ktonne-year}]$$

As expected, the rate value calculated for both metallicities corresponds to the values in Table 5.1. The statistical uncertainties indicate no limitation by the number of events analysed. Ultimately, systematics dominate the measurement with the systematic uncertainty approximately three orders of magnitude greater than the measurement. One can deconstruct the systematic uncertainty calculation and evaluate the leading contributors to the uncertainty value. As intuitively expected, the radiological backgrounds, with their high rates and associated percentage uncertainties, drive the high uncertainty value. These values are:

$$\sigma_{^{42}\mathrm{Ar}} = 3.81 \times 10^{8} \text{ [evts / 10 ktonne-year]},$$
$$\sigma_{\mathrm{neutron}} = 3.55 \times 10^{7} \text{ [evts / 10 ktonne-year]},$$
$$\sigma_{^{222}\mathrm{Rn}} = 4.53 \times 10^{8} \text{ [evts / 10 ktonne-year]}.$$

Under the conditions described, relating to a standard DUNE far detector module, it is unlikely that DUNE can make a conclusive measurement of the CNO flux. The systematic uncertainties, dominated by the radiological backgrounds, are too high for the CNO event rate to emerge. Despite the limitations, one can postulate the conditions required for DUNE to measure the CNO flux. A detector module, such as the low-background module of opportunity, which proposes $\mathcal{O}(10^3)$ background reduction on radon, and potentially more on argon and neutrons will help the radiologically dominated systematic uncertainty. Furthermore, one can examine reasonable improvements to the intrinsic systematic uncertainties.

5.4.4 Uncertainty on CNO rate in the low-background module of opportunity

The DUNE low-background module of opportunity [18] aims to reduce the radiological backgrounds significantly. It predicts a reduction in the radon rate of approximately three orders of magnitude (see Subsection 3.2.5). Additionally, it predicts further reductions in the ^{42}Ar rate by using underground argon (UAr) as the detector medium instead of atmospheric argon (AAr). Finally, the low-background module has water shielding, effectively mitigating external neutrons entirely. The neutron background is practically insignificant if only internal neutrons contribute.

Quantifying the effect of strictly reducing the backgrounds is imperative to CNO studies. The radiological event rates undergo incremental reductions until they reach one thousandth their initial values. All radiological backgrounds are decreased following the radon reduction to emulate a "worst-case scenario" for background reduction. At each stage, the CNO percentage uncertainty gets evaluated under the systematic uncertainties in Table 5.3. Figure 5.13 illustrates the uncertainty of the CNO rate as a function of radiological background reduction.

From 0 - 100x reduction, the percentage uncertainty decreases exponentially. After that, the uncertainty plateaus as $\sigma_{\mathrm{CNO}} \approx 160\%$. This plateau indicates that after a 100x reduction, the radiological backgrounds are not the leading contributor to the CNO rate uncertainty. Instead, ^{8}B neutrinos become the leading background. Since one cannot shield the detector from neutrinos, the ^{8}B background is the limiting background in a low-background neutrino detector.

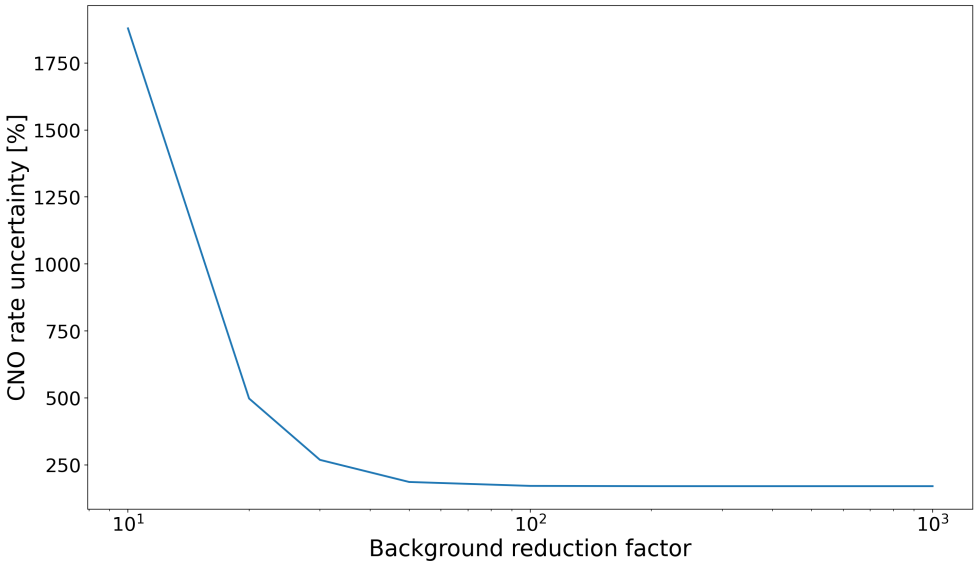

Figure 5.13: The CNO percentage uncertainty as a function of radiological background reduction.

5.4.5 Uncertainty on CNO rate with improved systematics

Tables 5.3 and 5.6 show systematic uncertainties that impact the measurement of CNO neutrinos at DUNE. At the current magnitudes of these uncertainties, it is unlikely that DUNE can make a convincing measurement. However, over DUNE's operational lifetime, the magnitude of the uncertainties is likely to decrease. The extent of this reduction is currently unknown, but in place of experimentally driven values, one can postulate reasonable improvements to these systematics.

The first improvements to consider are the uncertainties on the radiological background activities. ^{42}Ar's uncertainty is of the order $\mathcal{O}(25-50\%)$, and ^{222}Rn and neutrons both carry a 20% associated uncertainty. Supposing DUNE can measure the ^{42}Ar content of atmospheric (or underground) argon to some arbitrary accuracy.

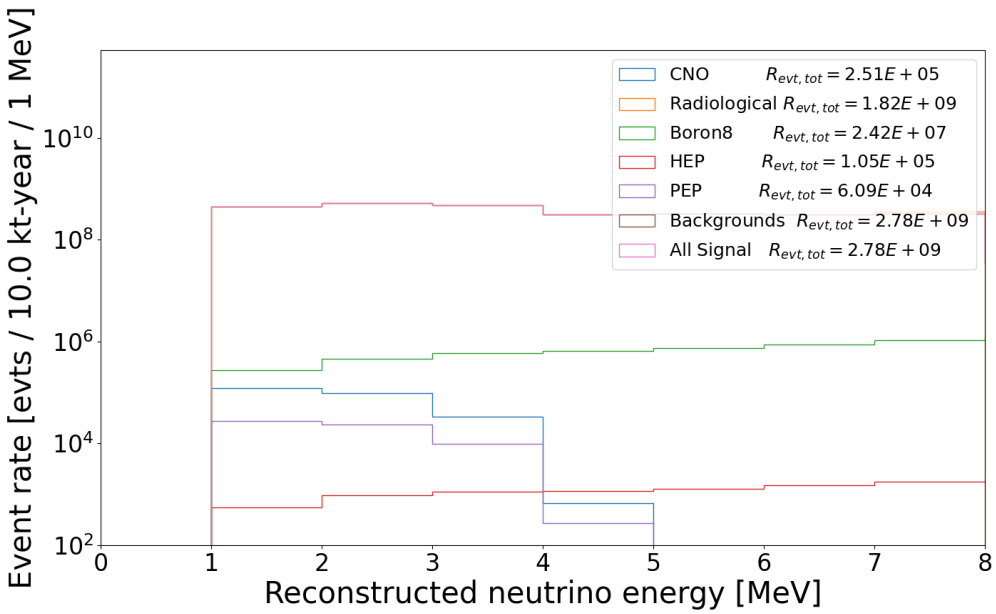

Figure 5.14: The event rate of all sources with no background reduction.

Similarly, one might assume an analogous measurement gets made on neutrons and ^{222}Rn. Then, we can temporarily set the activities of these sources in the analysis to an arbitrarily low value - in this case, $\sigma_{\text{radiological}} = 5\%$. An uncertainty of 5% is consistent with measurements performed at DarkSide-50 [104], a low-background dark matter experiment.

The next improvement for consideration is energy reconstruction. On average, the neutrino energy reconstruction algorithm has 56% resolution. Therefore, there is considerable scope for improvement. Despite the difficulties DUNE faces in the data acquisition of 1-5 MeV signals, some improvements are possible. One may struggle to acquire more hits than are available presently, but sophisticated use of optical flash matching could prove effective. Additionally, applying tools like PANDORA, a specialist reconstruction module, if tailored to low-energy events, would consid-

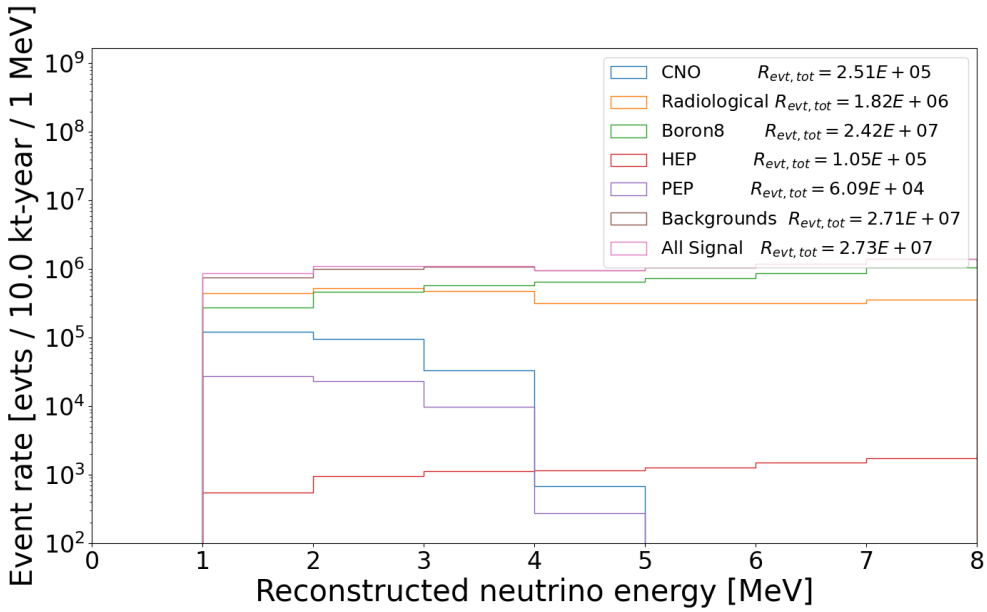

Figure 5.15: The event rate of all sources under a 1000x background reduction.

erably improve this uncertainty. PANDORA utilises advanced processes, such as pattern recognition and machine learning models, to reconstruct neutrino interactions. Currently, the lowest energy it reliably works at is of the order $\mathcal{O}(100$ MeV), significantly above the remit of solar neutrinos. Reconstruction of events with more charge depositions is possible with an efficiency of between $80 - 100\%$ [142]. Assuming improvements in the low energy sector towards a similar calibre of event reconstruction, one can optimistically achieve an energy resolution of 10% or less.

Description	Percentage uncertainty
^{8}B neutrino flux	4% [138]
HEP neutrino flux	30% [135]
pep neutrino flux	1% [135]
Radiological ^{42}Ar activity	5%
Radiological neutron activity	5%
Radiological ^{222}Rn activity	5%
MSW survival probability	2%
Trigger efficiency	1%
Energy reconstruction	56%
Elastic scattering cross section	0.5% [45]
Charge current cross section	10% [19]

Table 5.5: Table showing the percentage uncertainties on CNO interaction rate calculation elements with tightened systematics.

Description	Percentage uncertainty
$\sigma_{^{8}\mathrm{B}}$	12%
σ_{HEP}	31%
σ_{pep}	11%
$\sigma_{^{42}\mathrm{Ar}}$	9%
σ_{n}	9%
$\sigma_{^{222}\mathrm{Rn}}$	9%

Table 5.6: Table showing the percentage uncertainty of each element in the CNO rate uncertainty under tightened systematics.

In this case, one only needs to calculate the CNO uncertainty once. Solar metallicity has a negligible impact on ^{8}B, HEP and *pep* neutrino fluxes. Furthermore, solar metallicity does not affect the radiological backgrounds at the DUNE far detector. Ultimately, under the tightened systematics, the uncertainty on the CNO rate is $\sigma_{\text{tighter syst}} = 7.06 \times 10^{7}$ [evts / 10 ktonne-year].

The uncertainty with better systematics is only one order of magnitude lower than the equivalent value under standard uncertainties. Therefore, it remains unlikely that DUNE can make a convincing measurement of the CNO neutrino flux under this paradigm. It is clear that reducing the radiological background or tightening the systematics is not enough. Instead, examining the extent of the reduction to the CNO rate's uncertainty when enacting both methods is the channel to follow.

5.4.6 Uncertainty on CNO rate with improved systematics with low radiological backgrounds

Following on from the observations in Subsections 5.4.4 and 5.4.5, one can examine the effect of reducing the radiological backgrounds and tightening the systematic uncertainties. One can approximate the radiological background reduction as a 10^3 reduction across leading radiological contributors. If the backgrounds get reduced to this extent, and the percentage uncertainty on them is $\sim$9%, one can estimate that significant reductions to the CNO uncertainty should arise.

Upon re-executing the counting experiment, one can observe the effects of a lower radiological background in combination with the prospective better uncertainties. In this case, it is more descriptive to quote uncertainties as a percentage of the measured value. For low and high solar metallicities, the uncertainty on the CNO rate is 68% and 43%, respectively. Fortunately, the uncertainties on the CNO rate are now less than the measured CNO rate. Therefore, a measurement made under this paradigm is no longer consistent with zero.

An observation of the rates and uncertainties of the background components shows the main contributors to the CNO uncertainty. Table 5.7 shows that the dominant background is the ^{8}B, with ^{222}Rn and ^{42}Ar as the next-to-leading backgrounds. With this observation, one might consider management techniques on ^{8}B solar neutrinos. Blocking them is not possible. Even if shielding neutrinos were theoretically possible, it would mitigate CNO neutrinos simultaneously, making a challenging search all the more difficult. Instead, one might perform a more accurate measurement of the ^{8}B flux, minimising its uncertainty and, in turn, reducing the CNO measurement's uncertainty. One might also argue that further reductions to the radiological backgrounds are beneficial. While this is true, background reductions exceeding those predicted are unlikely and, if possible, impractical.

Source	Rate [evts / 10 ktonne-year]
^{8}B	$(1.38 \pm 0.16) \times 10^{6}$
HEP	$(2.74 \pm 0.55) \times 10^{3}$
pep	$(6.09 \pm 0.67) \times 10^{4}$
^{42}Ar	$(6.26 \pm 0.45) \times 10^{5}$
Neutrons	$(5.97 \pm 0.43) \times 10^{4}$
^{222}Rn	$(7.62 \pm 0.54) \times 10^{5}$

Table 5.7: Table showing the rates of the background components with low-background reduction and tightened systematics.

5.4.7 DUNE as a counting experiment for ^{8}B neutrinos

The counting rate procedure used to measure an excess of events due to CNO neutrinos has a general usage. In this case, one can define a new ROI, excluding any CNO events, and instead, target ^{8}B neutrinos. As before, the value of the counting experiment will return the input for the ^{8}B rate. The associated uncertainty, however, may be improved compared to the models used.

The counting experiment configuration utilises the maximal radiological background reduction predicted by the low-background module. Additionally, the tighter systematics, outlined in Table 5.5 get implemented in the ^{8}B counting experiment. The ROI gets defined as $E_{\nu,\text{reco}} = [5, 8]$ MeV. This ROI excludes all CNO events while including all other relevant physics processes. Figure 5.16 gives a representation of the ^{8}B counting experiment domain.

The counting experiment procedure gets applied to the event spectrum in the ROI, targeting ^{8}B neutrinos. The uncertainty on the ^{8}B neutrino rate, evaluated under Equation 5.7, is 1%. Propagating this uncertainty through the trigger, MSW survival rate, energy reconstruction and cross-section yields an uncertainty on the ^{8}B flux of approximately 7%. This uncertainty is almost twice that calculated in the SNO combined fit. Therefore, applying a similar counting experiment to the ^{8}B does not stand to offer any improvement on a CNO measurement at DUNE.

Despite not measuring the ^{8}B to greater accuracy, DUNE may yet contribute to a ^{8}B measurement. The outcome of a combined analysis utilising DUNE, SNO phases I-III [138], Borexino phase II [143], and Super-K phase IV [144] may further constrain the ^{8}B flux.

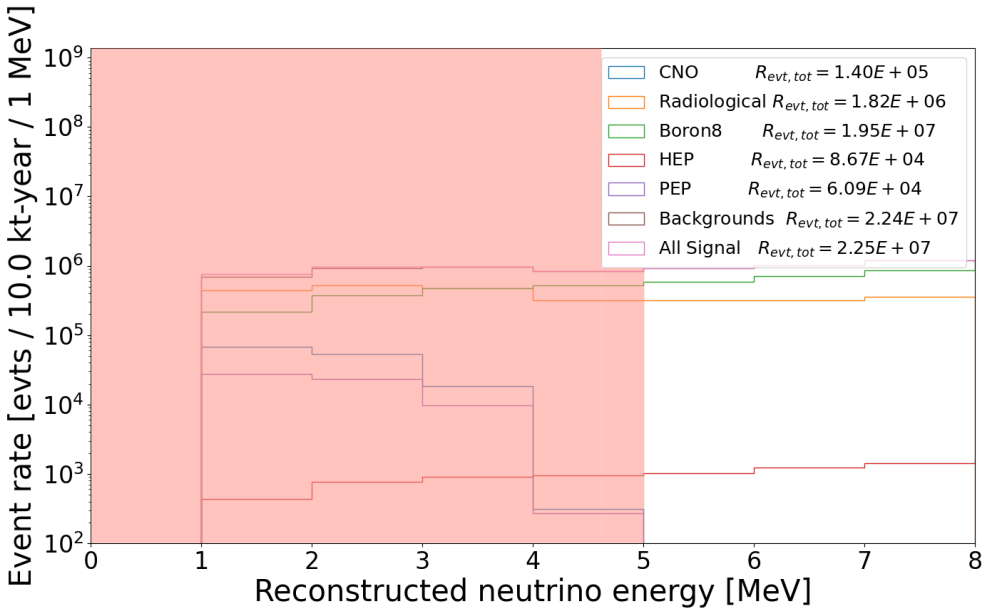

Figure 5.16: The region of interest for targeting ^{8}B neutrinos under a counting experiment. The red area represents the excluded energy region.

5.5 Likelihood testing on CNO neutrino hypotheses

If one has a hypothesis, one might perform an experiment to back it up. Supposing the experimental measurement is naively in support of the original theory, how well can one ensure this agreement? Likelihood-ratio testing evaluates the "goodness of fit" of two statistical models. In this procedure, one defines a hypothesis, H_1, which could be "*CNO neutrinos are present in my data set*", and a null hypothesis, H_0, defined as "*CNO neutrinos are not present in my data set*". Following this, the likelihood of a prediction gets tested against both models to exclude either hypothesis. Under this procedure, one can ultimately make statements such as "*measurement x excludes the null-hypothesis at an nσ confidence level*". Here, σ refers to one stan-

dard deviation of a normal distribution. In experimental particle physics, generally, a 3σ measurement represents evidence towards the hypothesis, and 5σ represents observation or discovery thereof.

5.5.1 Poisson likelihood

Information binned into discrete bins is underpinned by Poisson statistics. Under the Poisson distribution, the probability of observing k data counts when the model predicts λ is:

$$p(k|\lambda) = \frac{\lambda^k e^{-\lambda}}{k!}. \tag{5.11}$$

For N data points, the likelihood of observing them under a given distribution is the product of all their probabilities:

$$\mathcal{L}(k;\lambda) = \prod_{i=1}^{N} p(k_i|\lambda_i) = \frac{\lambda_i^{k_i} e^{-\lambda_i}}{k_i!}. \tag{5.12}$$

If one takes the negative logarithm of Equation 5.12 the product becomes a summation, as follows:

$$-\log \mathcal{L}(k;\lambda) = \sum_{i=1}^{N} \left[\log k_i! - k_i \log \lambda_i + \lambda_i\right]. \tag{5.13}$$

In this form, the likelihood is calculable but computationally tedious. For large k, $k!$ will be exceptionally large before taking its logarithm. The elegance of likelihood testing arises when one takes the logarithm of the ratio of two likelihoods, essentially comparing two different models. One can define a test statistic, q, such that

$$q = -2 \log \left(\mathcal{L}(k;\lambda)/\mathcal{L}(k;\phi)\right) \tag{5.14}$$

Expanding Equation 5.14 one gets

$$\begin{aligned} q &= -2\left[\log \mathcal{L}(k;\lambda) - \log \mathcal{L}(k;\phi)\right] \\ &= -2\sum_{i=1}^{N}\left[\log k_i! - k_i \log \lambda_i + \lambda_i\right] \\ &+ 2\sum_{i=1}^{N}\left[\log k_i! - k_i \log \phi_i + \phi_i\right]. \end{aligned} \tag{5.15}$$

Therefore,

$$q = -2\sum_{i=1}^{N}\left[\lambda_i - \phi_i + k_i \log\left(\frac{\phi_i}{\lambda_i}\right)\right]. \tag{5.16}$$

In general, λ represents the "expected" signal and ϕ is the "observed" signal. Equation 5.16 shows that the more similar λ and ϕ are, the closer to zero the test statistic will be. In contrast, the more dissimilar they are, the larger the test statistic is.

5.5.2 Hypothesis testing and extracting confidence levels

Suppose one defines the following hypothesis, H_1:

"I hypothesise that CNO neutrinos are present within the signal acquired."

Therefore, the null hypothesis, H_0, describes a scenario where CNO neutrinos aren't present. One can test H_1 by searching for an excess of events in hopes of rejecting H_0 to a statistically significant degree.

A key element required in this procedure is a distribution of the test statistic, q, under H_0. This distribution gets generated by running arbitrarily many (generally in the thousands to tens of thousands) Toy Monte Carlo[6] simulations, usually taking the form of a Gaussian distribution centred on the mean value of the test statistic. Finally, the distribution is normalised, imposing that integrating over the entire domain of the test statistic returns one.

Suppose - for example - one develops a distribution of the test statistic under H_0 of the form

$$f(q_{H_0}) = \mathcal{G}(x; \mu = 2, \sigma = 0.2), \tag{5.17}$$

where $\mathcal{G}$ is the normal distribution with mean and standard deviation μ and σ, respectively. Then, suppose a measurement of some physical process gets performed that, when evaluated, returns a test statistic of 2.65. Is a value of 2.65 in agreement with the null hypothesis, or is it sufficient to reject it? Evaluating this is simple: one calculates the p-value of the measured test statistic, then calculates the significance of such a value and decides whether to reject or accept the null hypothesis accordingly. For the example case, a measured test statistic of 2.65 results in a p-value of 1.15×10^{-3} and a significance of 99.88%. With these values, one can reject the null hypothesis at a greater than 3σ confidence level. As mentioned before, a discovery typically requires a 5σ result, or, in other words, a significance of more than 99.99994%.

[6]Toy Monte Carlo refers to a parameterised, lightweight simulation rather than a full physics simulation. When high statistics are required, it becomes too computationally expensive and inefficient to perform high numbers of full simulations.

5.5.3 Likelihood measurement of CNO neutrinos at DUNE

The first question regarding CNO neutrinos at DUNE is whether DUNE can measure the CNO rate. Formally: is the predicted CNO event rate substantial enough and its uncertainty small enough to imply one is not observing a statistical fluctuation?

Here, the hypothesis, H_1, is that CNO neutrinos are present in the acquired event rate, implying the null hypothesis, H_0, states there aren't CNO neutrinos. The generation of the test statistic distribution under H_0 utilises 10^4 Toy Monte Carlo events. The distribution is normalised, as described in Subsection 5.5.2, and fitted with a Gaussian profile. Figure 5.17 shows such a distribution for a low metallicity solar model for a 10 ktonne-year exposure. Additionally, a maximal radiological background reduction is applied, and the systematic uncertainties are in line with Subsection 5.4.7.

Subsections 5.4.3 - 5.4.7 all state uncertainties on the CNO event rate under different conditions. If each value is generalised as $x \pm \sigma$, one can generate three values to examine under hypothesis testing. These values are labelled:

- x, the mean value,
- $x + \sigma$, the best-case value,
- $x - \sigma$, the worst-case value.

To test DUNE's measurement capabilities toward CNO neutrinos, one requires

$$x - \sigma > 0.$$

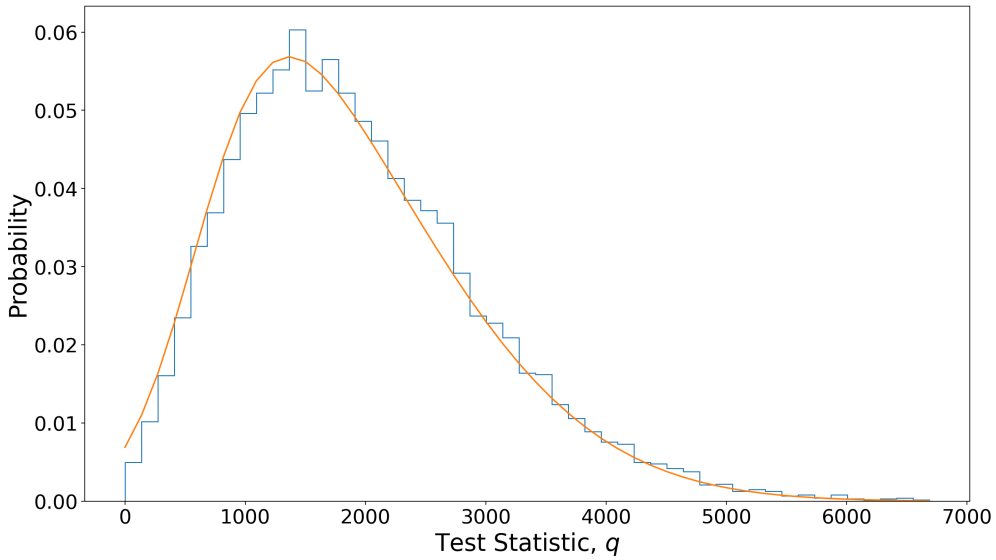

Figure 5.17: The q distribution for low Z, 1000x background reduction and fully constrained systematic uncertainties. The blue histogram shows the values of q, and the orange profile is the Skewed Gaussian best fit.

Here, we define the confidence level at which the null hypothesis gets rejected as the significance of the q value of the worst-case CNO rate. We use the worst-case rate as it gives the most pessimistic evaluation of DUNE's CNO measurement potential.

Realistically, not all of the models described previously merit testing. If the CNO rate calculated is consistent with zero, then that model is ignored. Therefore, testing is conducted on the low background model with the prospective, tightened systematic uncertainties.

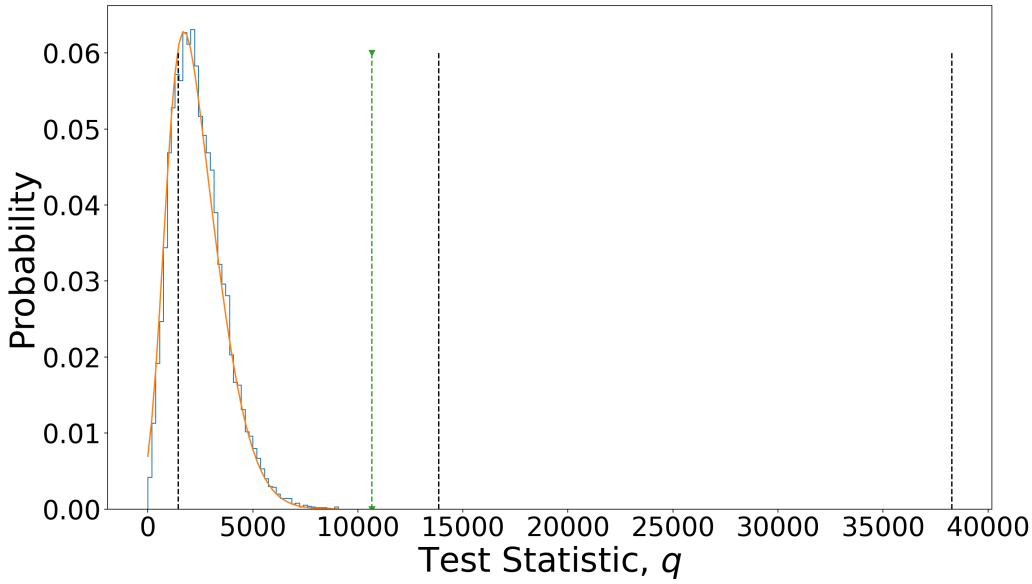

Figure 5.18: The low metallicity likelihood test for CNO measurement at DUNE under tightened systematic uncertainties and low radiological backgrounds. The blue histogram fitted with the orange profile shows the distribution of the test statistic under H_0, the black dashed lines show the worst, mean ad best case values of the measured test statistic, and the green dashed line represents the 5σ value of the test statistic.

Low backgrounds and tighter systematics

Figures 5.18 and 5.19 show several elements in the CNO measurement likelihood procedure for low and high solar metallicity models. The blue histogram fitted with the orange profile illustrates the test statistic distribution under H_0. The vertical dashed black lines represent, going from left to right, the test statistic of the worst-case, mean, and best-case measurements of a CNO excess from the counting experiment.

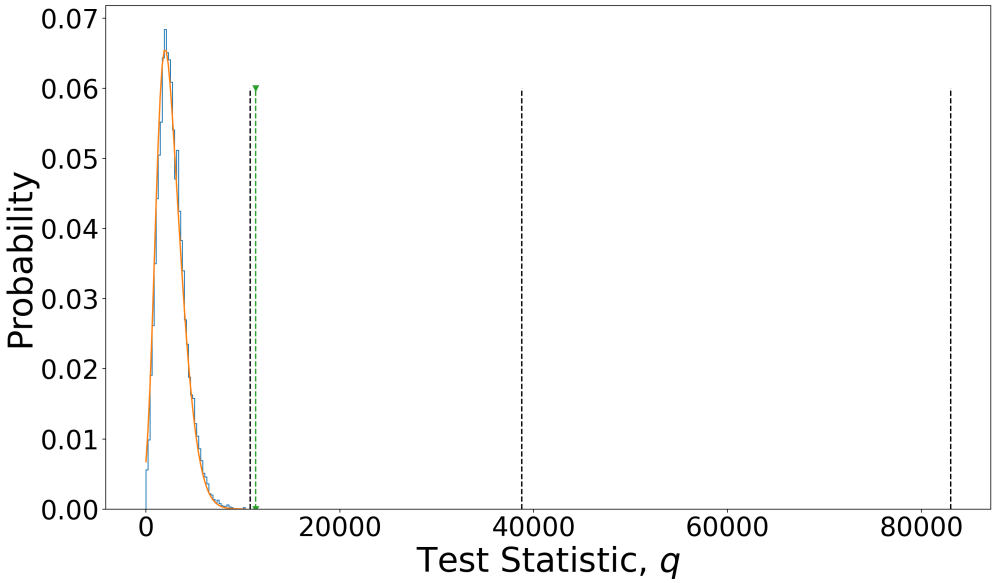

Figure 5.19: The high metallicity likelihood test for CNO measurement at DUNE under tightened systematic uncertainties and low radiological backgrounds. The blue histogram fitted with the orange profile shows the distribution of the test statistic under H_0, the black dashed lines show the worst, mean ad best case values of the measured test statistic, and the green dashed line represents the 5σ value of the test statistic.

Examining the low solar metallicity model first, one observes the worst-case and mean values are of interest. One could reject the null hypothesis at a confidence level of 6.68σ using the mean value of the test statistic. Unfortunately, by the parameters of this search, the mean value is not used for this calculation. Instead, when using the worst-case value, it is clear from the plot that there is no substantive cause to reject the null hypothesis. Therefore, under the low background model with tightened systematic uncertainties, it is unlikely that DUNE could measure CNO neutrinos under a low metallicity model.

Radiological background uncertainty [%]	C.L.
5	0.89σ
4	1.05σ
3	1.17σ
2	1.44σ
1	1.59σ

Table 5.8: The CNO measurement potential for low solar metallicity under varying radiological background uncertainties.

The results are much more encouraging for high solar metallicity. Because this model predicts a much higher flux of neutrinos, the test statistic for the measured value is also higher. The extent of this benefit results in the worst-case value of the test statistic being high enough to reject the null hypothesis at a confidence level of 4.9σ.

Improvements required for CNO measurement under a low solar metallicity model

The radiological background uncertainties limit DUNE's potential for low solar metallicity sensitivity. Therefore, the better the radiological backgrounds are understood, the better the potential for DUNE. Table 5.8 shows the measurement potential of DUNE for varying background uncertainties.

We see that arbitrarily precise knowledge of the dominant radiological backgrounds does not make low-Z CNO observation available at DUNE. One would require the radiological background to be very well understood and an energy resolution of the order $\mathcal{O}(1-3\%)$. Hypothetically, with $\sigma_{\text{radioloiglcal}} = 3\%$ and $\sigma_{E,\,\text{reco}} = 3\%$ DUNE could reject the no-CNO hypothesis at a 3.32σ confidence level. Introducing a low-energy event reconstruction, such as modifying DUNE's PANDORA framework,

would improve the energy reconstruction. However, the extent of the improvement is currently unevaluated. Reconstructing events at such low energy is challenging due to the limited data forming the event. Additionally, measuring the contamination levels of radiologically active backgrounds, such as the ^{42}Ar content of UAr and radon levels, may improve their associated uncertainties. Under these considerations, such tightly constrained systematics at the MeV scale are unlikely at DUNE.

5.5.4 Likelihood measurement of solar metallicity with CNO neutrinos at DUNE

CNO neutrinos can offer an insight into the metallicity of the Sun. Theoretical models imply higher metallicity solar models generate a higher solar neutrino flux. Therefore, one can apply a likelihood-based hypothesis testing approach to discern the Sun's metallicity.

The hypothesis testing for separating low and high metallicity models gets defined as a search for an excess in the acquired event rate. Therefore, the null hypothesis, H_0, is that the Sun has a lower metallicity, and H_1 states the Sun has a high metallicity. Following this, a similar procedure to that described in Subsection 5.5.3 gets applied.

Generating a distribution for the null hypothesis test statistic utilises a low solar metallicity simulation under the low background model with tightened systematic uncertainties. As before, 10,000 events form the distribution, which gets fitted with a Gaussian-like profile. Under the same detector model, the high metallicity CNO

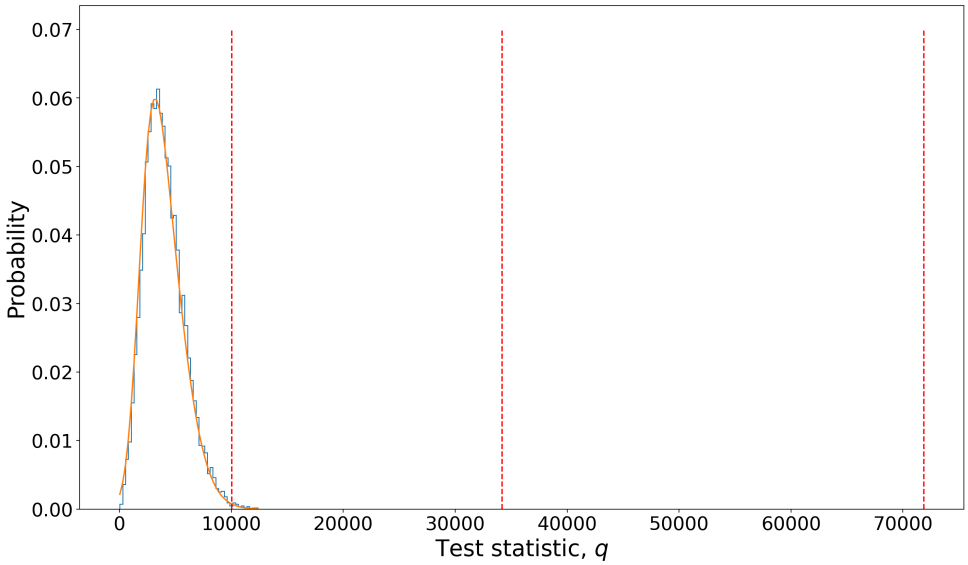

Figure 5.20: The test statistics for differentiating low from high solar metallicity. The blue distribution fitted with an orange Gaussian profile represents the distribution under a low metallicity null hypothesis. The red dashed lines represent the worst, mean, and best-case values for a high solar metallicity hypothesis, going from left to right.

neutrino rate gets evaluated, resulting in the worst-, mean, and best-case values, as before. Figure 5.20 shows the H_0 distribution and the worst-, mean, and best-case CNO rates under high metallicity as red dashed lines going from left to right.

The p-value of the worst-case high metallicity CNO rate is approximately 1.20×10^{-3}. This p-value implies a significance value of 99.88%, ultimately rejecting the null hypothesis at a 3.24σ confidence level. A confidence level of 3.24σ does not conclusively imply DUNE can separate metallicity models. It does, however, motivate DUNE's ability to do so. As the low-background model, if constructed, would only be the third or fourth far detector module, it is not optimistic to think that systematic uncertainty reduction of this scale is possible.

5.5.5 Conclusions on CNO measurements and likelihood testing

Low-energy physics studies are part of the main physics goals of DUNE. We have shown that DUNE has limited but non-zero sensitivity to CNO neutrino interactions. Furthermore, by utilising clever clustering and triggering models, constraints are possible within the CNO energy region of interest on the solar neutrino and radiological backgrounds.

Subsections 5.4.4 - 5.4.7 demonstrate that measuring the CNO neutrino rate at DUNE is possible with $< 100\%$ uncertainty. To do so requires two principal improvements. The first is implementing a low-background DUNE far detector module to combat the high radiological background rate compared to the CNO signal. The second is constraining the systematic uncertainties associated with measuring CNO neutrinos. The main uncertainties that require management are energy reconstruction and radiological background rates. Modifying the event reconstruction framework, PANDORA, to target MeV level events would help the energy reconstruction uncertainty. Additionally, radiological background measurements would help constrain their systematics. With the described improvements, DUNE could perform a 0.89σ and 4.86σ measurement of CNO neutrinos, depending on low or high metallicity, respectively.

Model	Uncertainty	
	High Z	Low Z
Low-background	$\sim 160\%$	$\sim 160\%$
Tighter systematics	$3.66 \times 10^4\%$	$3.66 \times 10^4\%$
Low-background and tighter systematics	43%	68%

Table 5.9: Table showing the CNO event rate uncertainty under various systematic improvements.

Were DUNE to facilitate the systematic constraints and low-background model, CNO neutrino measurements would help elucidate the metallicity of the Sun. DUNE could reject a low solar metallicity hypothesis at a 3.24σ confidence level. While this does not achieve the 5σ threshold of discovery set by experimental particle physics, it does motivate DUNE's ability to discriminate between solar metallicity models. Furthermore, this is achievable within a 10 ktonne-year exposure.

Chapter 6

Conclusions and further work

"Whatever you do, don't be another brick in the wall."

— H. J. Moody

This thesis presents two analyses, the first being an exploration of the radiological neutrons at the DUNE far detector. The pre-existing neutron simulation gets executed in a workspace geometry. This geometry results in a poor representation of neutrons propagation within a far detector module. The construction of a complete, 17-ktonne DUNE far detector geometry, designed following the DUNE construction documentation, allowed for more physically accurate simulations of radiological neutrons. In addition, material spectroscopy of samples collected from the cavern and protoDUNE elucidated the molecular composition of the rock and other components. These molecular compositions informed `GEANT4` during particle propagation and also `SOURCES4C` for the generation of neutron production energy spectra. The total neutron capture rate combines the contributions from the external radiological neutron sources - the cavern rock, concrete and shotcrete - and the internal sources - steel I-beams, steel cryostat layers and field cage. Ultimately, a radiological neutron capture rate 3.05 ± 0.13 captures / 10 ktonne-s is predicted at DUNE.

One of DUNE's primary physics goals is the observation of supernova neutrinos, a low-energy interaction with an energy range of $\mathcal{O}(1 - 100)$ MeV. An ancillary goal is the observation of solar neutrino signals. The second analysis assesses DUNE's viability for observing CNO neutrinos, a low-energy signal from a subdominant helium production channel in the Sun. A purpose-developed clustering and triggering model, utilising the collection and induction planes of the TPC, shows non-zero triggering efficiency for CNO neutrinos. Despite a non-zero trigger efficiency, a baseline DUNE far detector module is unlikely to show statistically significant evidence for CNO neutrinos. Unfortunately, the radiological background levels are too high, and the systematic uncertainties are not constrained enough.

Possible improvements exist, bettering DUNE's abilities as a CNO neutrino observatory. The first improvement is the low-background module of opportunity. In theory, using underground argon instead of atmospheric argon as the detector medium reduces the radon contamination by ~ 1000 times. Additionally, the ^{42}Ar contamination gets reduced by a similar factor. As well as upgrading the detector medium, utilising water shielding around the cryostat would effectively negate the external neutron background, leaving only the unshieldable, internal neutrons. These reductions to the radiological backgrounds make them subdominant to the ^{8}B event rate.

Radiological background reductions get DUNE partially towards statistically significant observations of CNO neutrinos. In addition, constraining the systematics is critical. Fortunately, were the low-background module of opportunity implemented, one could assume arbitrarily precise knowledge of one's radiological contaminants. The combination of tighter uncertainties and reduced event rates significantly minimises the negative impact of the radiological backgrounds.

The energy reconstruction also requires modification. This analysis presents a modest approach to energy reconstruction, yielding usable results with sizeable uncertainties. At the 1-2 MeV scale, event reconstruction is heuristic, given the absence of more sophisticated tools. However, developments in software, such as PANDORA, DUNE's proprietary event reconstruction framework, to target low-energy interactions could improve energy reconstruction further down the analysis pipeline. At the time of writing, such a technique is unavailable but is under active research and development.

With the proposed improvements, hypothesis testing aiming to reject a no-CNO null hypothesis gets tested. We found that under a high solar metallicity model, the no-CNO hypothesis gets rejected at a 4.86σ confidence level. Unfortunately, to get a statistically significant observation of low solar metallicity CNO neutrinos, improvements to the energy reconstruction beyond a reasonable scope are required. DUNE can discriminate high from low solar metallicity at a 3.24σ confidence level. Separating metallicity models is possible considering systematic constraints and reduced radiological backgrounds.

Further work on the radiological neutron examination consists of improvements to the geometry and the addition of neutron generators. Internal volumes, such as the printed circuit boards within the cryostat, are not present in the geometry. Currently, the precise dimensions and materials are not available. Additionally, the CuBe wires are not present in the geometry during the `GEANT4` stage of the simulation chain. Fortunately, the wires' activity is well known as their composition is well defined. Externally, material compositions and volume definitions require revision. Concrete and shotcrete are compositionally similar but will have variations in their water contents. Furthermore, the concrete and shotcrete compositions will require re-evaluation when on-site material samples are acquirable. Volumes, such as the mastic, need adding to the geometry.

Neutrons generated through comic ray interactions currently do not contribute to the total neutron capture rate. Spallation neutron simulations are possible within the `LArSoft` framework, but simulations using the 17-ktonne geometry are unavailable at the time of writing. Theoretically, spallation neutrons are sub-dominant to radiological neutrons [19] but crucial to include for completion.

Were the CNO neutrino study continued, the primary area of research would be targetting experimental systematics. While the systematics discussed are the leading ones, it does not imply a complete overview of the systematics. Features such as detector response, electron lifetime, argon purity and electric field consistency are needed. Uncertainties relating to these parameters will, in the future, be motivated from studying the DUNE detectors when up and running Adding these to the analysis would bring the simulations further toward complete realism. In addition, adding a PANDORA event reconstruction, followed by energy reconstruction, introduces further uncertainties which require evaluation. Developing the low-energy event reconstruction would be an entire study, having critical implications for DUNE as an experiment. If successful, it would improve not only DUNE's solar neutrino efforts but also DUNE's ability to observe neutrinos from supernova events. MeV scale event reconstruction should be a principal research effort in DUNE's low-energy physics program.

Bibliography

[1] W. Nash, "Neutrino physics," *Nature Physical Science*, vol. 229, no. 6, pp. 187–187, 1971.

[2] "Precision electroweak measurements on the Z resonance," *Physics Reports*, vol. 427, no. 5, pp. 257–454, 2006.

[3] J. N. Bahcall, A. M. Serenelli, and S. Basu, "New solar opacities, abundances, helioseismology, and neutrino fluxes," *The Astrophysical Journal Letters*, vol. 621, no. 1, p. L85, 2005.

[4] Y. Fukuda, T. Hayakawa, E. Ichihara, K. Inoue, K. Ishihara, H. Ishino, Y. Itow, T. Kajita, J. Kameda, S. Kasuga, *et al.*, "Evidence for oscillation of atmospheric neutrinos," *Physical Review Letters*, vol. 81, no. 8, p. 1562, 1998.

[5] I. Gil-Botella and A. Rubbia, "Oscillation effects on supernova neutrino rates and spectra and detection of the shock breakout in a liquid argon TPC," *Journal of Cosmology and Astroparticle Physics*, vol. 2003, no. 10, p. 009, 2003.

[6] S. Adrián-Martínez, M. Ageron, F. Aharonian, S. Aiello, A. Albert, F. Ameli, E. Anassontzis, M. André, G. Androulakis, M. Anghinolfi, G. Anton, M. Ardid, T. Avgitas, G. Barbarino, E. Barbarito, B. Baret, J. Barrios-Martí, B. Belhorma, A. Belias, and J. Zuñiga, "Letter of intent for KM3NeT 2.0," *Journal of Physics G: Nuclear and Particle Physics*, vol. 43, 01 2016.

[7] D. R. Nygren, "The time projection chamber: A new 4π detector for charged particles," *PEP-0144*, 1974.

[8] C. Rubbia, "The liquid-argon time projection chamber: a new concept for neutrino detectors," 1977.

[9] "Electronics in LAr." `https://lar.bnl.gov/properties/electronics.html`. Accessed: 2022-04-21.

[10] J. Thomas and D. Imel, "Recombination of electron-ion pairs in liquid argon and liquid xenon," *Physical Review A*, vol. 36, no. 2, p. 614, 1987.

[11] S. Amoruso, M. Antonello, P. Aprili, F. Arneodo, A. Badertscher, B. Baiboussinov, M. B. Ceolin, G. Battistoni, B. Bekman, P. Benetti, *et al.*, "Study of electron recombination in liquid argon with the ICARUS TPC," *Nuclear Instruments and Methods in Physics Research Section A: Accelerators, Spectrometers, Detectors and Associated Equipment*, vol. 523, no. 3, pp. 275–286, 2004.

[12] S. Kubota, A. Nakamoto, T. Takahashi, T. Hamada, E. Shibamura, M. Miyajima, K. Masuda, and T. Doke, "Recombination luminescence in liquid argon and in liquid xenon," *Physical Review B*, vol. 17, no. 6, p. 2762, 1978.

[13] C. Thorn, "Properties of LAr," 2019. "DUNE-doc-14407-v1".

[14] DUNE collaboration *et al.*, "Deep underground neutrino experiment (DUNE): Far detector technical design report. volume i. introduction to DUNE," *Journal of Instrumentation*, vol. 15, no. 8, 2020.

[15] J. Strait, E. McCluskey, T. Lundin, J. Willhite, T. Hamernik, V. Papadimitriou, A. Marchionni, M. J. Kim, M. Nessi, D. Montanari, *et al.*, "Long-baseline neutrino facility (LBNF) and deep underground neutrino experiment (DUNE) conceptual design report volume 3: Long-baseline neutrino facility for DUNE june 24, 2015," *arXiv preprint arXiv:1601.05823*, 2016.

[16] A. A. Abud, B. Abi, R. Acciarri, M. A. Acero, G. Adamov, D. Adams, M. Adinolfi, A. Aduszkiewicz, Z. Ahmad, J. Ahmed, *et al.*, "Deep underground neutrino experiment (DUNE) near detector conceptual design report," *Instruments*, vol. 5, no. 4, p. 31, 2021.

[17] B. Abi, R. Acciarri, M. A. Acero, G. Adamov, D. Adams, M. Adinolfi, Z. Ahmad, J. Ahmed, T. Alion, S. A. Monsalve, *et al.*, "Deep underground neutrino experiment (DUNE), far detector technical design report, volume iv far detector single-phase technology," *arXiv preprint arXiv:2002.03010*, 2020.

[18] A. Avasthi, T. Bezerra, A. Borkum, E. Church, J. Genovesi, J. Haiston, C. Jackson, I. Lazanu, B. Monreal, S. Munson, *et al.*, "Low background kton-scale liquid argon time projection chambers," *arXiv preprint arXiv:2203.08821*, 2022.

[19] J. Beacom, S. W. Li, G. Zhu, and F. Capozzi, "Supplemental material: DUNE as the next-generation solar neutrino experiment," *Phys. Rev. Lett*, vol. 123, p. 131803, 2019.

[20] C. L. Tan, "Big gaps and short bridges: A model for solving the discontinuity problem," *Answers Research Journal*, vol. 9, no. 6, pp. 149–162, 2016.

[21] J. N. Bahcall and R. K. Ulrich, "Solar models, neutrino experiments, and helioseismology," *Reviews of Modern Physics*, vol. 60, no. 2, p. 297, 1988.

[22] Mitch Soderberg, "The MicroBooNE proposal," 2008.

[23] M. Ivanovich and R. S. Harmon, "Uranium-series disequilibrium: applications to earth, marine, and environmental sciences. 2," 1992.

[24] W. Pauli, "Letter to the participants of the conference at Tubingen," *private communication*, 1930.

[25] L. M. Brown, "The idea of the neutrino," *Physics Today*, vol. 31, no. 9, p. 23, 1978.

[26] J. Chadwick, "The existence of a neutron," *Proceedings of the Royal Society of London. Series A, Containing Papers of a Mathematical and Physical Character*, vol. 136, no. 830, pp. 692–708, 1932.

[27] E. Amaldi, "From the discovery of the neutron to the discovery of nuclear fission," *Physics Reports*, vol. 111, no. 1-4, pp. 1–331, 1984.

[28] K. C. Wang, "A suggestion on the detection of the neutrino," *Physical Review*, vol. 61, no. 1-2, p. 97, 1942.

[29] C. Cowan Jr, F. Reines, F. Harrison, E. Anderson, and F. Hayes, "Large liquid scintillation detectors," *Physical Review*, vol. 90, no. 3, p. 493, 1953.

[30] F. Reines and C. Cowan Jr, "A proposed experiment to detect the free neutrino," *Physical Review*, vol. 90, no. 3, p. 492, 1953.

[31] F. Reines and C. Cowan Jr, "Detection of the free neutrino," *Physical Review*, vol. 92, no. 3, p. 830, 1953.

[32] C. L. Cowan, F. Reines, F. B. Harrison, H. W. Kruse, and A. D. McGuire, "Detection of the free neutrino: a confirmation," *Science*, vol. 124, no. 3212, pp. 103–104, 1956.

[33] G. Danby, J. M. Gaillard, K. Goulianos, L. M. Lederman, N. Mistry, M. Schwartz, and J. Steinberger, "Observation of high-energy neutrino reactions and the existence of two kinds of neutrinos," *Physical Review Letters*, vol. 9, no. 1, p. 36, 1962.

[34] M. L. Perl, G. Abrams, A. Boyarski, M. Breidenbach, D. Briggs, F. Bulos, W. Chinowsky, J. Dakin, G. Feldman, C. Friedberg, *et al.*, "Evidence for anomalous lepton production in e^+- e^- annihilation," *Physical Review Letters*, vol. 35, no. 22, p. 1489, 1975.

[35] G. J. Feldman, F. Bulos, D. Lueke, G. Abrams, M. Alam, A. Boyarski, M. Breidenbach, J. Dorfan, C. Friedberg, D. Fryberger, *et al.*, "Inclusive anomalous muon production in e^+ e^- annihilation," *Physical Review Letters*, vol. 38, no. 3, p. 117, 1977.

[36] J. Burmester, L. Criegee, H. Dehne, K. Derikum, R. Devenish, G. Flügge, J. Fox, G. Franke, C. Gerke, P. Harms, *et al.*, "Anomalous muon production in e^+ e^- annihilations as evidence for heavy leptons," *Physics Letters B*, vol. 68, no. 3, pp. 297–300, 1977.

[37] D. Decamp, B. Deschizeaux, J.-P. Lees, M.-N. Minard, J. Crespo, M. Delfino, E. Fernandez, M. Martinez, R. Miquel, M. Mir, *et al.*, "Determination of the number of light neutrino species," *Physics Letters B*, vol. 231, no. 4, pp. 519–529, 1989.

[38] B. Adeva, G. Massaro, M. Fukushima, M. Dhina, N. Colino, A. Böhm, P. Vikas, L. Baksay, A. Degré, F. Marzano, *et al.*, "A determination of the properties of the neutral intermediate vector boson Z^0," *Phys. Lett. B*, vol. 231, no. CIEMAT-640-MF, pp. 509–518, 1989.

[39] M. Akrawy, A. Simon, M. Sasaki, A. Lee, W. Zeuner, M. Hansroul, A. Martin, G. Azuelos, E. Gross, Y. Yang, *et al.*, "Measurement of the Z^0 mass and width with the opal detector at lep," *Phys. Lett. B*, vol. 231, no. CERN-EP-89-133, pp. 530–538, 1989.

[40] P. A. Aarnio, E. Lebreton, J. Loken, J. Grillet, P. Ratoff, G. Voulgaris, J. Contreras, B. Fjeld, G. Lenzen, J. Rídky, *et al.*, "Measurement of the mass and width of the Z^0 particle from multihadronic final states produced in e^+ e^- annihilations," *Phys. Lett. B*, vol. 231, no. CERN-EP-89-134, pp. 539–547, 1989.

[41] K. Kodama, N. Ushida, C. Andreopoulos, N. Saoulidou, G. Tzanakos, P. Yager, B. Baller, D. Boehnlein, W. Freeman, B. Lundberg, *et al.*, "Observation of tau neutrino interactions," *Physics Letters B*, vol. 504, no. 3, pp. 218–224, 2001.

[42] H. A. Bethe, "Energy production in stars," *Physical Review*, vol. 55, no. 5, p. 434, 1939.

[43] J. N. Bahcall, N. A. Bahcall, and G. Shaviv, "Present status of the theoretical predictions for the ^{37}Cl solar-neutrino experiment," *Phys. Rev. Lett.*, vol. 20, pp. 1209–1212, May 1968.

[44] B. Cleveland, T. Daily, R. J. Davis, J. Distel, K. Lande, C. Lee, P. Wildenhain, and J. Ullman, "Update on the measurement of the solar neutrino flux with the homestake chlorine detector," *Nuclear Physics B Proceedings Supplements*, vol. 38, p. 47, 1995.

[45] J. N. Bahcall, M. Kamionkowski, and A. Sirlin, "Solar neutrinos: Radiative corrections in neutrino-electron scattering experiments," *Physical Review D*, vol. 51, no. 11, p. 6146, 1995.

[46] T. K. Gaisser, R. Engel, and E. Resconi, *Cosmic rays and particle physics*. Cambridge University Press, 2016.

[47] F. Reines, M. Crouch, T. Jenkins, W. Kropp, H. Gurr, G. Smith, J. Sellschop, and B. Meyer, "Evidence for high-energy cosmic-ray neutrino interactions," *Physical Review Letters*, vol. 15, no. 9, p. 429, 1965.

[48] C. Achar, M. Menon, V. Narasimham, P. R. Murthy, B. Sreekantan, K. Hinotani, S. Miyake, D. Creed, J. Osborne, J. Pattison, *et al.*, "Detection of muons produced by cosmic ray neutrinos deep underground," *Physics letters*, vol. 18, no. 2, pp. 196–199, 1965.

[49] B. Pontecorvo, "Mesonium and antimesonium," *Zhur. Eksptl'. i Teoret. Fiz.*, vol. 33, 1957.

[50] B. Pontecorvo, "Neutrino experiments and the problem of conservation of leptonic charge," *Sov. Phys. JETP*, vol. 26, no. 984-988, p. 165, 1968.

[51] E. Majorana and L. Maiani, "A symmetric theory of electrons and positrons," in *Ettore Majorana Scientific Papers*, pp. 201–233, Springer, 2006.

[52] C. Giunti and C. W. Kim, *Fundamentals of neutrino physics and astrophysics*. Oxford university press, 2007.

[53] Z. Maki, M. Nakagawa, and S. Sakata, "Remarks on the unified model of elementary particles," *Progress of Theoretical Physics*, vol. 28, no. 5, pp. 870–880, 1962.

[54] M. Guzzo, H. Nunokawa, P. de Holanda, and O. Peres, "Massless "just-so" solution to the solar neutrino problem," *Physical Review D*, vol. 64, no. 9, p. 097301, 2001.

[55] J. N. Bahcall, C. M. Gonzalez-Garcia, and C. Pena-Garay, "Before and after: How has the SNO NC measurement changed things?," *Journal of High Energy Physics*, vol. 2002, no. 07, p. 054, 2002.

[56] A. Y. Smirnov, "The MSW effect and solar neutrinos," *arXiv preprint hep-ph/0305106*, 2003.

[57] S. Mikheev and A. Y. Smirnov, "Resonance amplification of oscillations in matter and spectroscopy of solar neutrinos," *Yadernaya Fizika*, vol. 42, no. 6, pp. 1441–1448, 1985.

[58] S. Mikheyev and A. Y. Smirnov, "Resonant amplification of ν oscillations in matter and solar-neutrino spectroscopy," *Il Nuovo Cimento C*, vol. 9, no. 1, pp. 17–26, 1986.

[59] A. D. Sakharov, "Violation of CP-invariance, C-asymmetry, and baryon asymmetry of the universe," in *In The Intermissions... Collected Works on Research into the Essentials of Theoretical Physics in Russian Federal Nuclear Center, Arzamas-16*, pp. 84–87, World Scientific, 1998.

[60] J. H. Christenson, J. W. Cronin, V. L. Fitch, and R. Turlay, "Evidence for the 2π decay of the k_2^0 meson," *Phys. Rev. Lett.*, vol. 13, pp. 138–140, Jul 1964.

[61] T. Mannel, "Theory and phenomenology of CP violation," *Nuclear Physics-Section B-PS-Proceedings Supplements*, vol. 167, pp. 115–119, 2007.

[62] T. Ohlsson, H. Zhang, and S. Zhou, "Probing the leptonic dirac CP-violating phase in neutrino oscillation experiments," *Physical Review D*, vol. 87, no. 5, p. 053006, 2013.

[63] T. Ohlsson, H. Zhang, and S. Zhou, "Radiative corrections to the leptonic dirac CP-violating phase," *Physical Review D*, vol. 87, no. 1, p. 013012, 2013.

[64] Y. Fukuda, T. Hayakawa, K. Inoue, T. Ishida, S. Joukou, T. Kajita, S. Kasuga, Y. Koshio, T. Kumita, K. Matsumoto, *et al.*, "Atmospheric ν_μ ν_e ratio in the multi-GeV energy range," *Physics Letters B*, vol. 335, no. 2, pp. 237–245, 1994.

[65] S. Ahmed, A. Anthony, E. Beier, A. Bellerive, S. Biller, J. Boger, M. G. Boulay, M. Bowler, T. Bowles, S. Brice, *et al.*, "Measurement of the total active ^{8}B solar neutrino flux at the sudbury neutrino observatory with enhanced neutral current sensitivity," *Physical review letters*, vol. 92, no. 18, p. 181301, 2004.

[66] A. Bueno, I. Gil-Botella, and A. Rubbia, "Supernova neutrino detection in a liquid argon tpc," *arXiv preprint hep-ph/0307222*, 2003.

[67] E. G. Adelberger, A. García, R. H. Robertson, K. Snover, A. Balantekin, K. Heeger, M. Ramsey-Musolf, D. Bemmerer, A. Junghans, C. Bertulani, *et al.*, "Solar fusion cross sections. ii. the pp chain and CNO cycles," *Reviews of Modern Physics*, vol. 83, no. 1, p. 195, 2011.

[68] S. Davini, M. Agostini, S. Appel, G. Bellini, J. Benziger, D. Bick, G. Bonfini, D. Bravo, B. Caccianiga, F. Calaprice, *et al.*, "CNO and pep solar neutrino measurements and perspectives in Borexino," in *Journal of Physics: Conference Series*, vol. 675, p. 012040, IOP Publishing, 2016.

[69] M. Salaris and S. Cassisi, *Evolution of stars and stellar populations*. John Wiley & Sons, 2005.

[70] C. von Weizsäcker, "On transformations of elements in the interiors of stars. i," *Physikalische Zeitschrift*, vol. 38, pp. 176–191, 1937.

[71] C. von Weizsäcker, "On transformations of elements in the interiors of stars. ii," *Physikalische Zeitschrift*, vol. 39, pp. 633–646, 1987.

[72] G. Audi, A. Wapstra, and C. Thibault, "The AME2003 atomic mass evaluation:(ii). tables, graphs and references," *Nuclear physics A*, vol. 729, no. 1, pp. 337–676, 2003.

[73] H. Scheffler and H. Elsaesser, "Physics of the stars and the sun. physik der sterne und der sonne," 1990.

[74] R. Depalo, L. collaboration, *et al.*, "Towards a study of ^{22}Ne (pγ) ^{23}Na at LUNA," in *Journal of Physics: Conference Series*, vol. 665, p. 012017, IOP Publishing, 2016.

[75] N. Prantzos, C. Charbonnel, and C. Iliadis, "Light nuclei in galactic globular clusters: constraints on the self-enrichment scenario from nucleosynthesis," *Astronomy & Astrophysics*, vol. 470, no. 1, pp. 179–190, 2007.

[76] C. Iliadis, A. Champagne, J. José, S. Starrfield, and P. Tupper, "The effects of thermonuclear reaction-rate variations on nova nucleosynthesis: A sensitivity study," *The astrophysical Journal supplement series*, vol. 142, no. 1, p. 105, 2002.

[77] R. Acciarri, M. Acero, M. Adamowski, C. Adams, P. Adamson, S. Adhikari, Z. Ahmad, C. Albright, T. Alion, E. Amador, *et al.*, "Long-baseline neutrino facility (LBNF) and deep underground neutrino experiment (DUNE) conceptual design report, volume 4 the DUNE detectors at LBNF," *arXiv preprint arXiv:1601.02984*, 2016.

[78] H.-K. Proto-Collaboration, K. Abe, H. Aihara, C. Andreopoulos, I. Anghel, A. Ariga, T. Ariga, R. Asfandiyarov, M. Askins, J. Back, *et al.*, "Physics potential of a long-baseline neutrino oscillation experiment using a J-PARC neutrino beam and Hyper-Kamiokande," *Progress of theoretical and experimental physics*, vol. 2015, no. 5, p. 053C02, 2015.

[79] `https://pdg.lbl.gov/2022/tables/contents_tables.html`. Accessed: 2022-06-02.

[80] F. An, J. Bai, A. Balantekin, H. Band, D. Beavis, W. Beriguete, M. Bishai, S. Blyth, K. Boddy, R. Brown, *et al.*, "Observation of electron-antineutrino disappearance at Daya Bay," *Physical Review Letters*, vol. 108, no. 17, p. 171803, 2012.

[81] J. K. Ahn, S. Chebotaryov, J. Choi, S. Choi, W. Choi, Y. Choi, H. Jang, J. Jang, E. Jeon, I. Jeong, *et al.*, "Observation of reactor electron antineutrinos disappearance in the RENO experiment," *Physical Review Letters*, vol. 108, no. 19, p. 191802, 2012.

[82] P. Adamson, C. Ader, M. Andrews, N. Anfimov, I. Anghel, K. Arms, E. Arrieta-Diaz, A. Aurisano, D. Ayres, C. Backhouse, *et al.*, "First measurement of electron neutrino appearance in NOvA," *Physical review letters*, vol. 116, no. 15, p. 151806, 2016.

[83] K. Abe, J. Adam, H. Aihara, T. Akiri, C. Andreopoulos, S. Aoki, A. Ariga, T. Ariga, S. Assylbekov, D. Autiero, *et al.*, "Observation of electron neutrino appearance in a muon neutrino beam," *Physical review letters*, vol. 112, no. 6, p. 061802, 2014.

[84] K. Abe, J. Amey, C. Andreopoulos, M. Antonova, S. Aoki, A. Ariga, D. Autiero, S. Ban, M. Barbi, G. Barker, *et al.*, "Combined analysis of neutrino and antineutrino oscillations at T2K," *Physical review letters*, vol. 118, no. 15, p. 151801, 2017.

[85] P. Adamson, L. Aliaga, D. Ambrose, N. Anfimov, A. Antoshkin, E. Arrieta-Diaz, K. Augsten, A. Aurisano, C. Backhouse, M. Baird, *et al.*, "Constraints on oscillation parameters from ν_e appearance and ν_μ disappearance in NOvA," *Physical review letters*, vol. 118, no. 23, p. 231801, 2017.

[86] C. Kraus, B. Bornschein, L. Bornschein, J. Bonn, B. Flatt, A. Kovalik, B. Ostrick, E. Otten, J. Schall, T. Thümmler, *et al.*, "Final results from phase ii of the Mainz neutrino mass searchin tritium β-decay," *The European Physical Journal C-Particles and Fields*, vol. 40, no. 4, pp. 447–468, 2005.

[87] V. Aseev, A. Belesev, A. Berlev, E. Geraskin, A. Golubev, N. Likhovid, V. Lobashev, A. Nozik, V. Pantuev, V. Parfenov, *et al.*, "Upper limit on the electron antineutrino mass from the Troitsk experiment," *Physical Review D*, vol. 84, no. 11, p. 112003, 2011.

[88] P. Collaboration, P. Ade, N. Aghanim, C. Armitage-Caplan, M. Arnaud, M. Ashdown, F. Atrio-Barandela, J. Aumont, C. Baccigalupi, A. Banday, *et al.*, "Planck 2013 results. xvi. cosmological parameters," *A&A*, vol. 571, p. A16, 2014.

[89] M. Aker, A. Beglarian, J. Behrens, A. Berlev, U. Besserer, B. Bieringer, F. Block, S. Bobien, M. Boettcher, B. Bornschein, *et al.*, "Direct neutrino-mass measurement with sub-electronvolt sensitivity," *Nature Physics*, vol. 18, no. 2, 2022.

[90] S. Amerio, S. Amoruso, M. Antonello, P. Aprili, M. Armenante, F. Arneodo, A. Badertscher, B. Baiboussinov, M. B. Ceolin, G. Battistoni, *et al.*, "Design, construction and tests of the ICARUS T600 detector," *Nuclear Instruments and Methods in Physics Research Section A: Accelerators, Spectrometers, Detectors and Associated Equipment*, vol. 527, no. 3, pp. 329–410, 2004.

[91] C. Anderson, M. Antonello, B. Baller, T. Bolton, C. Bromberg, F. Cavanna, E. Church, D. Edmunds, A. Ereditato, S. Farooq, *et al.*, "The ArgoNeuT detector in the NuMI low-energy beam line at Fermilab," *Journal of Instrumentation*, vol. 7, no. 10, p. P10019, 2012.

[92] F. Cavanna, M. Kordosky, J. Raaf, and B. Rebel, "LArIAT: Liquid argon in a testbeam," tech. rep., Fermi National Accelerator Lab.(FNAL), Batavia, IL (United States), 2014.

[93] R. Acciarri, C. Adams, R. An, A. Aparicio, S. Aponte, J. Asaadi, M. Auger, N. Ayoub, L. Bagby, B. Baller, *et al.*, "Design and construction of the MicroBooNE detector," *Journal of Instrumentation*, vol. 12, no. 02, p. P02017, 2017.

[94] B. Baller, C. Bromberg, N. Buchanan, F. Cavanna, H. Chen, E. Church, V. Gehman, H. Greenlee, E. Guardincerri, B. Jones, *et al.*, "Liquid argon time projection chamber research and development in the united states," *Journal of Instrumentation*, vol. 9, no. 05, p. T05005, 2014.

[95] V. Chepel and H. Araújo, "Liquid noble gas detectors for low energy particle physics," *Journal of Instrumentation*, vol. 8, no. 04, p. R04001, 2013.

[96] D. Rivera, "Triggering on solar neutrinos in DUNE," 2020. "DUNE-doc-20120-v1".

[97] H. Nunokawa, S. Parke, and J. W. Valle, "CP violation and neutrino oscillations," *Progress in Particle and Nuclear Physics*, vol. 60, no. 2, pp. 338–402, 2008.

[98] "Constraint on the matter–antimatter symmetry-violating phase in neutrino oscillations," 2020.

[99] T. Fazzini, G. Fidecaro, A. W. Merrison, H. Paul, and A. Tollestrup, "Electron decay of the pion," *Physical Review Letters*, vol. 1, no. 7, p. 247, 1958.

[100] F. Bossi, E. De Lucia, J. Lee-Franzini, S. Miscetti, and M. Palutan, "Precision kaon and hadron physics with KLOE," *La Rivista del Nuovo Cimento*, vol. 31, no. 10, pp. 531–623, 2008.

[101] J.-M. Levy, "Kinematics of an off axis neutrino beam," *arXiv preprint arXiv:1005.0574*, 2010.

[102] G. Zhu, S. W. Li, and J. F. Beacom, "Developing the MeV potential of DUNE: Detailed considerations of muon-induced spallation and other backgrounds," *Physical Review C*, vol. 99, no. 5, p. 055810, 2019.

[103] D. Caratelli, W. Foreman, A. Friedland, S. Gardiner, I. Gil-Botella, G. K. M. Kirby, G. L. Miotto, B. Littlejohn, M. Mooney, J. Reichenbacher, *et al.*, "Low-energy physics in neutrino LArTPCs," *arXiv preprint arXiv:2203.00740*, 2022.

[104] C. E. Aalseth, F. Acerbi, P. Agnes, I. Albuquerque, T. Alexander, A. Alici, A. Alton, P. Antonioli, S. Arcelli, R. Ardito, *et al.*, "Darkside-20k: A 20 tonne two-phase LAr TPC for direct dark matter detection at LNGS," *The European Physical Journal Plus*, vol. 133, no. 3, pp. 1–129, 2018.

[105] R. Ajaj, P.-A. Amaudruz, G. Araujo, M. Baldwin, M. Batygov, B. Beltran, C. Bina, J. Bonatt, M. Boulay, B. Broerman, *et al.*, "Search for dark matter with a 231-day exposure of liquid argon using DEAP-3600 at SNOLAB," *Physical Review D*, vol. 100, no. 2, p. 022004, 2019.

[106] P. Benetti, F. Calaprice, E. Calligarich, M. Cambiaghi, F. Carbonara, F. Cavanna, A. Cocco, F. Di Pompeo, N. Ferrari, G. Fiorillo, *et al.*, "Measurement of the specific activity of ^{39}Ar in natural argon," *Nuclear Instruments and Methods in Physics Research Section A: Accelerators, Spectrometers, Detectors and Associated Equipment*, vol. 574, no. 1, pp. 83–88, 2007.

[107] P. Agnes, L. Agostino, I. Albuquerque, T. Alexander, A. Alton, K. Arisaka, H. Back, B. Baldin, K. Biery, G. Bonfini, *et al.*, "Results from the first use of low radioactivity argon in a dark matter search," *Physical Review D*, vol. 93, no. 8, p. 081101, 2016.

[108] J. Schröder, K. Münnich, and D. Ehhalt, "Physical sciences: krypton-85 in the troposphere," *Nature*, vol. 233, no. 5322, pp. 614–615, 1971.

[109] M. Tanabashi, K. Hagiwara, K. Hikasa, K. Nakamura, Y. Sumino, F. Takahashi, J. Tanaka, K. Agashe, G. Aielli, C. Amsler, *et al.*, "Review of particle physics: particle data groups," 2018.

[110] S. Dimopoulos, S. Raby, and F. Wilczek, "Proton decay in supersymmetric models," *Physics Letters B*, vol. 112, no. 2, pp. 133–136, 1982.

[111] K. Abe, Y. Hayato, K. Iyogi, J. Kameda, M. Miura, S. Moriyama, M. Nakahata, S. Nakayama, R. Wendell, H. Sekiya, *et al.*, "Search for proton decay via p $\rightarrow$ ν k+ using 260 kiloton· year data of super-kamiokande," *Physical Review D*, vol. 90, no. 7, p. 072005, 2014.

[112] R. Bionta, G. Blewitt, C. Bratton, D. Casper, A. Ciocio, R. Claus, B. Cortez, M. Crouch, S. Dye, S. Errede, *et al.*, "Observation of a neutrino burst in coincidence with supernova 1987A in the large magellanic cloud," in *Neutrinos And Other Matters: Selected Works of Frederick Reines*, pp. 340–342, World Scientific, 1991.

[113] K.-I. Collaboration *et al.*, "Observation of a neutrino burst from the supernova SN1987A," in *Atmospheric Diagnostics of Stellar Evolution: Chemical Peculiarity, Mass Loss, and Explosion*, pp. 335–347, Springer, 1988.

[114] A. Mirizzi, I. Tamborra, H.-T. Janka, N. Saviano, K. Scholberg, R. Bollig, L. Hüdepohl, and S. Chakraborty, "Supernova neutrinos: production, oscillations and detection," *La Rivista del Nuovo Cimento*, vol. 39, no. 1, pp. 1–112, 2016.

[115] S. Horiuchi and J. P. Kneller, "What can be learned from a future supernova neutrino detection?," *Journal of Physics G: Nuclear and Particle Physics*, vol. 45, no. 4, p. 043002, 2018.

[116] "Www table of radioactive isotopes." `http://nucleardata.nuclear.lu.se/toi/nuclide.asp?iZA=180039`. Accessed: 2022-06-21.

[117] "Www table of radioactive isotopes." `http://nucleardata.nuclear.lu.se/toi/nuclide.asp?iZA=180042`. Accessed: 2022-06-21.

[118] "Www table of radioactive isotopes." `http://nucleardata.nuclear.lu.se/toi/nuclide.asp?iZA=190042`. Accessed: 2022-06-21.

[119] A. Barabash, R. Saakyan, and V. Umatov, "On concentration of ^{42}Ar in liquid argon," in *Journal of Physics: Conference Series*, vol. 718, p. 062004, IOP Publishing, 2016.

[120] S. Paige, "Geology of the region around lead south dakota and its bearing on the homestake ore body," tech. rep., Washington: Government Printing Office, 1924.

[121] "Www table of radioactive isotopes." `http://nucleardata.nuclear.lu.se/toi/nuclide.asp?iZA=360085`. Accessed: 2022-06-22.

[122] D. C. Kocher, "Radioactive decay data tables," tech. rep., Oak Ridge National Lab., TN (USA), 1981.

[123] "Www table of radioactive isotopes." http://nucleardata.nuclear.lu.se/toi/nuclide.asp?iZA=830210. Accessed: 2022-06-23.

[124] "Www table of radioactive isotopes." http://nucleardata.nuclear.lu.se/toi/nuclide.asp?iZA=830214. Accessed: 2022-06-23.

[125] A. Popeko and G. Ter-Akop'yan, "Multiplicity of prompt neutrons in spontaneous fission of ^{238}U," 1976.

[126] B. Viren, "GeGeDe." https://github.com/brettviren/gegede, 2014.

[127] F. Mauger and V. Tretyak, "BxDecay0." https://github.com/BxCppDev/bxdecay0, 2022.

[128] R. B. Pahlka, "The SuperNEMO experiment," *arXiv preprint arXiv:0810.3169*, 2008.

[129] S. Gardiner, "Simulating low-energy neutrino interactions with MARLEY," *Comput. Phys. Commun.*, vol. 269, p. 108123, 2021.

[130] J. Bahcall, "Software and data for solar neutrino research." http://www.sns.ias.edu/~jnb/SNdata/sndata.html. Accessed: 2022-06-28.

[131] J. MacQueen, "Classification and analysis of multivariate observations," in *5th Berkeley Symp. Math. Statist. Probability*, pp. 281–297, 1967.

[132] L. Rokach and O. Maimon, "Clustering methods," in *Data mining and knowledge discovery handbook*, pp. 321—-352, Springer, 2006.

[133] H.-P. Kriegel, P. Kröger, J. Sander, and A. Zimek, "Density-based clustering," *Wiley interdisciplinary reviews: data mining and knowledge discovery*, vol. 1, no. 3, pp. 231–240, 2011.

[134] P. Lasorak, "Clustering." `https://github.com/plasorak/Clustering`, 2019.

[135] N. Vinyoles, A. M. Serenelli, F. L. Villante, S. Basu, J. Bergström, M. Gonzalez-Garcia, M. Maltoni, C. Peña-Garay, and N. Song, "A new generation of standard solar models," *The Astrophysical Journal*, vol. 835, no. 2, p. 202, 2017.

[136] S. Gardiner, "Simulating low-energy neutrino interactions with MARLEY," *Computer Physics Communications*, vol. 269, p. 108123, 2021.

[137] J. J. Hopfield, "Neural networks and physical systems with emergent collective computational abilities.," *Proceedings of the national academy of sciences*, vol. 79, no. 8, pp. 2554–2558, 1982.

[138] B. Aharmim, S. Ahmed, A. Anthony, N. Barros, E. Beier, A. Bellerive, B. Beltran, M. Bergevin, S. Biller, K. Boudjemline, *et al.*, "Combined analysis of all three phases of solar neutrino data from the sudbury neutrino observatory," *Physical Review C*, vol. 88, no. 2, p. 025501, 2013.

[139] V. Ashitkov, A. S. Barabash, S. Belogurov, G. Carugno, S. Konovalov, F. Massera, G. Puglierin, R. Saakyan, V. Stekhanov, and V. Umatov, "Double beta decay of ^{100}Mo," *Journal of Experimental and Theoretical Physics Letters*, vol. 74, no. 11, pp. 529–531, 2001.

[140] V. Kudryavtsev, "Neutron production in surf rock." https://indico.fnal.gov/event/43870/contributions/191946/attachments/131796/161519/neutrons-dune-rock-bgtf-review-july2020.pdf. Accessed: 2022-07-07.

[141] J. Reichenbacher, J. Stock, and J. Haiston, "Radiological background model for DUNE MCCs." https://indico.fnal.gov/event/17817/contributions/44869/attachments/27869/34486/DUNE_RadiologicalModel_14Aug2018_JR.pdf. Accessed: 2022-07-08.

[142] B. Abi, R. Acciarri, M. A. Acero, G. Adamov, D. Adams, M. Adinolfi, Z. Ahmad, J. Ahmed, T. Alion, S. A. Monsalve, *et al.*, "Deep underground neutrino experiment (DUNE), far detector technical design report, volume ii: DUNE physics," *arXiv preprint arXiv:2002.03005*, 2020.

[143] B. collaboration, "Neutrinos from the primary proton–proton fusion process in the sun," *Nature*, vol. 512, no. 7515, pp. 383–386, 2014.

[144] K. Abe, Y. Haga, Y. Hayato, M. Ikeda, K. Iyogi, J. Kameda, Y. Kishimoto, L. Marti, M. Miura, S. Moriyama, *et al.*, "Solar neutrino measurements in Super-Kamiokande-IV," *Physical Review D*, vol. 94, no. 5, p. 052010, 2016.

Acronyms

AAr Atmospheric Argon.

ADC Analogue to Digital Conversion.

APA Anode Plane Assembly.

ArgoNeuT Argon Neutrino Teststand.

BSM Beyond Standard Model.

CC Charge Current.

CERN Conseil européen pour la recherche nucléaire.

CKM Cabibbo–Kobayashi–Maskawa.

CNO Carbon Nitrogen Oxygen.

CP Charge-Parity.

CPA Cathode Plane Assembly.

DAQ Data Acquisition.

DASP Double Arm Spectrometer.

DEAP Dark matter Experiment using Argon Pulse-shape discrimination.

DESY Deutsches Elektronen-Synchrotron.

DONUT Direct Observation of NuTau.

DUNE Deep Underground Neutrino Experiment.

DUNE-PRISM DUNE Precision Reaction-Independent Spectrum Measurement.

ECAL Electromagnetic Calorimeter.

ES Elastic Scattering.

eV Electronvolt.

FD Far Detector.

FLUKA FLUktuierende KAskade.

FNAL Fermi National Accelerator Laboratory.

FWHM Full Width Half Maximum.

GALLEX Gallium Experiment.

GAr Gaseous Argon.

GDML Geometry Description Markup Language.

GEANT4 Geometry and Tracking 4.

GEGEDE General Geometry Description.

GeV Giga Electronvolt.

GUT Grand Unified Theory.

HC Hit Channel.

HEP Helium Proton.

HPgTPC High Pressure Gas Time Projection Chamber.

HT Hit Time.

ICARUS Imaging Cosmic And Rare Underground Signals.

IMB Irvine-Michigan-Brookhaven.

J-PARC Japan Proton Accelerator Research Complex.

KamiokaNDE Kamioka Nucleon Decay Experiment.

KATRIN Karlsruhe Tritium Neutrino Experiment.

KLOE K^0_L Long Experiment.

LAr Liquid Argon.

LArIAT Liquid Argon In A Testbeam.

LArSoft Liquid Argon Software.

LArTPC Liquid Argon Time Projection Chamber.

LBNF Long Baseline Neutrino Facility.

LEP Large Electron-Positron Collider.

LHC Large Hadron Collider.

LMC Large Magellanic Cloud.

MARLEY Model of Argon Reaction Low Energy Yield.

MeV Mega Electronvolt.

MicroBooNE Micro Booster Neutrino Experiment.

MINOS Main Injector Neutrino Oscillation Search.

ML Machine Learning.

MSW Makheev-Smirnov-Wolfstein.

NC Neutral Current.

ND Near Detector.

NeuCBoT Neutron Calculator Based on TALYS.

NOvA NuMI Off-Axis ν_e Appearance.

NuMI Neutrinos at the Main Injector.

PCB Printed Circuit Board.

PD Photon Detector.

PDF Probability Distribution Function.

PDG Particle Data Group.

PDS Photon Detector System.

PID Particle Identification.

PMNS Pontecorvo-Maki-Nakagawa-Sakata.

QCD Quantum Chromodynamics.

RENO Reactor Experiment for Neutrino Oscillation.

RHC Reverse Horn Current.

RMS Root Mean Squared.

ROI Region of Interest.

SADC Summed Analogue to Digital Conversion.

SAGE Soviet–American Gallium Experiment.

SAND System for on-Axis Neutrino Detection.

SF Spontaneous Fission.

SiPM Silicon Photomultiplier.

SLAC Stanford Linear Accelerator Center.

SNB Supernova Burst.

SNO Sudbury Neutrino Observatory.

SNU Solar Neutrino Unit.

SPEAR Stanford Positron Electron Asymmetric Rings.

SSM Standard Solar Model.

SuperNEMO Super Neutrino Ettore Majorana Observatory.

SURF Sanford Underground Research Facility.

T2K Tokai-to-Kamioka.

TPC Time Projection Chamber.

UAr Underground Argon.

UV Ultraviolet.

WLS Wavelength-Shifting.

Appendix A

Quicksort Algorithm

Suppose we have the array of values:

6	5	3	1	8	7	2	4

.

For this example, we will choose 3 as our pivot value. Now, looking from left to right we locate the first value that is larger than the pivot; in this case 6. Similarly, from right to left we locate the first value that is smaller than our pivot; in this case 2. With both values located their positions are swapped.

2	5	3	1	8	7	6	4

With the two values now on the correct side of the pivot, the process is repeated, this time finding values 5 and 1.

2	1	3	5	8	7	6	4

If the pointers were to continue to increment, finding the first value smaller than the pivot value, one would find that its index is smaller than that of the pivot. If all values on the left and right are smaller and more than the pivot, respectively, it signals that this stage of the algorithm is complete. Following this, the algorithm is repeated on the sub-arrays on either side of the initial pivot, similarly ordering them.

Arranging the smaller and larger values to the left and right of the pivot has complexity $O(\log n)$ where n is the number of elements in the array. This process gets repeated recursively, visiting every list item. Therefore, the overall complexity of the quicksort algorithm is $O(n \log n)$, assuming properly chosen pivots at each stage.